3271

JNCASR
Acc No 3271
LIBRARY

Library copy

Photoelectric Properties of Hybrid Conjugated Polymer Based Bilayer Structures

JNCASR
547.7 P03
3271

A Thesis submitted in partial fulfillment
of the requirements of the degree of
Doctor of Philosophy

By
Manoj. A. G

Chemistry and Physics of Materials Unit
Jawaharlal Nehru Centre for Advanced Scientific Research (Deemed University)
Bangalore – 560 064 (INDIA)
August 2003

To

my parents and guru

547.7
Pob Thesis

Declaration

I hereby declare that this thesis entitled "Photoelectric properties of hybrid conjugated polymer based bilayer structures" is an authentic record of research work carried out by me under the supervision of Prof. K. S. Narayan at the Molecular Electronics Lab. Chemistry and Physics of Materials Unit, Jawaharlal Nehru Centre for Advanced Scientific Research, Bangalore, India.

In keeping with the general practice of reporting scientific observations, due acknowledgement has been made whenever work described here has been based on the findings of other investigators. Any oversight due to error of judgement is regretted.

Manoj. A. G

JAWAHARLAL NEHRU CENTRE FOR ADVANCED SCIENTIFIC RESEARCH
Jakkur, Bangalore 560064, India

K. S. Narayan
Associate Professor
Chemistry and Physics of Materials Unit

PHONE: 91 80 8462750-57
FAX: 91 80 8462766
e-mail: narayan@jncasr.ac.in

7th August 2003

Certificate

Certified that the work described in this thesis titled "Photoelectric properties of hybrid conjugated polymer based bilayer structures" has been carried out under my supervision at the Molecular Electronics Lab, Chemistry and Physics of Materials Unit, Jawaharlal Nehru Centre for Advanced Scientific Research, Bangalore, India.

Prof. K. S. Narayan

Acknowledgments

I don't think I can express my sincere thanks to my advisor Prof. K. S. Narayan in few words. His way of thinking and approach to the challenging problems is always a source of inspiration to find new phenomena's in science. I am indebted to him for his valuable suggestions and help during my difficult time with science and life. I really enjoyed the freedom he gave me in our lab. I also thank him for providing financial assistance in the early stages, when I started exploring science with him. I am also fascinated with the ideology and principle he followed in his life. I tried to learn and practice it in my life. I also express my sincere thanks to his family members, who were equally supportive to me during my stay in JNCASR.

I thank Prof C. N R. Rao, FRS, Chairman of CPMU, JNCASR for his encouragement and financial assistance he provided me during my stay in JNCASR. I also thank him for allowing me to use various facilities in our centre. I also express my sincere thanks to Prof Rao's family for their constant support and encouragement.

I thank my labmates present and past, Dr A. A. Alagiriswamy, Gurulingamurthy, N. Kumar, Geetha.K.Varier, Birendra Singh, Soumya Dutta, Dinesh Kabra, Basavaraj, Arun, Dhritiman and Satyanarayan for their constant encouragement and an enjoyable life in our lab.

I thank my collaborators Prof. Ramakrishnan (IPC, IISc) for his valuable suggestion and help during my graduation. He was a constant source of inspiration. I also thank Prof D. D. Sarma (SSCU, IISc) for his support during the collaborative project. I thank Dr. G. Padmanabhan, Dr Gouri, Dr.Beena Anni Kuruvilla and Dr J. Nanda for their help and encouragement during the collaborative projects.

I thank Dr. Umesh Waghmare and family for their constant support, discussions and encouragement during my stay in JNCASR. I won't be able to fit in few words about their hospitality and helping hand during my stay here.

I thank Dr Ranga Uday Kumar for allowing me to use his laboratory facilities and lab members Lakshnmi Ramaksrishna, Siddappa, and Prashant for their helping hand in dealing with biological samples.

I thank Dr. Swapan Pati and Dr. Chandrabhas for their scientific discussion and constant support. I thank Prof. V. Krishnan, Prof. G. U. Kulkarni, Dr. A. R. Raju, Dr. Balasubrahmaniam, Prof. Natarajan, Prof. Shobhana Narasimhan, Prof. Hemalatha Balaram, Dr. Srikanth Sastry and Dr. Rama Govindarajan for their constant encouragement.

I thank the help of Mrs. Usha with TEM, Srinath, Srinivas with electronic problems, Anil with X-ray diffraction, Vasu with UV-VIS and IR, Basvaraj and Rengnathan with SEM, Rajesh Khanna for computer assistance, Arokyanathan for assistance at the workshop and Sidharaju for lab assistance..

I thank Dr. P. S. Anilkumar and family, Dr. Pradeep Namboodiri and family and Dr. Santhosh. P. N and family and N. Vinod for their valuable help and encouragement during my studies.

I thank my friends: Drs, seniors and colleagues Eswar, Govinda, Siva, Saji, Sujay, Pattu, Sameen and family, Muruga, Sheeba, Gargi, Geetha, Vanitha, Sachin, Jaya, John, Ashish, Vaidhya, Ram, Anupama, Neena, Reji, Goutham, Deepak, S.Lakshmi, Pushpa, Sudhee, Kavitha, Kavitha. G, Aparna, Motin, Padma, Kunj, Ved, amitav, manashi and C. P. Vinod for their constant encouragement and making the hostel life enjoyable.

I thank my cousin Mr. Damodaran Namboodiri and family for their constant support and hospitality during my stay in Bangalore.

I am grateful to the administrative, library and mess staff members of JNC for all the help they have provided. I am thankful to Basavraj, Keshav, Harish and employees of students residence for their help during my stay at hostel.

I wouldn't have been here without constant support of my teachers who inspired me to take up science. I thank Late Prof. P. G. Kesavan Potty and his family, Prof. K. P. Unnikrishnan, Prof. K. K. L. Leelamma, Prof. Neelakantan Ammukutty teacher and other teachers for their constant encouragement and support.

I thank Dr. Parameswaran Potty and family for their helping hand and encouragement during my bad health days.

I wish to express my gratitude to my parents, muthassi, my brother Raghu, my sister Mallika, my brother in law Narayanan and my relatives for, without their support and encouragement, this study wouldn't have been possible.

Preface

The research studies in this thesis focus on soft-matter bilayer systems from the perspective of optical and electronic properties. Three different class of bilayer structures were studied (i) p-type semiconducting Polymer/n-type semiconducting conjugated polymer (CP) structures for photovoltaic properties (ii) doped-conducting polymer-blend/bacteriorhodopsin (bR) structure for studying synergetic processes at the interface (iii) semiconducting-polymer/nanoparticle devices for tunable light emitting diodes and photodiodes.

The transport characteristics of photogenerated free charge carriers across the interface of a bilayer consisting of p-type polyalkylthiophene derivatives or polyparaphenylene vinylene derivatives and n-type polymer poly(benzimidazobenzo phenanthroline) are studied using photocurrent spectral response, intensity modulated photocurrent spectra, current-voltage and thermally stimulated current measurements. The parameters governing the device efficiency are controlled by the interfacial defect characteristics. A clear evidence of these defect states at the polymer-polymer interface is revealed using the time and frequency domain photocurrent measurements.

The experimental observations resulting from photoexciting conducting polymer/bR under different bias conditions highlight the effects arising from complimentary processes in the two components. Oriented bR on a conducting polymer substrate forms a unique hybrid system where the possibility of changing the oxidation state of the polymer electrochemically is coupled to the optically activated proton gradient in the bR side. The internal conversion of the intermediate deprotonated M state of bR and the proton transfer/transport can be controlled by the electrochemical reactions at the interface and leads to interesting opto-electrical features in the process.

In CP/nanoparticle systems, a general feature of efficient photocurrent spectral response corresponding to nanoparticle and an appreciable EL response corresponding more to the active polymer are observed in the devices which results in a dual-function single device with wide separated spectral windows for operation.

Contents

Chapter 1

Conjugated Polymers.

1. 1 History of conjugated polymers

Polymers are long chain macromolecules, made of repeating monomeric units, with a large molecular weight (> 10000) [1]. Polymers (conjugated and nonconjugated) are traditionally known for electrically insulating properties. Since the first report of doping of polyacetylene in 1977 by A. J. Heeger, A. G. McDiramid and H. Shirakawa (Nobel prize in 2000) [2-4], conjugated polymers, i.e.: polymers with alternating single and double bonds, have been studied extensively as a novel class of electronic materials. Some of the common features of π- conjugated polymers as compared to conventional sigma (σ)-bonded nonconjugated polymers are that they have small band gaps, relatively large electron affinities and small ionization potentials, which result in low energy excitations. As a consequence, conjugated polymers are suitable for a wide range of electronic and optical applications. The conductivity of a conjugated polymer can be increased by over 10 orders of magnitude upon doping, undergoing an insulator to metal transition. For example, the room temperature conductivity of polyacetylene changes from ~ 10^{-13} – 10^{-5} S/cm to greater than 10^{5} S/cm upon doping with iodine [5-8], a value close to the conductivity of copper (~ 5×10^{5} S/cm) (Fig. 1. 1). Combining the novel electronic and optical properties of modern solid-state materials with the strength, flexibility and processability of conventional plastics, conjugated polymers have shown a tremendous potential for technological application. Conjugated polymers have been used successfully as active materials in thin film transistors (TFT) [9-11], light emitting devices (LED) [12-15], photodiodes (PD) [16], photovoltaics (PV) [17-19] and integrated circuits (IC) [20-22] in their undoped nonconductig form. In their conducting states, conjugated polymers were used as electromagnetic shielding [23]material and as electrodes in devices [24-26].

The discovery of electroluminescence (EL) in an undoped conjugated polymer thin film [12], sandwiched between electrodes in 1990, motivated many

researchers in studying the semiconducting properties of the conjugated polymer even though the polymer diodes were fabricated and characterized in the 1980s

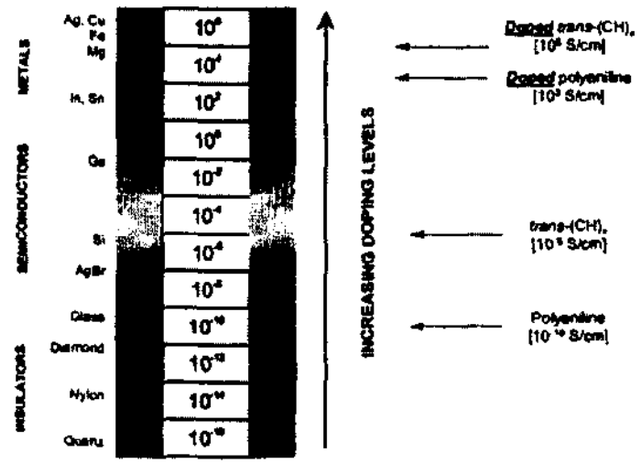

Fig. 1. 1. *Conductivity of conjugated polymers [3].*

[27, 28]. This was largely motivated by the ease with which thin semiconductor films can be made by solution processing and the ability to tune the semiconductor energy gap by grafting chemical substituents to the polymer backbone.

The conjugated polymers consist of alternate single and double carbon – carbon bonds. The conjugation arises due to its ability to swap positions of single and double bonds and end up with a structure that still satisfies the chemical bonding requirements for carbon. Carbon – carbon double bond formation is as described below: sp^2 "hybrid" orbitals were formed by combining two of the three 2p orbitals on each carbon atom with the 2s orbital of the same atom. These orbitals lie in a plane, directed at 120^0 to one another, and form three σ molecular orbitals with neighboring atoms, including neighboring carbon. The third p orbital of the carbon atom, p_z, is orthogonal to the other hybrid orbitals. It overlaps with the p_z orbital of neighboring carbon atoms to form a pair of so called π molecular orbitals that are spread out or delocalized over the polymer chain. The lower energy π (or bonding) orbitals are the valence band (VB) while the higher energy π^* (or antibonding) orbitals form the conduction band (CB). In order to use these

materials in semiconducting devices, the σ bonds should be much stronger than the π bonds (so that they can hold the molecule intact even in their excited states)

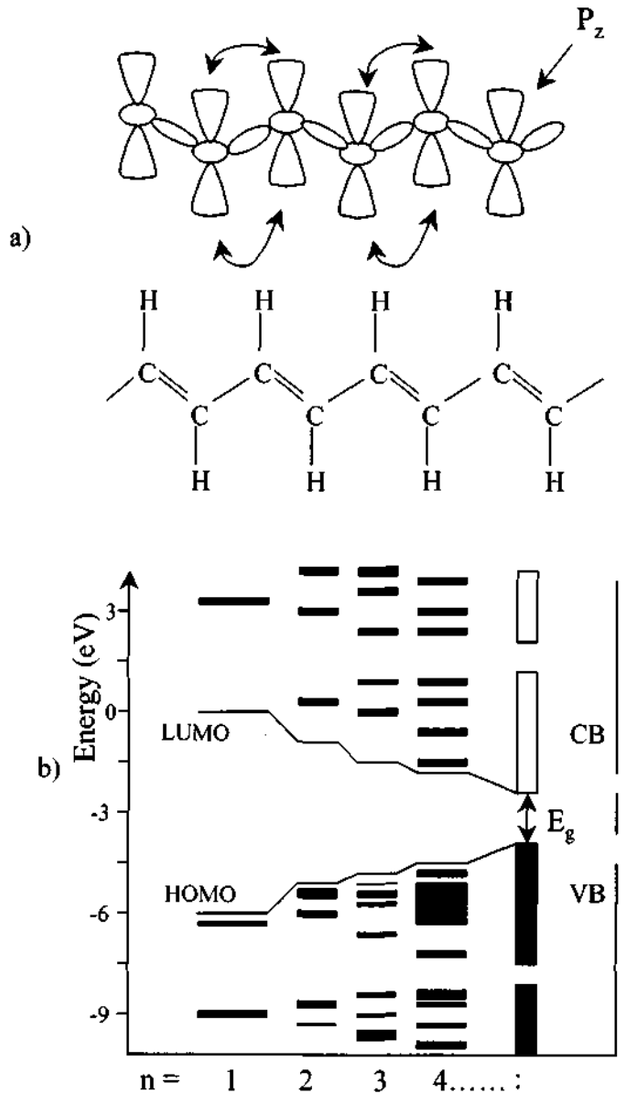

Fig. 1. 2 a. *The schematic of σ - bonding (linear overlap) and π - bonding (lateral overlap) in polyacetylene,* **b**. *The schematic of HOMO – LUMO energy levels of single molecule and many molecules[28 a].*

and the π orbitals on neighboring polymer molecules should overlap with each other so that electrons and holes can move in three dimensions between molecules.

The molecular orbital theory defines that when two atoms bond to form a molecule, the atomic orbitals overlap to form molecular orbitals (bonding and antibonding). The electrons fill these molecular orbitals according to the Pauli exclusion principle. The energy level difference between the highest occupied molecular orbital (HOMO) and lowest unoccupied molecular orbital (LUMO) is assigned as the energy band gap of the material. The HOMO – LUMO level is analogous to the valence band and the conduction band of inorganic materials. The transport properties of such conjugated polymers are similar to amorphous semiconductors.

1. 2 Physics of semiconducting conjugated polymers

1. 2. 1 Transport properties

There are different viewpoints on the transport properties of the undoped conjugated polymers. Polymer transport properties are normally described on the basis of both microscopic and macroscopic models. These models are based on charge transport in low-dimensional systems and also include the disordered nature of the polymer system. The macroscopic aspect of the electrical transport closely resembles the treatment used for amorphous semiconductors. Some of these issues will be discussed in this section.

In inorganic semiconductor crystals like silicon or germanium, the strong coupling between the atoms and the long-range order lead to the delocalization of the electronic states and the formation of allowed valence and conduction bands, separated by a forbidden energy gap. By thermal activation or photo-excitation, free electrons are generated in the conduction band, leaving behind positively charged holes in the valence band. The transport of these free charge carriers is described in the quantum mechanical language of Bloch functions, k-space, and dispersion relations [29].

Structural or chemical defects in the crystal introduce states in the forbidden energy gap, spatially localized at the defect. A mobile carrier from the transport band may get trapped at such a defect state, and will not contribute to the conductivity, until it is released again. In addition to such delocalized band transport with multiple trappings, carriers may also tunnel directly from one localized state to another when the electronic wave functions of the defect states

have sufficient overlap. The carrier may overcome the energy differences between the defect states by absorbing and emitting phonons. [30-32]. Hopping from a localized state j, to a state i, takes place at a phonon frequency ν_0, corrected for a tunneling probability and the probability to absorb a phonon for hops upward in energy [33]:

$$W_{ij} = \nu_0 \exp(-2\gamma R_{ij})$$
$$= \nu_0 \exp\left(\frac{-(\varepsilon_i - \varepsilon_j)}{k_B T}\right) \quad \varepsilon_i > \varepsilon_j \qquad (1.1)$$
$$= 1 \quad \varepsilon_i < \varepsilon_j$$

Here γ is the inverse localization length, R_{ij} is the distance between the localized states, and ε_i is the energy of the state i. Since the hopping rates are strongly dependent on both the positions and the energies of the localized states, hopping transport is extremely sensitive to structural as well as energetic disorder [34, 35]. This kind of transport process is also observed in amorphous semiconductors, like amorphous silicon (a-Si), and the transport property of conjugated polymers is similar to amorphous semiconductor.

Amorphous semiconductors are materials that lack long range periodic ordering of their constituent atoms. The lack of long range order introduces a range of localized states at the extremities of the electron and hole bands of an amorphous semiconductor. These localized states (tail states) are characteristic features of disordered solids and have a determining influence on electronic transport and related properties. It is these tail states which lead to new forms and mechanisms of transport that are not generally found in the crystalline systems. At intermediate and high temperatures (> 150 K) the excess carriers interact with the tail states by a continuous process of trapping and thermal release. In this multi-trapping mode the observed transport takes part in the extended states, but the carrier tail state interaction critically determines the propagation of the injected carriers. At lower temperatures (< 80 K) the excess charge carriers move through the localized tail states by phonon assisted hopping. The material abundantly used in these kinds of studies is hydrogenated silicon (a-Si) based materials. After the first results of transport property of amorphous semiconductors in 1957 [36], the amorphous

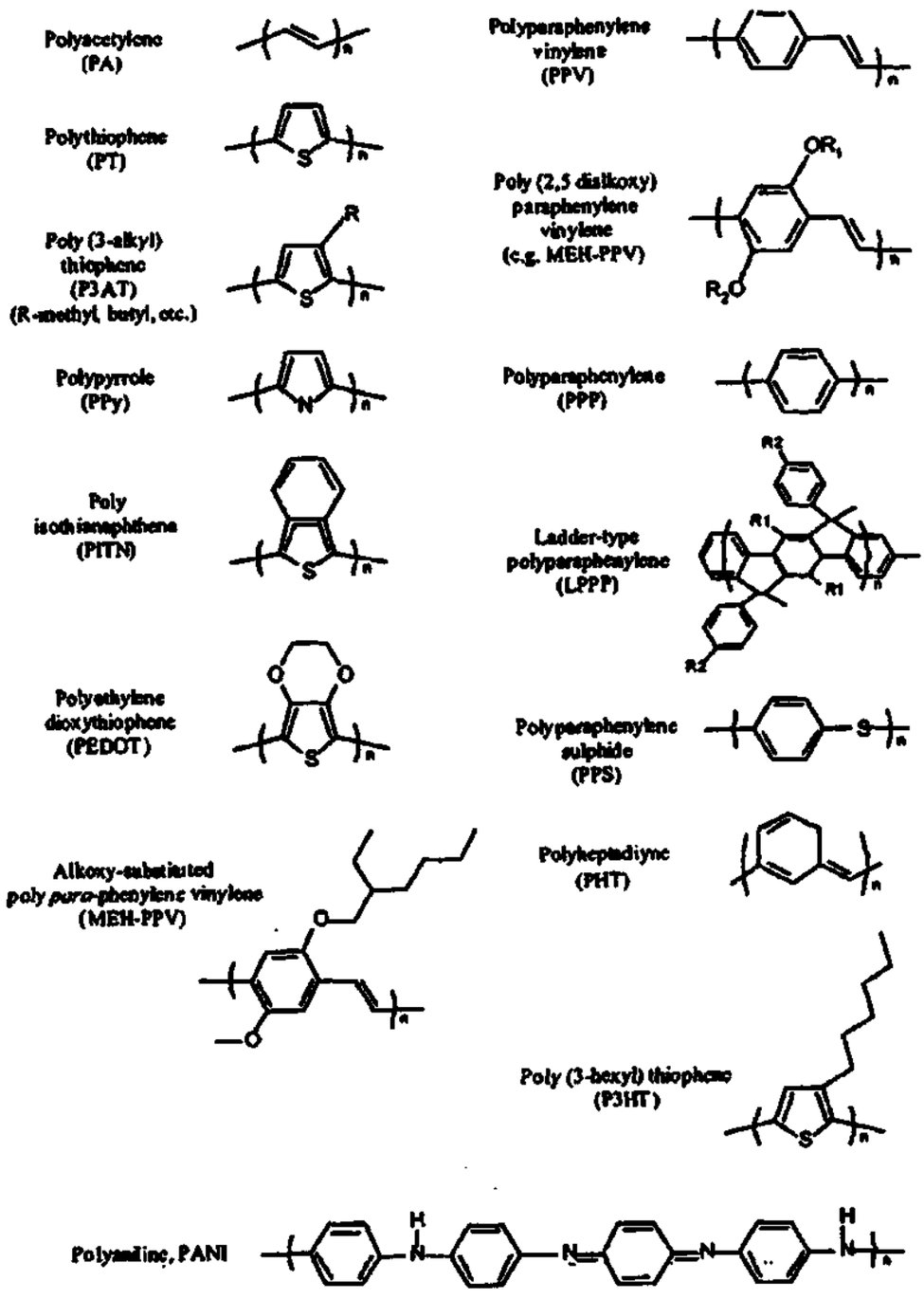

Fig. 1. 3 *The chemical structure of examples of conjugated polymers[2].*

semiconductor approach was extended to other disordered systems such as molecular solids.

In organic solids, intramolecular interactions are mainly covalent, but intermolecular interactions are due to much weaker van der Waals and London forces. As a result, the transport bands in organic crystals are much narrower than those of their inorganic counterparts and the band structure is easily disrupted by introducing disorder in the system. Thus, even in molecular crystals, the concept of allowed energy bands is of limited validity and excitations and interactions localized on individual molecules play a predominant role. The common electronic feature of many organic pigments is the π-conjugated system, which is formed by the overlap of carbon p_z orbitals. Due to the orbital overlap, the π electrons are delocalized within a molecule and the energy gap between the highest occupied molecular orbital (HOMO) and the lowest unoccupied molecular orbital (LUMO) is relatively small, i.e., with transition frequencies within the visible range. The chemical structures of some π-conjugated polymers are given in Fig. 1. 3. In the chemical structure formulae, the π-electrons are represented by double bonds (in phenyl groups, the double bonds are often replaced by circles, to emphasize the delocalized nature of the π-electrons). The low coupling between the molecules in the solid state ensures that the carriers in these materials are strongly localized in a molecule. Transport occurs via a sequence of charge transfer steps from one molecule to another, similar to the hopping between defect states in inorganic semiconductors.

Different models based on rather different microscopic approaches have been used to explain the temperature dependence conductivity of conjugated polymers. The most commonly invoked models are three dimensional variable range hopping with a Coulomb gap in the density of states near the Fermi level [37], quasi one dimensional variable range hopping model [38, 39] or charging energy limited tunneling [40, 41].

1. 2. 2 Photoexcitation

In inorganic semiconductors, the photogeneration of charge involves the excitation of an electron from the valence band into the conduction band. Due to the delocalized nature of the electronic states and screening effects, the Coulomb

interaction within the resulting electron-hole pair is weak and the carriers are either free or form very weakly bound excitons of the Mott-Wannier type [29]. In molecular systems, the primary optical excitations are localized on a single chromophore. Due to this confinement, and due to the low dielectric constant in organics, the Coulomb interaction between the electron in the LUMO and the hole in the HOMO is strong and the exciton is of the Frenkel type. Since the HOMO and LUMO vary for different chromophores in the disordered material, the excitons may relax in the course of a random walk to chromophores where the energy is low, a process known as spectral diffusion. This results in a red shift of the emission spectrum with respect to the absorption spectrum. The photogeneration of free carriers is an indirect process, requiring the dissociation of excitons into electrons and holes on different chromophores. Due to the high exciton binding energy (typically 1 eV), photoconduction in molecular systems commences from about 1 eV below the absorption edge.

In conjugated polymers, the π-conjugated system extends over the whole polymer chain, thus allowing for delocalized states in one direction. Therefore conjugated polymers were initially regarded as one-dimensional semiconductors. In their pioneering work Su, Schrieer, and Heeger [42] studied the interaction of an excitation with an ideal one-dimensional lattice, neglecting Coulomb interactions and disorder effects. They found that, in addition to direct electron and hole excitations across the semiconductor band gap, the one-dimensional system could support a host of exotic carrier types, like solitons (topological defects without charge, with spin 1/2), polarons (electrons and holes, self-trapped by carrier-lattice interactions), soliton-polarons (charged topological defects without spin, self-trapped by carrier-lattice interactions), bipolarons (two carriers with charge of the same sign, bound by lattice distortion), and polaron-excitons (two carriers with charge of the opposite sign, bound by lattice distortion) [42]. In this one-dimensional semiconductor picture, the red shift between absorption and emission is attributed to the creation of self-trapped polarons after the initial generation of free carriers. The energy shift is then a measure for the self-localization energy of the polaron. One of the major arguments in favor of the one-dimensional semiconductor picture for conjugated polymers has been the coincidence of the

onset of photoconductivity with the onset of optical absorption [43], which indicates the absence of a sizeable exciton binding energy.

On the other hand, spectroscopic studies of conjugated polymers show many features that are characteristic for disordered molecular systems [44]. Among these studies are site-selective fluorescence experiments [45] (where the emission spectrum is monitored as a function of excitation in a narrow spectral window) and in time-resolved photoluminescence experiments [46]. Both the spectral and the time dependence of the emission indicate that the primary excitation in a conjugated polymer is a neutral exciton localized in a chromophore, executing an incoherent random walk between chromophores. The chromophores may be identified with segments of the polymer chain, separated by mechanical and chemical defects (twists, kinks, impurities, crosslinks). Additional experimental proof for this molecular picture is formed by the observation of luminescence quenching by high electric fields [47, 48] (attributed to the dissociation of strongly bound excitons) and the recent demonstration that the photoconduction near the absorption edge is mostly of extrinsic origin, resulting from exciton dissociation at the electrodes [49].

1. 3 Excitons

The primary photoexcited species in a conjugated polymer is a neutral electron hole pair called exciton, which is a result of electron – electron interaction in the excited state of the conjugated polymer. The creation of an exciton was a matter of controversy in early 1990's and has been viewed differently in different conjugated polymers [50].

There are three types of excitons classified by their size. The small radius Frenkel exciton, the large radius Wannier exciton and the intermediate charge transfer exciton. Frenkel excitons are common in organic solids, while Wannier excitons are prevalent in inorganic semiconductors.

From the point of view of binding energies, excitons can be classified as Coulombic excitons and polaronic excitons. In coulombic excitons, the electron and hole pair is bound by their Coulomb interaction. In the spirit of constructing a bipolaron, one can think of constructing a polaronic exciton by coupling two opposite charges thereby confining a segment of the higher energy structure. This

results in a neutral excitation with spin 0 (singlet exciton) or 1 (triplet exciton). The triplets always have lower energies than singlets, but the optical transition between the singlet ground state and the triplet excited state is spin forbidden. If the exciton binding energy relative to the separate charge pair is larger than that of the polaron relative to their free particle bands the optical transitions will be dominated by the excitonic transition rather than the polaron ones. While solitons, polarons, and bipolarons have been widely used to account for the charge transport properties in doped conducting polymers excitons, the primary photoexcited quasiparticles, have been proposed to be responsible for the luminescent properties of some undoped conjugated polymers. The free photocarrier generation in these materials depends on the efficiency of dissociation of such excitons [50].

1. 4 Photogeneration of free carriers

Most conjugated polymers have semiconductor band gaps of 1.5-3 eV, which means they are ideal for optoelectronic devices that work in the visible range of the electromagnetic radiation spectrum. This property of the conjugated polymer prompted research in the area of photovoltaic devices where conjugated polymers are used as the active medium. Photovoltaics are semiconducting materials that absorb light at energies above the band gap, leading to the separation of positive and negative charge carriers. These charges are collected at opposite electrodes, giving rise to an open circuit voltage or with an external load, a photocurrent.

Photogeneration of free carriers in conjugated polymers is a two-step process involving creation of an exciton upon incident photon and subsequent dissociation of these excitons into free electrons and holes. These excitons migrate along the chain before dissociation into free charge carriers. The exciton migration length vary from 5 nm to 10 nm for different conjugated polymers [50]. The intrachain migration results in the lowering of the energy of exciton before it emits or dissociates. The apparent Stokes shift is a measure of the energy loss of an exciton during intrachain migration.

The photovoltaic properties of conjugated polymers differ from that of inorganic semiconductors in different ways and some of them are

1. charge carrier transport proceeds by hopping between localized states, rather than transport within a band, which results in low mobilities.
2. the spectral range of optical absorption is relatively narrow.
3. Absorption coefficients are high (~ 10^{-5} cm^{-1}) so that high optical densities can be achieved at peak wavelength with less than 100 nm thickness.
4. Stabilities of organic materials in harsh environment is a limitation.
5. As one dimensional semiconductors, their electronic and optical properties can be highly anisotropic. This is potentially useful for device design.
6. Low temperature processing.
7. Large area.
8. Soft lithographic techniques.

The exciton dissociation can be achieved by applying external electric field or by an electric field at the interfaces involving conjugated polymer/metal and conjugated polymer/conjugated polymer (having different HOMO and LUMO energy levels). But the transfer of free carriers to the electrode is hindered by the low mobility due to the high density of traps in these materials, which results in reduced external photocurrent conversion efficiencies.

The simplest interface is created at the junction between the electrode and the conjugated polymer [51-55]. Under open-circuit conditions, holes are collected at the high work function electrode (indium tin oxide, ITO), and electrons are collected at the low work function electrode (aluminum). Indeed, the V_{oc} generated by these devices depends upon the work function difference between the two electrodes (Fig. 1. 4). Unfortunately, the exciton-splitting process that occurs at a conjugated polymer–electrode interface is not very efficient and is one of the causes of the low quality of early polymer photovoltaics. Another cause of the very low efficiencies of early devices is the effect of impurities, such as oxygen, which act as traps to the migrating excitons. Single layer devices of this type deliver quantum efficiencies of less than 1% and power conversion efficiencies of less than 0.1%. Attempts to improve the efficiency of the exciton-splitting process depend on the behavior of excitons, when they encounter an interface. The interfaces will enhance the electroluminescence property or photovoltaic property depending on the processes involved at the interface when an exciton reaches the interface. The processes involved at the interfaces are

1. the exciton is transferred to the second material where it may decay radiatively (giving the luminescence properties of the second layer) or non radiatively
2. the exciton dissociates by transfer of a single charge to the second material, leaving behind an opposite charge in the first material

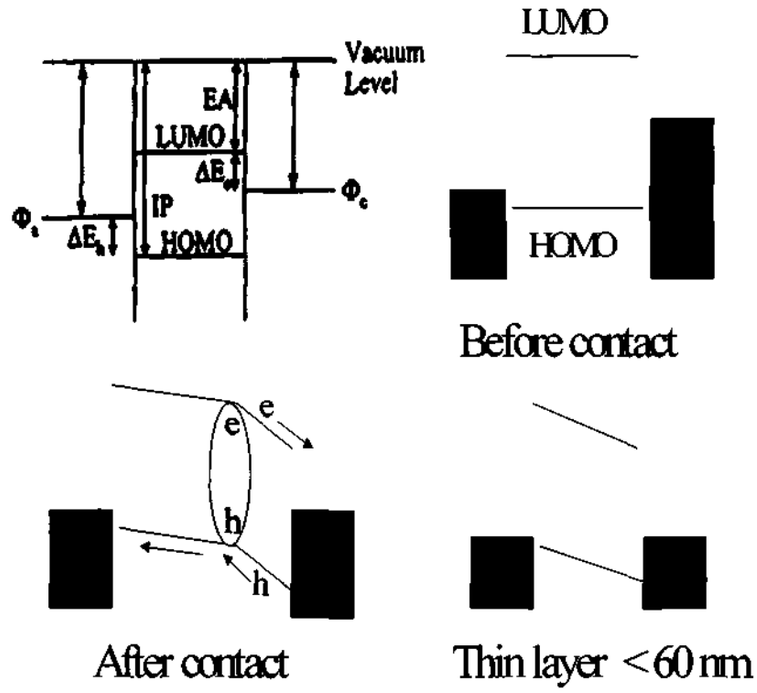

Fig. 1. 4 *Schematic of the energy levels of a single layer conjugated polymer device. IP-ionization potential, EA – electron affinity, ϕ_a and ϕ_c are the workfunction of the anode and the cathode respectively.*

3. the exciton remains in the first material where it decays radiatively (giving luminescence characteristic of the first polymer) or non radiatively.

Early work on molecular semiconductors has demonstrated that the separation of oppositely charged photogenerated carriers is efficient at the interface between certain materials having different ionization potentials and electron affinities. The effect was first reported in the early 1950s: organic dyes adsorbed on the surface of inorganic semiconductors were shown to sensitize this material, giving an additional photoresponse in the spectral range associated with inorganic

photoconductor. There are reports of sensitization of silver iodide (AgI) with a variety of dyes and photocurrent enhancement of cadmium sulfide (CdS) by sensitization with cyanine dyes [56]. It was argued that the conduction band of the dye lies above that of CdS such that the electrons photoexcited in the organic compound are transferred to CdS. Interest was renewed in 1980s when reports of strong photovoltaic effect in a combination of two molecular semiconductors came out. It was proposed that the high local electric field at the heterojunction interface favored the dissociation of excitons that diffuse towards it [57]. There were efforts to see such kind of effects in a conjugated polymer with the conjugated polymer acting as donor [58, 59].

1. 4. 1 Donor-Acceptor bilayer

In these kinds of bilayers the conjugated polymer is used as an electron donor and the organic molecule C_{60} as the electron acceptor [58,59]. The photogenerated exciton moves towards the donor acceptor interface and dissociates to free charge carriers. The mechanism involved in this process is that the highly electronegative C_{60} dissociates the exciton and accepts an electron. The exciton diffusion length limits the performance of such a device. The exciton diffusion length in a conjugated polymer is ~10 nm. So the thickness of such a

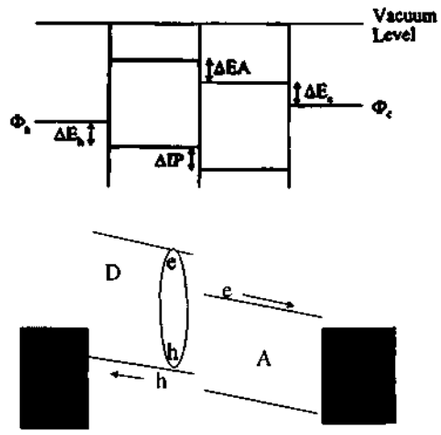

Fig. 1. 5. *Schematic energy level diagram of the donor (D) acceptor (A) bilayer device.*

device should be small enough to make all the excitons reach the interface and have maximum efficiency. It is also to be noted that even though the charge transfer process at the interface happens within nanoseconds, the transport property of C_{60} is poor, which results in low transfer of free charge carriers to the electrode. This increases the probability of recombination. A schematic diagram of the energy level of a bilayer device is as shown in Fig. 1. 5. Other than C_{60}, organic molecules and polymers with high electron affinity were used in such kind of structures. These materials were also used to make laminated bilayer devices. These devices were also limited by the efficiency of exciton dissociation. In order to optimize exciton dissociation, a new concept of interpenetrating network was introduced.

1. 4. 2 Interpenetrating network

Molecular electron acceptors such as C_{60}, polymers such as cyno derivative of poly(phenylene vinylene) and discotic liquid crystalline polymers were used to make an efficient photovoltaic cell [60-68]. New conjugated polymer species were also made that contained electron-donating and electron-accepting species. By creating interfaces among conjugated polymer molecules of differing electron affinities (Fig. 1. 6), it was possible to enhance the probability of electron transfer between molecules. This process (photoexcited charge transfer) caused the bound

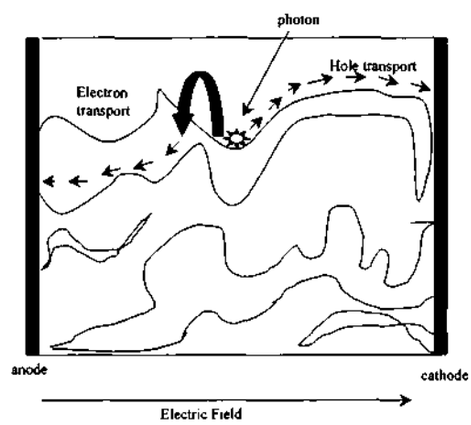

Fig. 1. 6 *Schematic of the process involved in an interpenetrating network.*

charges to separate, and the junction formed at the donor–acceptor interface was analogous to a semiconductor heterojunction.

These heterojunctions work very well at separating excitons that arrive at the junction. Unfortunately, the lifetime of excitons is short, and only excitons that are formed within ~10 nm of the junction will ever reach it. This short exciton range clearly limits the efficiency of these photovoltaic devices. In an attempt to develop a more efficient photovoltaic structure, interpenetrating networks of donor and acceptor polymers have been produced. With these materials, the number of heterojunctions within the polymer blend is greatly increased, and thus the probability that an exciton will encounter a junction and be separated.

1. 4. 3 p-n bilayer devices

The photovoltaic efficiency of the device also depends on the absorption of incident photon and transfer of the free charge carriers to the external circuit. Most of the conjugated polymers have a high mobility for holes in the undoped form and it hinders the effective transfer of electrons to the electrodes. The interpenetrating networks and heterojunction which are made by molecular solids lack high electron transfer rates which results in low efficiency and higher recombination rate due to high density of photoinduced free charge carriers. These problems can be solved by using a polymer which is intrinsically electron transporting and has the energy levels which can form a p-n heterojunction similar to the inorganic one [69, 70].

The n-type conjugated polymers are polymers with a high electron affinity group attached to the main chain [71]. This results in a high electron affinity level and high electron density along the chain. Some of the n type conjugated polymers are shown in Fig. 1. 7.

The properties, which impose some constraints on conjugated based photovoltaic devices, are

1. A strong driving force should be present to break up the photogenerated exciton
2. Low charge carrier mobilities limit the useful thickness of devices. Limited light absorption across the solar spectrum limits the photocurrent
4. Very thin devices mean interference effects are important

a)

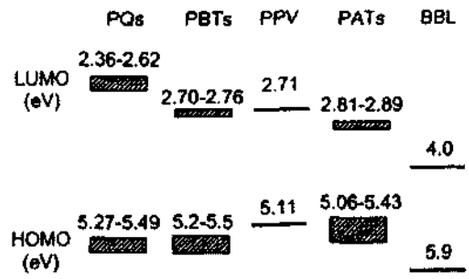

b)

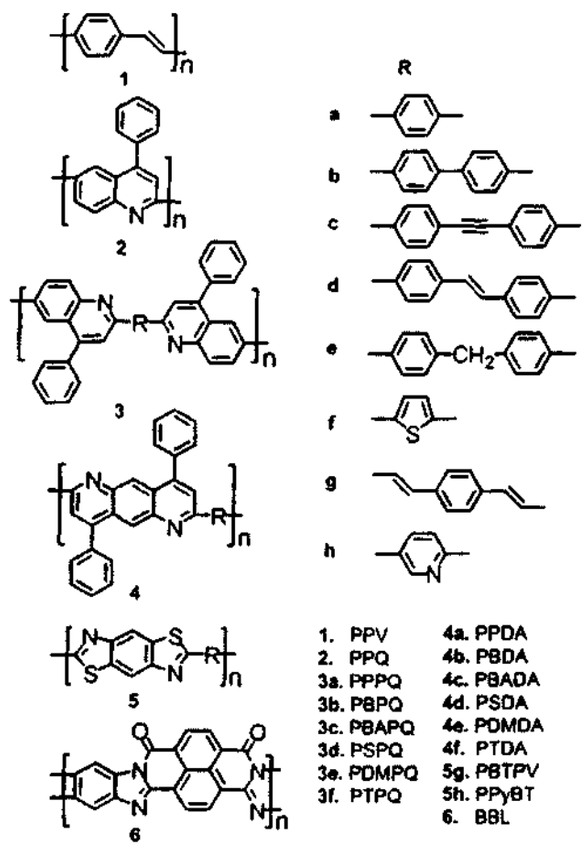

Fig. 1. 7. ***a)*** *The energy levels of Poly quinolines (PQ), Polyanthrazolines (PAT), polybenzobisthiazoles (PBT), poly(benzimidazobenzophenanthroline) (BBL) and poly (phenylene vinylene) (PPV) and* ***b)*** *the chemical structure of these polymers[188].*

5. photocurrent is sensitive to temperature through hopping transport

Some of these problems are addressed in this thesis with intrinsically p-type polymer and n-type polymer forming a bilayer, which has its optical absorption spanning different regions of solar spectrum. The photoelectric measurements were also used to probe the interface of such systems involving a p-type polymer and n-type polymer.

1. 5 Doping of conjugated polymers

Conjugated polymers properties can be changed dramatically by addition (or withdrawal) of electrons to (or from) the conjugated chains with simultaneous intercalation of the compensating counter ions between the chains, a process called doping [8, 72]. However the nature of the insulator to metal transition upon doping, particularly the nature of the metallic state, has been a great controversy [73-76]. Band model was used to explain the conductivity of conducting polymers in the early stage [42].

The approach in the band model is that, a half filled valence band would be formed from a continuous delocalized π -system. This would be an ideal condition for conduction of electricity. However, it turns out that the polymer can more efficiently lower its energy by bond alteration (alternating short and long bonds), which introduces a bandgap of 1.5 eV making it a high energy gap semiconductor. The polymer is transformed into a conductor by doping it with either an electron acceptor or a donor. This is similar to the doping of silicon based semiconductors where silicon is doped with either arsenic or boron. However, while the doping of silicon produces a donor energy level close to the conduction band or a acceptor level close to the valence band, this is not the case with conducting polymers. The evidence for this is that the resulting polymers do not have a high enough concentration of free spins, as determined by electron spin spectroscopy. Initially the free spins concentration increases with concentration of dopant. At larger concentrations, however, the concentration of free spins levels off at a maximum. To understand this it is necessary to examine the way in which charge is stored along the polymer chain and its effect.

The polymer may store charge in two ways. In an oxidation process it could either lose an electron from one of the bands or it could localize the charge over a small section of the chain. Localizing the charge causes a local distortion due a change in geometry, which costs the polymer some energy. However, the generation of this local distortion decreases the ionization energy of the polymer chain and increases its electron affinity making it more able to accommodate the newly formed charges. This method increases the energy of the polymer less than it would, if the charge was delocalized and, hence, takes place in preference to charge delocalization. This is consistent with an increase in disorder detected, after doping, by Raman spectroscopy. A similar scenario occurs for a reductive process.

Doping can be done in many ways and is as follows[2-4]

1. Chemical doping by charge transfer
2. Electrochemical doping
3. Doping of polyaniline by acid base chemistry
4. Photodoping
5. Charge injection at a metal semiconducting polymer interface

In chemical doping typical oxidizing dopants used include iodine, arsenic pentachloride, iron(III) chloride and $NOPF_6$. A typical reductive dopant is sodium naphthalide. The main criterion is its ability to oxidize or reduce the polymer without lowering its stability or whether or not they are capable of initiating side reactions that inhibit the polymers ability to conduct electricity. An example of the latter is the doping of a conjugated polymer with bromine. Bromine it too powerful an oxidant and adds across the double bonds to form sp^3 carbons. The same problem may also occur with $NOPF_6$ if left too long. Chemical doping can be generalized as follows.

a. p- type doping,

$(\pi\text{-polymer})_n + 3/2\ ny(I_2) \rightarrow [(\pi\text{-polymer})^{+y}(I_3^-)_y]_n$

b. n-type doping

$(\pi\text{-polymer})_n + [Na^+(\text{Naphthalide})^*]_y \rightarrow [(Na^+)_y(\pi\text{-polymer})^{-y}]_n + (\text{Naphth})^0$

The oxidative doping of polypyrrole proceeds in the following way. An electron is removed from the p-system of the backbone producing a free radical and a positive charge. The radical and cation are coupled to each other via local resonance of the charge and the radical. In this case, a sequence of quinoid-like

rings are used. The distortion produced by this is of higher energy than the remaining portion of the chain. The creation and separation of these defects costs a considerable amount of energy. This limits the number of quinoid-like rings that can link these two bound species together. In the case of polypyrrole it is believed that the lattice distortion extends over four pyrrole rings. This combination of a charge site and a radical is called a polaron. This could be either a radical cation or radical anion. This creates new localized electronic state in the gap, with the lower energy state being occupied by a single unpaired electron. The polaronic states of polypyyrole is symmetrically located about 0.5 eV from the band edges.

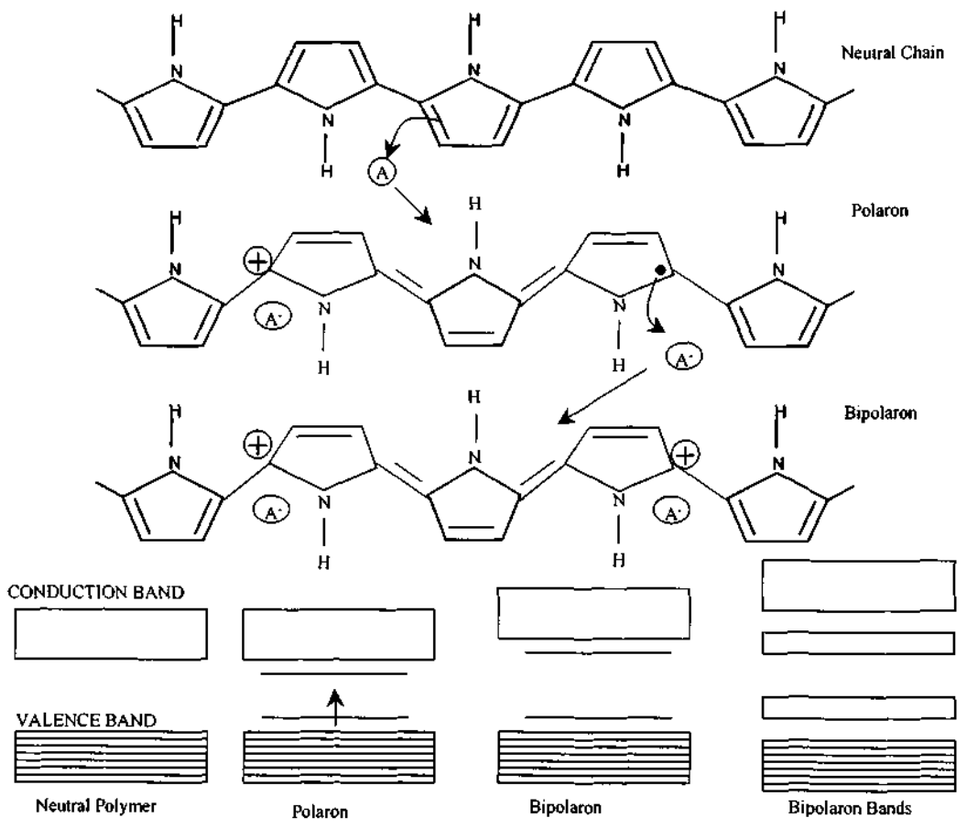

Fig. 1. 8. *Polaron and bipolaron creation upon doping of polypyrrole.*

Upon further oxidation the free radical of the polaron is removed, creating a new spinless defect called a bipolaron. Biploaron formation requires lower energy than the creation of two distinct polarons. At higher doping levels two polarons

combine to form a bipolaron. Thus at higher doping levels the polarons are replaced with bipolarons. The bipolarons are located symmetrically with a band gap of 0.75 eV for polypyrrole. This eventually, with continued doping, forms into continuous bipolaron bands. Their band gap also increases as newly formed bipolarons are made at the expense of the band edges. For a very heavily doped polymer it is conceivable that the upper and the lower bipolaron bands will merge with the conduction and the valence bands respectively to produce partially filled bands and metallic like conductivity. This is shown as in Fig. 1. 8.

Conjugated polymers with a degenerate ground state have a slightly different mechanism. As with polypyyrole, polarons and bipolarons are produced upon oxidation. However, because the ground state structures of such polymers are

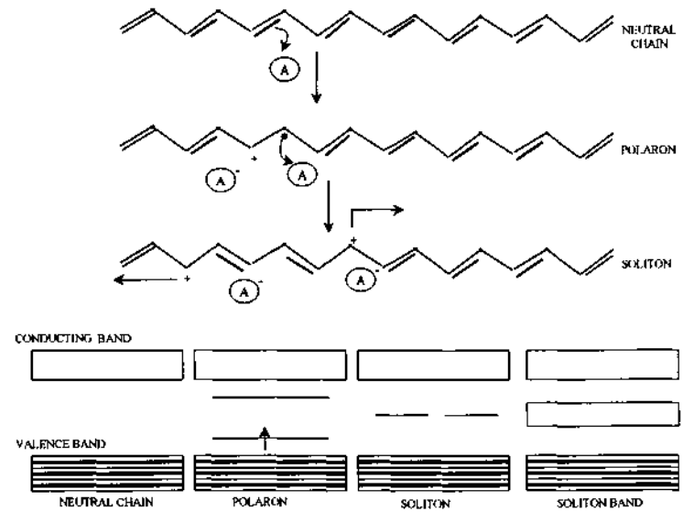

Fig. 1. 9. *The degenerate ground state of polyacetylene and creation of soliton.*

twofold degenerate, the charged cations are not bound to each other by a lower energy bonding configuration and can freely separate along the chain. The effect of this is that the charged defects are independent of one another and can form domain walls that separate two phases of opposite orientation and identical energy. These are called solitons and can sometimes be neutral. Solitons produced in polyacetylene are believed to be delocalized over about 12 CH units with the maximum charge density next to the dopant counterion. The bonds closer to the defect show less amount of bond alternation than the bonds away from the centre.

Soliton formation results in the creation of new localized electronic states that appear in the middle of the energy gap. At high doping levels, the charged solitons interact with each other to form a soliton band, which can eventually merge with the band edges to create true metallic conductivity. This is shown as in Fig. 1. 9.

Although solitons and bipolarons are known to be the main source of charge carriers, the precise mechanism is not yet fully understood. The problem lies in attempting to trace the path of the charge carriers through the polymer. All of these polymers are highly disordered, containing a mixture of crystalline and amorphous regions. It is necessary to consider the transport along and between the polymer chains and also the complex boundaries established by the multiple number of phases. This has been studied by examining the effect of doping, of temperature, of magnetism and the frequency of the current used. These tests show that a variety of conduction mechanisms are used. The main mechanism used is by movement of charge carriers between localized sites or between soliton, polaron or bipolaron states. Alternatively, where inhomogeneous doping produces metallic island dispersed in an insulating matrix, conduction is by movement of charge carriers between highly conducting domains. Charge transfer between these conducting domains also occurs by thermally activated hopping or tunneling. This is consistent with conductivity being proportional to temperature.

In electrochemical doping the electrode supplies the redox charge to the conducting polymer while ions diffuse into or out of the polymer structure from the

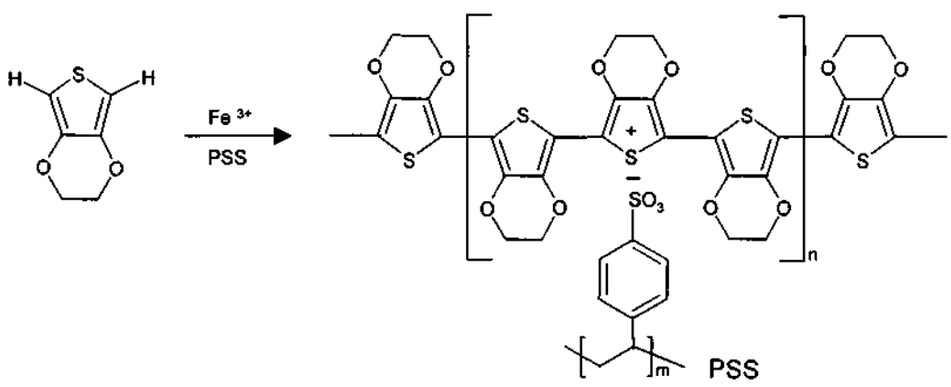

Fig. 1. 10 *Chemical structure of PEDOT:PSS.*

nearby electrolyte to compensate the electronic charge. The doping level is determined by the voltage between the conducting polymer and the counter electrode, at electrochemical equilibrium the doping level is precisely defined by that voltage. It has been shown that in the case of poly (3, 4 ethylenedioxythiophene) (PEDOT) chemically p-doped with poly(styrenesulphonate) (PSS), PEDOT:PSS [77], applying proper voltage in presence of an electrolyte changes the doping state of PEDOT. Since these reactions are often reversible, it is possible to systematically control the electrical and optical properties with precision. These changes in doped state result in eletrochromic behavior. It is even possible to switch from a conducting state to an insulating state [78].

A template-guided synthesis method is used in the case of making conducting PEDOT:PSS (Fig. 1. 10). The molecular template polystyrene sulfonic acid binds the monomer ethylenedioxythiophene to form molecular complexes, which are dispersed in water as colloidal particles. Upon polymerizations, the ethylenedioxythiophene monomers form PEDOT and remain attached to the template to form the template- PEDOT complex. The stabilization against coagulation arises from the coulomb repulsion between particles, which is a result of the surface charge provided by the extra sulfonic acid groups in PSS. This complex is dispersed in water and can be used to make thin films of surface resistance 500 Ωcm^{-2}. The electrochemical doping can be generalized as follows[2]

a. p-type

$(\pi\text{-polymer})_n + [Li^+ (BF_4^-)]sol'n \rightarrow [(\pi\text{-polymer})^{+y}(BF_4^-)_y]_n + Li\ (electrode)$

b, n-type

$(\pi\text{-polymer})_n + Li\ (electrode) \rightarrow [\ (Li^+)_y(\pi\text{-polymer})^{-y}]_n + [Li^+ (BF_4^-)]sol'n$

PEDOT:PSS is used in making electrochromic devices [79, 80].

The temperature dependence of the conductivity showed that the electrical conductivity

$$\sigma(T) = \sigma_0 \exp\left[-(T_0/T)^m\right] \qquad (1.2)$$

where m = 0.5 over the temperature range from 300 K to 6 K. This temperature dependence is characteristic of strongly disordered inhomogeneous systems. Similar behavior has been reported, for example in polyaniline doped with conventional protonic acids [38,39,81], in doped polypyrrole [82,83] and in

microscopically disconnected networks found in polyaniline blends below the percolation threshold [84].

The charge carrier transport mechanism in the case of PEDOT:PSS can be generally explained within the framework of the charging-energy-limited-tunneling model, originally proposed for highly disordered conducting polymers. In this model, conduction is supposed to proceed from tunneling between small conducting grains separated by insulating barriers [82]. This model is an extension of Shengs model of granular metals [40,41]. It focuses on the disorder present in the polymer and the polaronic ground state characteristic of many conducting polymers. According to this model the conducting clusters are highly doped polaronic islands generated by heterogeneities in the doping distribution. The dopant centers act as bridges between neighbouring chains and therefore improve the charge carrier transport. Using this model eq 1.2 is obtained with temperature independent prefactor (σ_0) and the parameter T_0 is given by

$$T_0 = (8U / k_b)(s^2 / d^2)[1/(0.5 + s/d)] \qquad (1.3)$$

where d is the average diameter of the conducting cluster, s is the average distance between the clusters, and U is the energy of coulomb interaction (repulsion) of two electrons at a distance equal to the size of the monomer. The latter had been estimated, for example for polyaniline to be about 2 eV. The T_0 increases 5-6 times with increasing pH in the range 0-3. Such T_0 evolution can be attributed to changes in relative sizes of s and d. Thus increasing pH causes an increase in the ratio of the distance between clusters due the average cluster size, s/d. The model of polaronic clusters embedded in an insulating matrix seems appropriate for PEDOT:PSS because it takes into account both the heterogeneous structure revealed by SEM and possible doping heterogeneities inside the conducting path.

1. 6. Organization of subsequent chapters

The second chapter of this thesis deals with the background information required to understand the photoresponsive bacteriorhodopsin (bR) biomolecule. This chapter describes in brief the history and developments in the bR field. The chapter also describes the photocycle, photoelectric phenomena and the photoinduced proton dislocation mechanism.

Chapter three contains a brief description of materials and methods used to study the different system. The experimental measurement techniques are also explained in detail.

The results and discussions in chapter four are based on the semiconducting properties of undoped conjugated polymers (MEHPPV, P3OT, and BBL). The photocarrier generation and transport of a conjugated polymer bilayer system of a p-type polymer and n-type polymer are discussed in detail and the interfacial processes are studied in detail.

The synergistic processes at the interface of a doped conjugated polymer/bacteriorhodopsin bilayer is probed in detail and the results are discussed in chapter five. The results based on bias dependent stabilization of different states of the bR photocycle, photoelectric spectral responses and history effects are discussed.

Optoelectronic properties of a bilayer consisting of conjugated polymer and nanoparticle are presented in chapter six. This chapter deals with the photocurrent and electroluminescence properties of the hybrid-bilayer structure.

Chapter 2

Bacteriorhodopsin- A photoresponsive biomolecule

2.1 History

Retinal proteins are pigments, which contain vitamin A aldehyde as the chromophore and are invariably bound to biological membranes. The first known retinal protein was the visual pigment, rhodopsin, which exists in the rod photoreceptor membrane of the vertebrate's eyes. Invertebrates also utilize retinal proteins as the visual pigment. Retinal proteins are not unique to the animal kingdom. In 1971, Oesterhelt and Stoeckius discovered a new retinal protein in Halobacterium salinarium [86,87] (formerly Halobacterium halobium), bacteriorhodopsin (bR). Subsequently three additional retinal proteins were found in the same organism.

Under anaerobic conditions and at high salt concentration (about six times that of sea water), the cell membrane of this bacterium grows large patches of a hexagonal two dimensional crystalline lattice, which consists of embedded bR trimers in a lipid bilayer called purple membrane (PM). These extreme brine and high temperature growth conditions of the bacterium together with the crystalline lattice structure of the PM have resulted in bR that has exceptional stability against salt, high temperature, photochemical degradation, other chemicals and extreme pH media [88-91].

2. 2 Function of bR in bacteria

Bacterial cell membrane patches contain four structurally related retinal proteins. These cell membranes are classified into purple membrane and red membrane. Purple membrane contains bacteriorhodopsin, which acts as a light driven proton pump [87]. The remaining three retinal proteins halorhodopsin [92], sensory rhodopsin 1 and sensory rhodopsin 2(or phoborhodopsin) [93] are found in

red membrane. The red membrane also contains the electron transport chain components and the F_0-F_1 complex of ATP synthetase/ATPase.

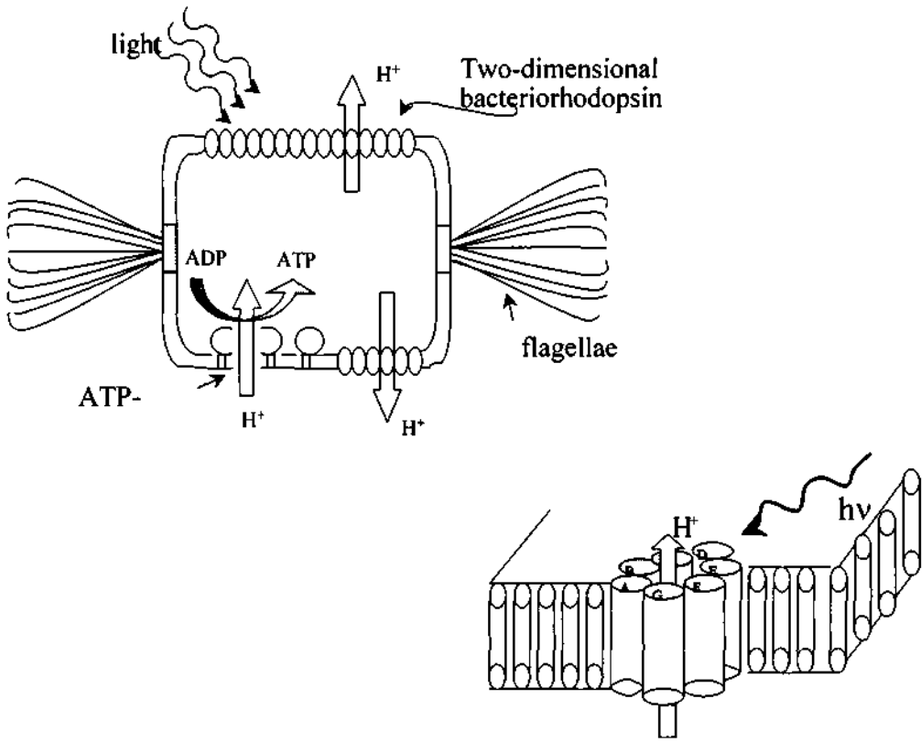

Fig. 2. 1. *a) Scheme of halobacterial cell. Bacteriorhodopsin is a light driven proton pump. The proton gradient generated over the cell membrane energizes the membrane-bound ATP synthase. b) Bacteriorhodopsin consists of seven transmembrane alpha helices (A-G) and an encaged retinylidine residue bound to helix G, which separates the cytoplasmic from the extracellular part of the proton pore.*

Halorhodopsin is a light driven chloride ion pump where rhodopsin 1 and 2 are sensory pigments, which serve photoaxis functions. bR is functionally analogous to the photosynthetic reaction centers of green plants cynobacteria and purple phototrophic bacteria. The eubacteria uses classical photosynthesis based on chlorophyll like pigments and redox chemistry. Archaebacteria use a system of chromoproteins containing retinal as chromophore, which is able to transport ions across the cell membrane upon illumination. Thus light energy is directly converted into electrochemical energy in the form of an ion gradient (Fig. 2.1). The energy so stored is then utilized to power the ATP synthetase, which converts ADP

and inorganic phosphate into ATP [94] in accordance with chemiosmotic theory [95-97]. Bacteriorhodopsin is essentially a stripped down photosynthetic apparatus: protons are pumped by single molecule instead of a chlorophyll–protein supramolecular complex. In brief, Halobacteria utilize a visual pigment to perform photosynthesis.

2. 3 Surface charges and structure of purple membrane

Like other biological membranes, purple membranes have a net negative surface charge of ~ 0.01 charges/Å^2 or 2 electrons per bacteriorhodopsin[98-100]. The negative charges are due to acidic (amino acids) of bR and acidic lipids [101]. The difficulty of a precise determination of the surface charge density has been pointed out recently [102]. The asymmetry of the membrane structure and the difference of the surface charge densities on both sides of the membrane are important points for photoelectric studies [103, 104]. A polarity inversion of the surface charge difference has been estimated by photoelectric orientation studies to occur at pH 5 [105, 106]. The permanent dipole moment connected with the asymmetric surface potential of PM has been estimated to be ~ 10^7 debye [106-108]. These asymmetries are the basis for different experimental procedures for orienting the membrane fragments.

The main constituent of the purple membrane patch is bacteriorhodopsin consisting of a single polypeptide chain with 248 aminoacids. It traverses the membrane in 7 alpha helices. The prosthetic chromophore group is normally all trans retinal, which is covalently bound to the ε-amino group of lysine 216 via a protonated Schiff base. Compared to the absorption of the free protonated Schiff base of all-trans retinal (Fig. 2. 2b) in organic solution (λ_{max}= 440 nm), the binding to the protein shifts the absorption maximum to 570 nm, which is due to the electric field of the charged residues in the neighborhood. This additional spectral shift is called opsin shift and confers the purple color to the protein [109]. The Schiff base proton is directly exchangeable with the external medium (apparent isoelectric potential, pK ≈ 13) without the need of light activation [109,99]. Besides the protein substates, two main forms are distinguished by the light adapted state, bR_{LA}, and the dark adapted, bR_{DA}. The light adapted state contains all trans retinal, whereas the dark adapted state is

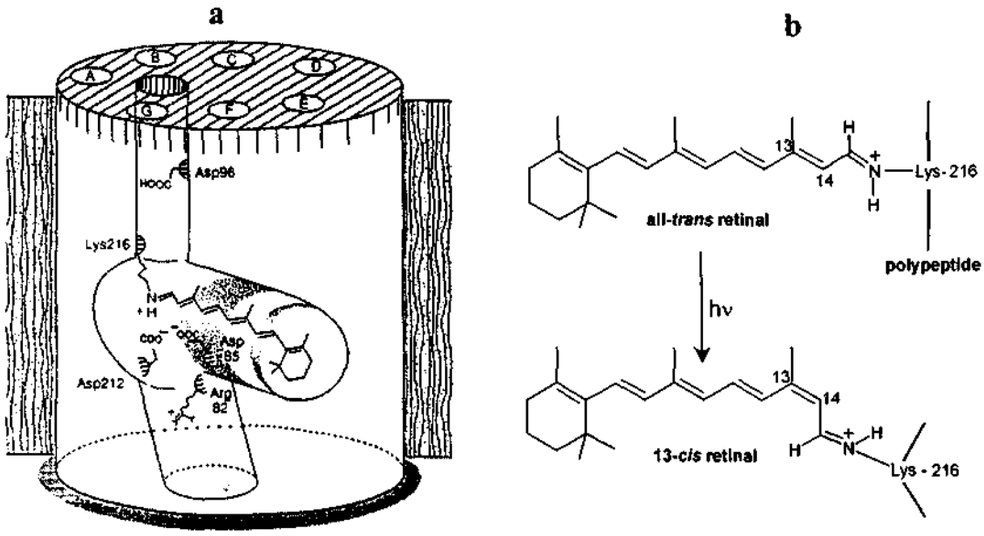

Fig. 2. 2 *a) The cross section of a PM[175] and b) the photoinduced isomerization of retinal.*

(at room temperature) a nearly 1:1 or 2:1 mixture of 13-cis and all-trans retinal in thermodynamic equilibrium [111]. The schematic of the retinyl molecule inside the PM and the isomerization is as shown in Fig. 2. 2.

2. 4 Photoinduced proton transfer

The absorption of light initiates a series of different reactions. This includes isomerizations of the retinal and concomitant conformational changes of the protein, as well as the deprotonation and reprotonation of the Schiff base group. H^+ ejection to external medium (~100 μs) precedes H^+ uptake from the cytoplasm in the 10 ms range at neutral and slightly acidic pH [112]. The transmembrane pumping of protons build up an electrochemical gradient and thereby provides the cell, under anaerobic conditions, with free energy by means of a proton driven ATP-ase [113-116]. The proton pumping capacity does not depend on whether bacteriorhodopsin is in the monomeric state or incorporated into the crystalline array of a purple membrane [117 118]. After a turnover time of approximately 20 ms bacteriorhodopsin at pH 7 relax to its initial state [119]. During the cycling period, protonation and deprotonation of several amino acid residues take place. Some may be arranged as a chain of hydrogen bonds forming a transmembrane H^+ conducting wire [120]. Most probably, all 4 asparates that lies in the inner part of

the protein (Asp^{85}, Asp^{96}, Asp^{115}, Asp^{212}), Arg^{82} and Tyr^{185} are involved in the formation of photocycle intermediates [121-126]. The cycle is mostly characterized by spectroscopically detectable intermediates (Fig 2. 3). However the electrogenic reactions accompanying the photocycle allow a characterization also by its electric response.

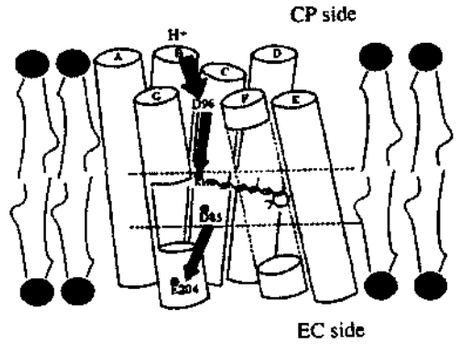

Fig. 2. 3. *The schematic of proton translocation path in PM[174].*

The three dimensional structure of bR has not been determined to the level of atomic resolution. Henderson and co-workers applied Fourier analysis to electron diffraction patterns of purple membrane at low temperature and reported a three dimensional map of bR with a resolution of 3.5 Å in a direction parallel to the membrane plane, but at a lower resolution in the perpendicular direction [127,128]. The proton translocation path in the purple membrane is shown in Fig. 2.3. The chromophore binds to the lysine residue 216 (K216) and a smaller number of key amino acid residues. The residues aspartate 96 (D96) and 85 (D85) are the primary proton donor to the Schiff base and the primary proton acceptor of the Schiff base proton respectively [127, 129, 130]. The D85 is connected to the Schiff base through a hydrogen bonded water molecule and forms a second hydrogen bond with another water molecule [131]. The residue glutamate 194 releases the proton after accepting the proton from Asp 85 through glutamate 204 [132-134]. The distance between D96 and the Schiff base is 12 Å therefore proton transfer between the two binding sites is unlikely to be accomplished in single step. A hydrogen-bonded chain formed by several additional residues and bound water has been suggested as the pathway of possible proton transfer

JNCASR
Acc No 3271
LIBRARY

2. 5 The Photocycle of bR

The absorption spectrum of bR depends on its state of light adaptation. Fully dark-adapted bR contains a mixture of 13-cis retinal and all-trans retinal and its absorption maximum is at λ = 568 nm. When it is light adapted the absorption maximum is at λ = 570 nm and the chromophore is in the all-trans configuration. Upon pulsed illumination, bR undergoes a sequence of chemical reactions during which the absorption maximum shifts continuously. These photointermediates in a cyclic reaction scheme is designated with letters such as K, L, M, N, O, P and the reaction scheme is known as the bR photocycle (Fig. 2. 4) [135-140]. Absorption maximum and a lifetime characterize each of these intermediate states. Many of the steps in this photocycle are reversible with almost equal rates for the forward and reverse reactions. Upon illumination, retinal isomerizes from all-trans to 13-cis conformation with a quantum efficiency of approximately 0.65. This process then deprotonates the Schiff base within picoseconds to form a primary charge displacement state. One proton is released to the extracellular side during the L to M reaction and taken up again from the intracellular side during the decay of N. The proton release precedes proton uptake at neutral and high pH and the sequence is reversed at low pH. Further it has been shown that the step M involves two processes M1 and M2 where the Schiff base switches from the extracellular orientation to the intracellular orientation [141-145]. Unlike typical biological material, PM has high thermal and photochemical stability. Bacteriorhodopsin can retain its natural structure and function at temperatures as high as 140 ^{0}C in the dry state and for pH ranging from 3 to 10 in solution [88]. The proton pumping photocycle of bR can be repeated more than 10^6 times [146]. This unusual stability coupled with unique photochemical and photophysical properties has made bR the most promising biological material for applications such as photoelectric and holographic devices. The work presented here concentrates on the photoelectric properties of bR.

A dynamic model, based on reaction kinetics has explained the photocycle of bR. The dynamic model is based on the population of each state and rate of photoelectrochemical reactions during the photocycle, which involve the rate constants of the chemical reactions.

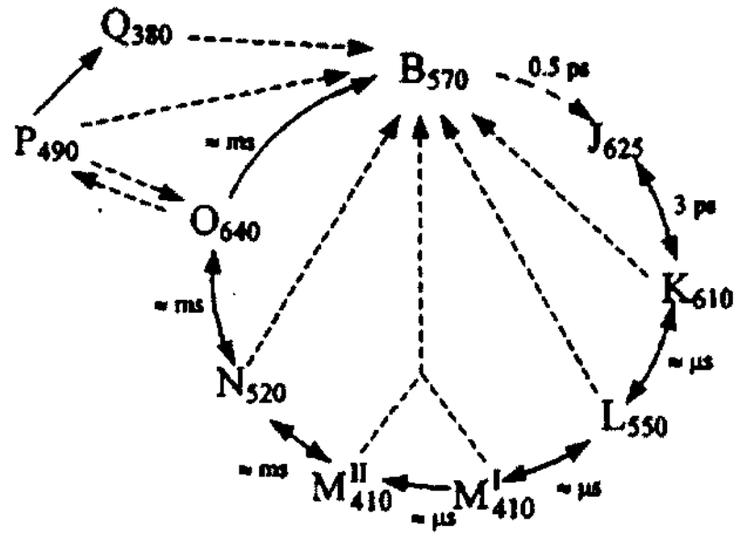

Fig. 2. 4. *Detailed description of various states in the photocycle of bacteriorhodopsin[204].*

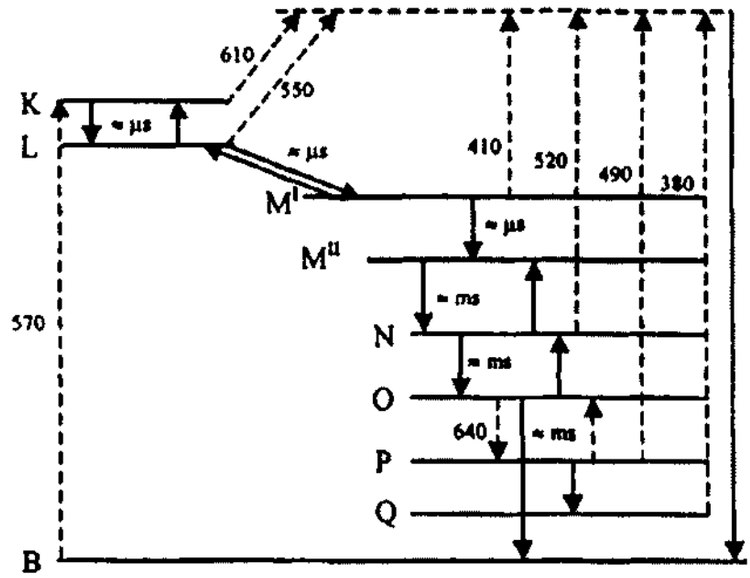

Fig. 2. 5. *Schematic of lifetimes of different states in the bR photocycle[204].*

Optically induced population changes in molecular systems such as bR, induce changes in the absorptive and dispersive properties of the medium, thereby exhibiting spatial light modulation and optical bistability. Investigations of the complex photochemical cycle of bR molecules have been based on an extremely simplified photocycle considering a two level model with B and M states or a three level model with B, K and M states only. The lifetime of each state is schematically shown in Fig. 2. 5. The lifetime of the M state is defined as the time taken by that state to relax back to the ground state B without any external perturbations. The reported life time of the M state of a wild type (directly extracted from Halobacterium Salinarium cell culture in laboratory condition similar to the growth of this bacteria in nature) bR is 5 ms. The life time of the M state can be increased by preventing the reprotonation of retinal Schiff base from the cytoplasmic side. A mutation of the protein at the Asp 96 site results in a life time of ≈5 s for the M state of bR photocycle.

2. 6 Photoelectric effect in bR

The first demonstration of photoelectric effect in bR was performed in 1974 [147,148]. In this experiment oriented purple membrane (PM) fragments were incorporated into a planar black lipid membrane and demonstrated an electric potential across the membrane during continuous illumination. Since then, there were many studies to understand the mechanism and improve the photoelectric properties of PM. Photoelectric studies of the PM, especially the transient photoelectric signals from the charge separation and displacement after photoexcitation of bR, have provided information for understanding the molecular mechanism of the bR proton pump [149, 150]. On the nano and microsecond time scales, two fast photoelectric components referred to as B1 and B2 were observed by flash photolysis (where B1 and B2 are conventional name given to the photoelectric signal in nano and microsecond time respectively). The negative polarity component B1, with a rise time of less than microseconds, is believed to be associated with the initial proton-pumping event. i.e. charge separation as a result of the light induced retinal isomerization from all-trans to 13-cis in bR [151, 152]. The positive polarity component B2 on the microsecond time scale is due to the vectoral pumping of protons from Schiff base to solution [153]. On the

millisecond time scale a pH dependent component B3 was observed and its origin is not clear [154]. The differential photocurrent component D1 (light on component) and D2 (light off component) of bR under green light excitation is an important parameter for electronic device applications. A schematic of the photoelectric response is shown in Fig. 2. 6. Moreover, the magnitude and efficiency of the differential photocurrent that can be generated from bR films is quite dependent on the bR orientation [155-157].

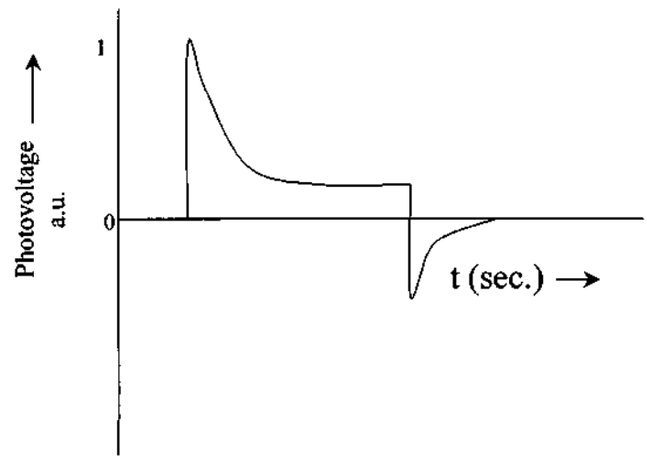

Fig. 2. 6 *Schematic representation of bR photoelectric response for a long duration pulse.*

2. 6. 1 Orientation techniques

The methods recently used for assembling the PM in the solid state or into solid supports for device applications, have included Langmuir Blodget (LB) deposition [157-160], electric field sedimentation (EFS) [161], chemiadsorption self assembly [162, 163], electrostatic layer by layer adsorption (LBL) [164-166], antigen antibody molecular recognition [155,156], sol gel encapsulation [167, 168] and using polymers as immobilizing matrices [169, 170]. These methods have been used to provide preferred orientation and tailorability of the bR depending on the property and application of interest. The photoelectric conversion efficiency of a bR based device largely depends on the degree of orientation of bR in the film. Orientation methods such as LB EFS and LBL are used for this purpose.

2. 6. 2 The mechanism of differential photocurrent in bR

There are conflicting opinions regarding the actual molecular mechanism of the differential photocurrent. One is that charge displacement within bR induces the differential current on the electrode adjacent to the bR molecule when bR is excited with light [155, 156]. Another opinion is that differential current of bR results from an electrochemical current induced by local pH change [171-173]. Both pulsed and continuous wave laser photoexcitations on different time scales showed an identical polarity change with pH for slow B3 photocurrent components under pulsed laser excitations and D1 differential component from CW laser excitation. This observation leads to the conclusion that the origin of D1 photocurrent is same as that for B3. Since B3 component results from the proton accumulation near the electrode/bR interface, D1 was inferred to the change in proton concentration at the electrode/electrolyte interface as a result of proton pumping of bR. This leads to the formation of a transient proton capacitor between the working and counter electrodes. The charging and discharging process of the proton capacitor produces the differential photocurrent response of bR.

The M state is the intermediate state which has a characteristic absorption peak at λ = 412 nm, which is well separated from the ground state B absorption peak at λ = 570 nm. It has many technological applications and plays an important role in the photocycle of bR.

2. 6. 3 Importance of M state

The above-mentioned mechanism also proves that the M state of bR plays an important role in determining the differential photocurrent response [174-176]. Photochromic devices based on bR has been developed due to the large shift in absorption peak and long life time of the M state. The devices made of wild type PM, show a photoeletcric spectral response in the wavelength range 500 nm < λ < 650 nm of the visible spectrum. But a device, with the PM in the M state, shows a photoelectric spectral response in the 350 nm < λ < 500 nm range. M state is usually achieved in presence of a high pH electrolyte [177, 178] or by growing it on an ionic surfactant [176] or by site specific mutation like D96N mutation [179]. In the high pH method and in the ionic surfactant method, the M state life time is

enhanced due to the reduction in proton uptake in presence of an alkaline electrolyte. In the case of D96N mutant the Asp 96 is replaced by asparagines in which, the second carboxyl group is substituted by a carboxyamido group, which changes the source of reprotonation of Schiff base from Asp 96 to the local medium.

The work presented in this thesis provides an easy and novel way to produce the M state by orienting bR on a doped conjugated polymer-blend surface. Varying the polarity and magnitude of the external bias can change the conducting polymer surface potential. The doped conjugated polymer has high conductivity in the oxidized form and low conductivity in the reduced form. The orientation is basically possible due to the anionic surfactant component in the polymer-blend. This allows the positively charged extracellular side of bR to grow on it. This approach also reduces the degradation effect, which is typically observed in a bR/electrolyte system.

Chapter 3

Materials and methods

3. 1 Materials

The conjugated polymers used were undoped poly(3-alkyl thiophenes) (P3AT's) such as poly(3-octyl thiophene) (P3OT) and poly(3-hexyl thiophene), poly(2-methoxy, 5-(2-ethylhexoxy)-1, 4-phenylene vinylene) (MEHPPV), poly(benzimidazobenzophenanthroline) (BBL) and 6, fluoro poly-(benzoxazole-bioxydecyl) (6FPBO) and poly(3,4 ethylenedioxythiophene) (PEDOT) doped with poly(styrenesulphonate) (PSS). The inorganic nanocrystallites used were cadmium sulfide of size 22 Å (CdS-22) and 44 Å (CdS-44). The biomolecule was a retinal protein bacteriorhodopsin (bR) embedded in purple membrane of Halobacterium Salinarium.

3.1.1 P3ATs

Three general methods for polymeric synthesis of P3ATs have been developed over the last 15 years [180]. These include electrochemical polymerization, oxidative polymerization of 3-alkylthiophene by oxidants such as ferric chloride ($FeCl_3$) and polymerization by catalyzed dedihalogenation of 2,5, dihalo-3-alkylthiophene such as nickel (Ni) catalyzed coupling of thiophene Grignard reagent or dihalothiophene monomers. The regioregularity in P3AT can be achieved in two ways head to head (HH) or head to tail (HT) depending on 3-alkyl substituent. Synthesis of HT regioregular P3AT is typically done using a Ni catalyst coupling polymerization of a regiospecific thiophene Grignard reagent. The polymer used here is obtained commercially from Aldrich, USA. The organo zinc reagents formed by reacting Ricke Zinc with 2,5 dihalothiophenes was used for synthesis of this polymer [181]. The nuclear magnetic resonance (NMR) studies of these P3ATs have shown a regioregularity of more than 98.5%. These P3AT's were soluble in common organic solvents such as chloroform or p-Xylene. The simple cast films of all regioregular P3ATs have been shown to have a crystalline self organized lamellar morphology with three dimensional ordering of the polymer chains while that of the regiorandom P3AT has a totally amorphous phase by the X-ray diffraction analysis. The X-ray diffraction showed a strong

first, second and third order diffraction at 2θ angles of 5.4, 10.8, and 16.3^0. This corresponds to an interlayer d – spacing of 16.36 Å of the self organized lamellar structure. The UV-VIS absorption spectrum of thin films showed an absorption edge of 610 nm compared to 560 nm of regiorandom P3AT implying a larger proportion of the longer conjugation length polymer chain. The basic inherent electrical and optical properties of the P3AT are shown in Table 3. 1. P3HT was also prepared using electrochemical polymerization of monomers obtained from commercial sources. The chemical structure of P3OT and HOMO, LUMO levels are as shown in Fig. 3. 1

3.1.2 MEHPPV

MEHPPV used here was made by Prof Ramakrishnan's group in IPC, IISc. The synthesis of MEHPPV has been done using thermal elimination of the precursor. The sulfonium chloride polyelectrolyte precursor of MEHPPV was prepared according to a slightly modified procedure of Wessling et al [182, 183]. The polyelectrolyte was treated with varying mole ratios of sodium acetate – methanol in acetic acid solution at room temperature to give required neutral precursor polymer [184]. MEHPPV in Xylene is thermally eliminated and is used to make thin films. The chemical structure and HOMO, LUMO levels are as shown in Fig. 3. 1 The electrical and optical properties of MEHPPV are summarized in Table 3.1.

3.1.3 BBL

BBL belongs to a family of heat resistant high temperature ladder type polymers, which have wide applications in electronics, aircraft and aerospace vehicles. This polymer was obtained from Polymer Branch, Wright Patterson Air Force, and was synthesized according to the procedure given by Arnold and vanDeussen in 1969 [185,186]. The central principle of the synthesis was the condensation of tetrafunctional monomers, in this case an aromatic tetraamine(1,2,4,5-tetraaminobenzene) with naphthalene-1,4,5,8-tetracarboxylic anhydride in arpotic medium such as polyphosphoric or sulphuric acid. In order to largely avoid the undesired formation of branched and cross linked structures, special reaction conditions were introduced. Rigid chain structures containing

aromatic or heterocyclic rings together with such chemical factors as introduction of groups that promote strong primary and Van-der Waals bonding forces, hydrogen bonding, resonance stabilization, molecular symmetry or cross linking have been used to achieve this combination of thermal stability and physical properties in polymers. Unfortunately these structural features which endow the desirable physicochemical properties in thermally stable rigid chain polymers also cause processing difficulties due to insolubility in organic solvents and the extremely high glass transition, softening or melting temperatures (> 250 – 300 ^{0}C). Insolubility of these rigid chain polymers is not simply due to high molecular weight since even their low molecular weight structural analogue or model compounds are equally insoluble in common organic solvents.

Different approaches have been used to the solubilization and processing of rigid chain polymers [187]. One of them was synthetic modification of the basic rigid chain structures by introduction of flexibilizing linkages (eg -O-, -CO-, -CH_2-, -SO_2- etc) or molecular asymmetry (ortho, meta, versus para linkages) into the backbone or addition of bulky side groups to improve solubility. Synthetic routes involving a soluble intermediate or precursor polymer that can be converted to the rigid chain structure after processing by using thermally activated cyclization or similarly simple reactions and dissociation in strong protonic acids such a methane sulphonic acids, chlorosulfonic acid, triflic acid and concentrated sulphuric acid. But these methods result in poor thermal stability, chemical resistance and mechanical properties.

Due to these difficulties, a different approach of solubilizing the polymers in organic arpotic solvents is developed. Here the reversible formation of electron donor-acceptor complexes of these polymers with Lewis acids follows dissolution to form viscous solution, which can be processed by conventional methods. The complexation processes introduce molecules or ions of the complexing agent between chains and add charge to, or distribute charge on the macromolecular chain. The net result of such a process was a net reduction in intermolecular attraction between chains and reduction of chain stiffness allowing solvation of chain by solvent. The feasibility of forming various electron donor acceptor complexes of the heteroaromatic rigid chain polymers with metal halide Lewis

acids (MX_n) were excellent in view of the rich nonbonded electron pair donor sites on the polymer chains such as the heteroatoms.

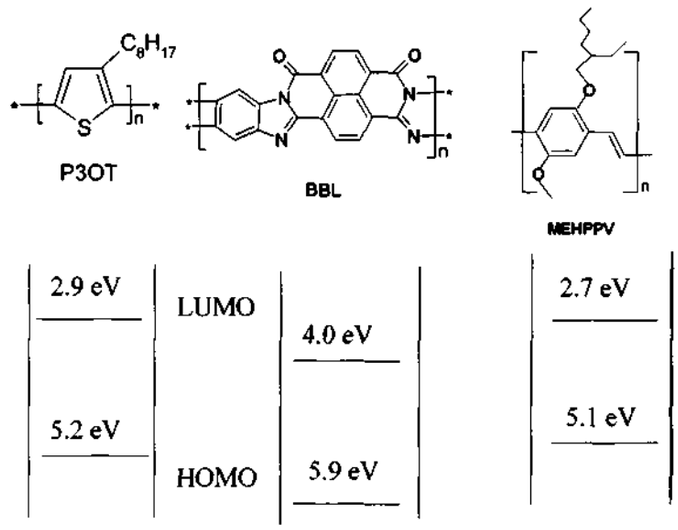

Fig. 3. 1 *The chemical structure of P3OT, BBL and MEHPPV and their LUMO and HOMO energy levels*

CP	transport type	Mobility cm^2/Vs hole	Mobility cm^2/Vs electron	Conductivity S/cm	Band gap eV
P3OT	p -type	$\sim 10^{-1}$	$\sim 10^{-5}$	$\sim 10^{-7}$	~ 2.1
MEHPPV	p - type	$\sim 10^{-2}$	$\sim 10^{-6}$	$\sim 10^{-9}$	~ 2.15
BBL	n-type	~ 10^{-5}	~ 10^{-1}	$\sim 10^{-10}$	~ 1.9

Table 3.1. *Electrical and optical properties of the conjugated polymers(CP)*

(O, S, N, C=O), which contain unshared electron pairs. Here, aluminum chloride in nitrobenzene and gallium chloride in nitromethane were used as the Lewis acids.

The chemical structure and HOMO, LUMO levels are as shown in Fig. 3. 1 The optical and electrical properties [188] are as shown in Table 3.1.

3.1.4 CdS - 44 and CdS - 22

Nanocrystallites of CdS were obtained from Prof D. D. Sarma's group, SSCU. IISc. The synthesis of these nanocrystallites followed a thiophenol route and was similar to the one given by Wang and Herron [189]. First stock solutions were prepared in the following manner. 0. 1 M cadmium salt solution was made by dissolving cadmium acetate ($Cd(CH_3COO)_2$ in methanol and 0.1 M Na_2S solution was made by dissolving 8g sodium sulphide in 50 ml of methanol. 0.2 M thiophenol (PbSH) solution was made from 2.2 ml of thiophenol in 100 ml of methanol. From these stock solutions 50 ml of sodium sulphide solution and 50 ml of sodium thiophenol solution were mixed and stirred. Then 100 ml of cadmium acetate solution was added with continuum stirring of the solution. This resulted in a cloudy yellow solution. The solution was then filtered and suction dried by blowing dry nitrogen to yield dry yellow powders. The particle size could be controlled by varying the relative ratio of sulphide to thiophenol. The S:Ph ratio was 1:2 here S stands for sulphide and Ph for thiophenol. For the larger sized crystallites, the ratio between the sulphide ion and thiophenol was 2:1.

CdS nanocrystallites of two different sizes were synthesized using 1-thioglycerol as the capping agent. The method followed was similar to that reported by Vossmeyer et al[190]. In this case, 2.35 g of Cadmium acetate di hydrate (8.82 mmol), 0.95 g thiourea(12.48 mmol) and 0.95 ml of thioglycerol (10.95 mmol) in DMF was heated to 80° C for about one hour under argon atmosphere. Subsequently about 20% of v/v water was added to the cooled solution followed by refluxing the reaction mixture for about 12-14 hours. Following this, the solution was condensed to about one –tenth of original volume using a rotavapor. The condensed mixture contains nanocrystallites with a wide size distribution as indicated by broad absorption spectra. In order to narrow down the size distribution, a method known as size select precipitation [191] was followed. The larger particles were precipitated gradually by adding drops of acetone leaving behind the smaller particles in the supernatant. This procedure was repeated several times to finally yield crystallites having an average size of about

2.2 nm. CdS nanocrystallites having an average size of about 4.4 nm were synthesized using the same method except the fact that the quantity of thiourea was halved(6.34 mmol) and the solution was refluxed directly without adding water. This method did not require any size selective treatment as the final reaction mixture contained CdS particles with a degree of monodispersity. The nanocrystallites with average sizes of 2.2 and 4.4 nm will be henceforth referred to as CdS-22 and CdS-44 respectively [192].

3.1. 5 PEDOT:PSS

PEDOT:PSS used here was obtained from Bayer AG USA. This was developed during the second half of the 1980s by scientists at the Bayer AG research laboratories in Germany and the backbone structure is as shown in Fig 1. 11 [193]. This polymer often abbreviated as PEDOT was initially developed to give a soluble conducting polymer that lacked the presence of undesired α,β- and β, β couplings within the polymer backbone. This polymer was prepared using standard oxidative chemical or electrochemical polymerization methods. PEDOT was initially found to be an insoluble polymer, yet exhibited some very interesting properties. In addition to very high conductivity PEDOT was found to be almost transparent in thin oxidized state. The solubility problem was subsequently solved by using a water soluble polyelectrolyte polystyrene sulfonic acid as charge balancing dopant during polymerization to yield PEDOT:PSS. This combination resulted in a water soluble polyelectrolyte system with good film forming properties, high conductivity high visible light transmittivity and excellent stability. There are different methods to synthesize PEDOT. Oxidative chemical polymerization of the ethylene dioxy thiophene (EDT) based monomers, electrochemical polymerization of the EDT based monomers and transition metal mediated coupling of dihaloderivatives of EDT. The PEDOT:PSS used here was made using the third method and was developed by Bayer AG. This method utilizes the polymerization of EDT in an aqueous polyelectrolyte (most commonly PSS) solution using $Na_2S_2O_8$ as the oxidizing agent. Carrying this reaction out at room temperature results in a dark blue aqueous PEDOT:PSS dispersion which is commercially available from Bayer AG under the trade name Baytron P. An interesting aspect of Baytron P is that after drying the remaining PEDOT:PSS film

is highly conducting transparent mechanically durable and insoluble in any common solvent [77].

3.1. 6 bR

bR is a biological photochrome with exceptional properties, produced by Halobacterium Salinarium. bR is found to be the functional component of so called "purple membranes (PM)" and has a two dimensional, crystalline lattice [175] in conjunction with a lipid bilayer structure. bR has been reported to be the only protein found in PM. PM used was obtained from MIB Germany and has been prepared from the Halobacterium Salinarium strain S-9 cells according to the method of Oesterhelt and Stoeckenius [86, 87] and was highly purified by density gradient centrifugation and contains more than 99.9% of bR (referring to proteins). bR was individually tested by absorption spectroscopy, SDS-page analysis and a number of other tests. Aqueous suspensions of pure PM has a ratio of absorption coefficients OD_{280} /OD_{570} of equal or better than 2.5. The bR embedded in PM is obtained in lyophilized form. Lyophilized PM can easily be re-suspended in water and can be sonicated to achieve the desired homogeneity. Aqueous suspensions of purple membranes can be stored for a short time at a temperature of +4°C and can be stored at -20°C without any time limitation.

3. 2 Film Fabrication Procedures

3. 2. 1 Single layer structures

The single layer structures of conjugated polymers were made by dissolving the polymer in appropriate solvents and then spin casting the solution on clean ITO plates. The solvents used are chloroform and p-Xylene (sulfur free) for P3OT, P3HT, MEHPPV, PVK. BBL is dissolved in a Lewis acid to form a Lewis acid complex. The BBL was recovered by decomplexing the film by washing with methanol and distilled water for eight hours respectively. PEDOT:PSS was obtained as a dispersion in water and was used as it is. Aluminum (Al) or gold (Au) was used as the cathode and was thermally evaporated in a vacuum chamber ($< 10^{-6}$ Torr) to have 5 mm^2 area of the sandwich type structure. The thickness of

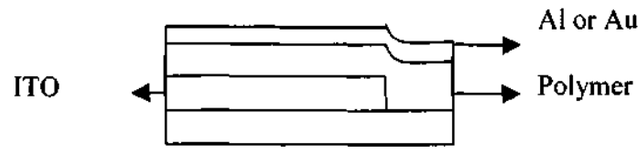

Fig. 3. 2 *Schematic of the single layer structure.*

the single layer varied from 50 nm to 200 nm and is controlled by the solution concentration and rotation speed. The solution concentration here was 1 mg/ml and rotation speed varied from 1000 rpm to 3000 rpm. A schematic of the single layer structure is shown in Fig. 3. 2.

3. 2. 2 Polymer-polymer bilayer fabrication

The bilayers were prepared so as to study the properties of a heterojunction consisting of a p-type polymer and n-type polymer similar to a p-n heterojunction made from inorganic materials. The p-type polymers were coated first on well cleaned ITO (patterned) coated glass plates using spin coating and thoroughly dried by keeping it in vacuum oven for 30 minutes at 50 ^{0}C. The substrate coated with p-type polymer was then transferred to a glove box filled with inert argon gas. The n-type polymer BBL was spin coated, dried and washed first with methanol and then with distilled water for 8 hours each. Then the samples were transferred to a vacuum oven and heated to 60 ^{0}C for two hours. The metals were deposited on top of BBL using thermal evaporation techniques with a device area of 5 mm^2 to have a sandwich structure. The integrity of the bottom layer was checked with absorption spectra. The interlayer diffusion related problems did not arise in these bilayers as BBL was not soluble in common organic solvents and the p-type polymers did not dissolve in the Lewis acids. A schematic diagram of the bilayer structure is as shown in Fig. 3. 3.

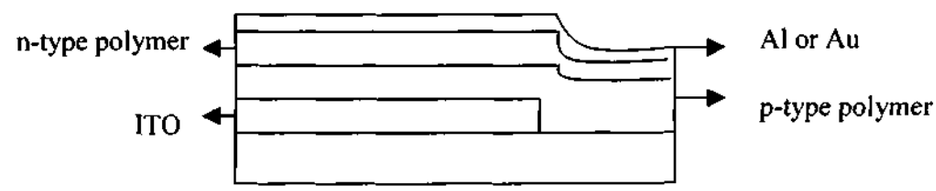

Fig. 3. 3 *The schematic diagram of a bilayer structure.*

It was also seen that the BBL complex with $AlCl_3$ in nitrobenzene, which wets the P3OT surfaces, did not wet the surface of MEHPPV. But BBL complex with $GaCl_3$ in nitromethane wet the MEHPPV surface and was used to make the MEHPPV based bilayer. Cross section scanning electron microscopy (SEM) indicated distinct boundary at the interface of two layers. Samples of different thickness were made. The sample thickness of individual p-type polymer layer vary from 50 nm to 200 nm and that of n-type polymer layer vary from 100 nm to 50 nm. The thickness was optimized for maximum photocurrent efficiency.

3. 2. 3 Polymer – inorganic nanocrystallites bilayer

The polymers were coated on ITO as in the case of a single layer structure. The nanocrystallites dissolved in dimethyl formaldehyde (DMF) were spin coated on top of the polymer. The solubility of the polymer in DMF is very low, thereby decreasing the possibility of diffusion of nanocrystallites into the polymer layer in a short spinning time. In order to improve the hole injection properties a thin layer of PVK is introduced in between the polymer and ITO. The metals were deposited on top of CdS nanocrystallites to have 5 mm^2 area structures. A schematic diagram of such kind of bilayer structure is as shown in Fig. 3. 4.

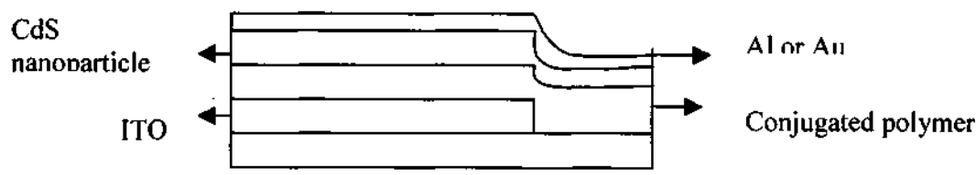

Fig. 3. 4 *Schematic of conjugated polymer/nanoparticle bilayer structure.*

3. 2. 4 Polymer – biomolecule bilayer

The polymer PEDOT:PSS was spin coated on top of a well cleaned ITO substrate and heated to 120 ^{0}C. While cleaning, a silane solution, Hexamethylsilazane (HMDS) was used to remove the oily layer on top of ITO. The biomolecule, bR in PM was dispersed in distilled and deionized water to make a 10mg/ml concentrated dispersed solution. The bR dispersion (30 μl) was placed in between the 1 mm spacing of PEDOT:PSS and Au coated glass plate and a

small electric field (300 V/cm) is applied with ITO positively biased. The solution was allowed to dry while the bias is ON. Before casting, the dispersion was ultrasonicated for 3 minutes to get a homogeneously dispersed solution. The electric field and PSS helps to orient the bR containing PM with its positively charged extracellular side facing the PEDOT:PSS. The availability of negatively charged PEDOT:PSS surface can be attributed to the 3:1 weight ratio of PSS to PEDOT and weak electric field. Schematic of the bilayer structure and the electric field application is as shown in Fig. 3. 5.

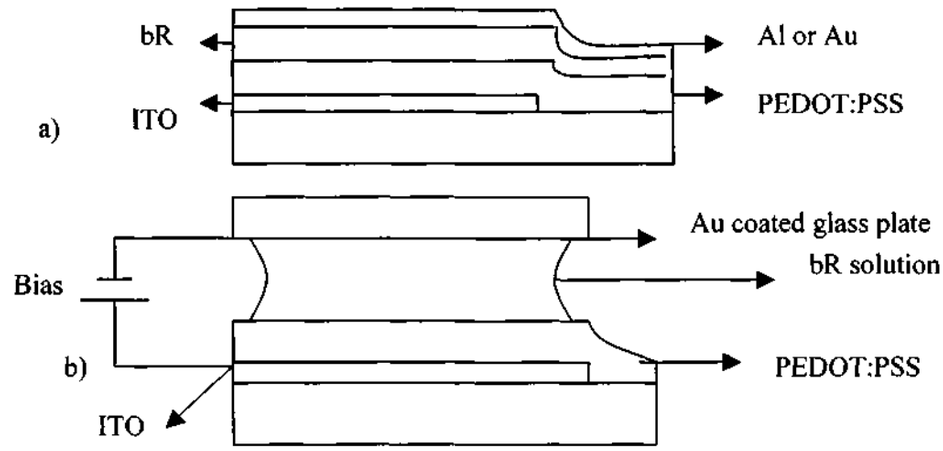

Fig. 3. 5 *a) The schematic diagram of PEDOT:PSS/bR bilayer structure, b) schematic of the electric field assisted orientation of bR on PEDOT:PSS.*

3. 3 Methods

3. 3. 1 Determination of absorption coefficient

The single layer and bilayer structures of similar thickness was made on thin quartz plates as it was on an ITO plate and were used for absorption measurements. The measurements were done using Hitachi U-3400 spectrophotometer and Perkin Elmer spectrophotometer. The absorbance spectrum of the polymers in solution was also taken in order to compare with that of the thin films. The absorption coefficient can be determined from the absorbance spectrum using the equation 3.1 taking into account the interfacial reflection, where α is the

$$\alpha d = 2.303 \log\left(\frac{I_0}{I}\right) \tag{3.1}$$

absorption coefficient, d thickness of the film, I_0 the incident beam intensity and I the transmitted beam intensity.

3. 3. 2.Photocurrent spectroscopy

The photocurrent spectral responses were measured using lock in technique. In this technique the samples were illuminated with a chopped light and the photocurrent was measured using a lock in amplifier (SRS SR830DSP) locked at that chopping frequency. The chopper frequency varied from 10 Hz to 1.2 kHz. The integration time constant of the lockin amplifier varied according to the chopping frequency selected. The monochromatic light source used was a tungsten lamp or Xenon lamp coupled with a monochromator (Acton Spectrapro150 or Spex 500M). The photocurrent spectral response is given by

$$I_{ph}(\lambda) = AI(\lambda)\alpha(\lambda)\eta(\lambda) \qquad (3.2)$$

where A is a constant, I(λ) is the incident intensity, α(λ) is the absorption coefficient and η(λ) is photocarrier generation efficiency at a particular λ. The correction for the spectral response of the lamp and monochromator was done by taking the spectral response of a standard silicon photodiode placed at the same position as that of the sample without changing any other external parameters and dividing this from the experimental photocurrent spectrum. The schematic of the set up was as shown in Fig. 3. 6.

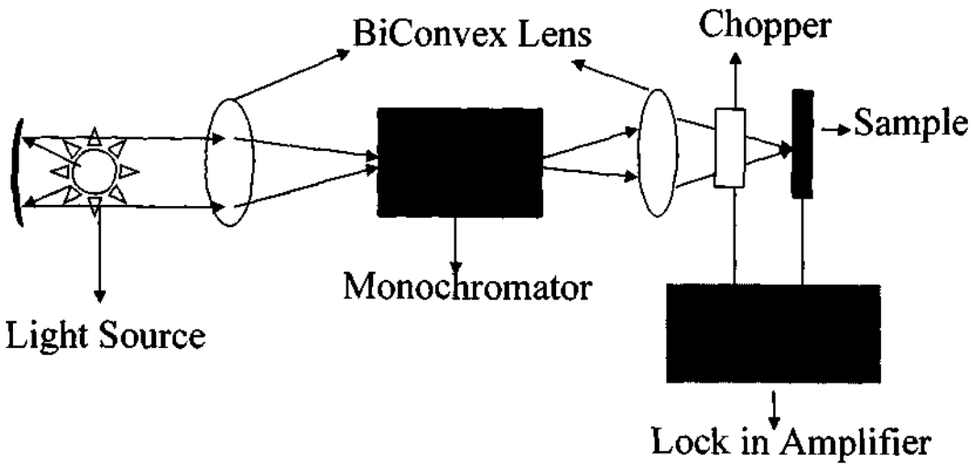

Fig. 3. 6 *Schematic of the experimental set up for photocurrent spectral response.*

3. 3. 3 Current Voltage characteristics

The transport properties of the bilayers were studied using current voltage characteristic (IV). Different models were used for analyzing the IV characteristic. The IV characteristic of the device was measured using a source meter (Keithley 2400) and an electrometer (Keithley 6512). The data was taken with enough time gap in order to avoid the hysterisis related artifacts. The positive bias to ITO was considered as forward bias and negative bias to ITO was considered as reverse bias with respect to Al or Au. The pin hole effect was reduced by reducing the active area of the bilayer structure. In the case of IV in presence of a monochromatic light, the current was measured using lock in amplifier for a modulated incident light and using electrometer for continuous illumination. A schematic representation of IV set up is as shown in Fig. 3. 7.

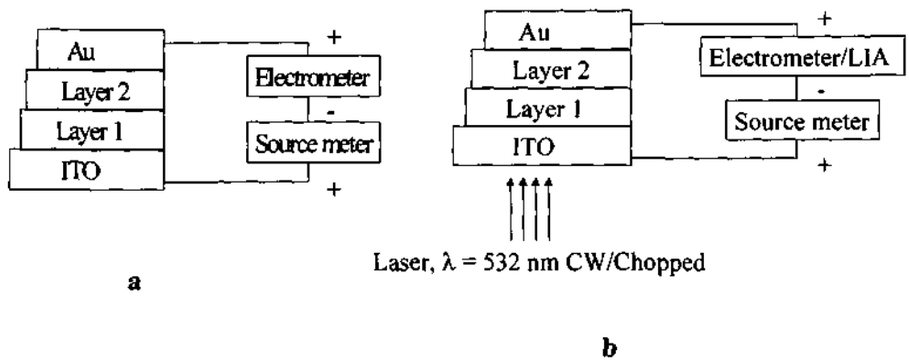

Fig. 3. 7 *Schematic of IV set up for **a)** dark and **b)** in presence of light.*

3. 3. 4 Transient photocurrent measurement

The transport properties of the semiconductors were studied by time of flight techniques. In the time of flight technique, a pulse of free charge carriers was created at one electrode of the sandwich device and was allowed to flow to the other electrode under an external electric field. Here, a short pulse of light created the charge carriers. The decay time constants of the transient signal were used to estimate the mobility of free charge carriers in semiconductors. These measurements were good for materials whose dielectric relaxation time constant (τ_σ) is greater than the transit time ($t_{transit}$) of free charge carriers in the device made of the same material. If this condition was not satisfied, the estimated mobility can

be wrong at low electric fields. τ_σ is defined as $\varepsilon\varepsilon_0/\sigma$, where ε = the dielectric constant of the material and ε_0 = the dielectric constant of free space and σ = the conductivity of the material. $t_{transit}$ is defined as $d/\mu E$, where d = the interelectrode distance of the sandwich device, μ = the mobility of the free charge carriers in the material and E = the external electric field. Here our aim was not to determine the mobility but to study the transport of photogenerated free carriers at the interface for short and long light exposures. A 10 ns pulsed laser (λ = 532 nm) of power 5 mW was used as short pulse source. Diode lasers (λ = 405 nm, 472 nm) of power 5 mW and light emitting diodes (λ = 472 nm, 532 nm, 570 nm, 660 nm) of power ≈ 1 mW modulated by a function generator (HP, Tektronix) were used as long pulse source. The I_{ph} was measured using oscilloscope, electrometer and multimeter. In order to understand the dynamics of free charge carriers,.the transient photocurrent measurements were done for different temperatures and electric field for the bilayer structures. A schematic representation of the transient photocurrent measurement set up is as shown in Fig. 3. 8.

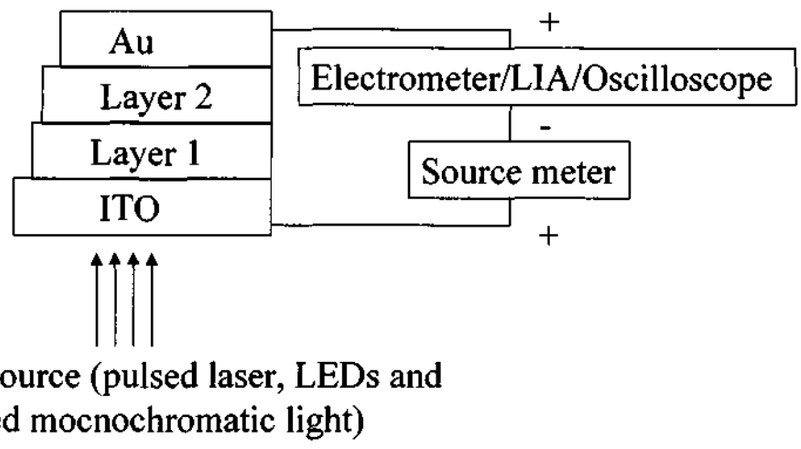

Fig. 3. 8. *Schematic of the transient photocurrent measurement set up.*

3. 3. 5 Intensity modulated photocurrent spectroscopy

Intensity modulated photocurrent spectroscopy (IMPS) was used as an impedance related technique in which the light intensity, that was incident on a sample, was modulated sinusoidally [194]. As a consequence the photocurrent that

flows through the sample shows a harmonic response that can be shifted in phase and magnitude. The IMPS signal has a real and imaginary part and was measured using a lock in amplifier , and was plotted in the complex plane. This nonstationary technique can give us an understanding of the kinetics and mechanisms of elementary photoinduced process at the interface by fitting it to a model and has been used extensively in the case of semiconductor/electrolyte interfaces. LED's (λ = 660 nm, 470 nm, 532 nm) modulated with a function generator were used as the light source and the photocurrent was measured using lock in amplifier in the short circuit mode. These measurements were also carried at different temperatures.

3. 3. 6 Thermally stimulated current

The devices consisting of polymer materials are prone to have defects, which was found to be due to chemical impurities. Thermally stimulated current (TSC) study has been used to probe such defect states, which limits the electro-optical properties of the device [195]. In this technique the sample is kept at a constant temperature and perturbed with photoexcitation or applying a large electric field in order to populate the localized electron traps or hole traps within the band gap of the material. After removal of the external perturbation the system was left in a non equilibrium state which relaxes towards thermal equilibrium via a rate limiting step of thermal release of carriers from the traps into the bands. The interpretation of the results is based on fitting the experimental results to expression from models for the kinetic processes. A typical TSC has been carried out and the steps involved were as follows. The sample was heated initially to $\approx$ 350 K maintained for 45 minutes and voltage or current source or light was applied to sweep the residual trap charges or fill the traps (time of field polarization, $t_p \approx$ 30 minutes). The samples were subsequently cooled to 10 K in the presence of this voltage bias. The short circuit current was then measured as a function of temperature (10 K- 400 K) at a typical linear heating rate (β) of 2.5 K/minute.

3. 3. 7 Capacitance Voltage measurements

The capacitance due to a depleted region of a p-n junction was measured using this technique. This measurement was done in the present case of p-type polymer/n-type polymer bilayer assuming that it is analogous to an inorganic p-n

junction. The measurements were done using a capacitance voltage meter and HP impedance analyzer. The capacitance was measured at different bias voltages and frequencies. The measurements were also carried out in presence of light using LED's. The measurements were carried out assuming that the electrode polymer contact is ohmic. Bilayer devices show capacitive nature. The capacitance can be due to the free carriers stored in traps. This also gave a measure of the depletion width created at the interface between a metal and polymer or polymer/polymer. The measurements were done using Keithley C-V meter and HP impedance meter. The capacitance C of a heterojunction is

$$C = \left[\frac{qN_p N_n \varepsilon_p \varepsilon_n}{2(\varepsilon_n N_n + \varepsilon_p N_p)(V_{bi} - V)} \right]^{1/2} \qquad (3.3)$$

where q is the charge of electron, N_p is the number of acceptor impurity, N_n is the number of donor impurity, ε_p and ε_n are the dielectric constant of p-type and n-type materials respectively, V_{bi} is the built in potential at the interface and V is the applied bias.

Chapter 4

Conjugated polymer-conjugated polymer bilayer structure

Conjugated polymer/conjugated polymer bilayer structure were made by using p-type conjugated polymers and n-type conjugated polymers, similar to the p-n heterojunction in inorganic semiconductors. These bilayers have been investigated for the photoinduced interfacial processes involved at the interface. The processes include free charge carrier creation, carrier transport, trapping of the carriers at defect sites and transfer of free charge carriers at the interface. These processes were found to be important to understand the limiting factors of photovoltaic properties based on these structures.

4. 1 p-type polymer/n-type polymer interface

The interface of a p-type polymer/n-type polymer can be thought to be similar to the p-n heterojunction in inorganic semiconductors. The schematic of the energy level diagram of the two layer before contact is as shown in Fig. 4. 1a. The assumption is that the contact between the two layers results in a narrow depleted region created because of the space charge due to shallow level traps (Fig. 4. 1b). This results in a band bending due to energy level rearrangement in order to match the fermi levels (Fig. 4. 1c). The energy level gets modified upon reverse biasing (Fig. 4. 1d) and forward biasing (Fig. 4. 1e). In the reverse bias mode, the energy barrier at the interface is favorable for high exciton dissociation and transfer of holes and electrons to the electrodes, which results in higher photocurrent efficiency. In the forward bias condition, the energy levels get modified in such a way that the exciton dissociation is less and the barrier is not favorable for hole and electron transfer and hence results in less photocurrent.

The energy level gradient created at the interface results in an electric field at the interface (Fig. 4. 1f). The electric field at the interface plays an important role in the enhanced photovoltaic properties of the bilayer structure. The interface was also expected to show an asymmetric current voltage characteristic similar to

the p-n heterojunction in inorganic semiconductors provided the metal/polymer interface has an ohmic contact.

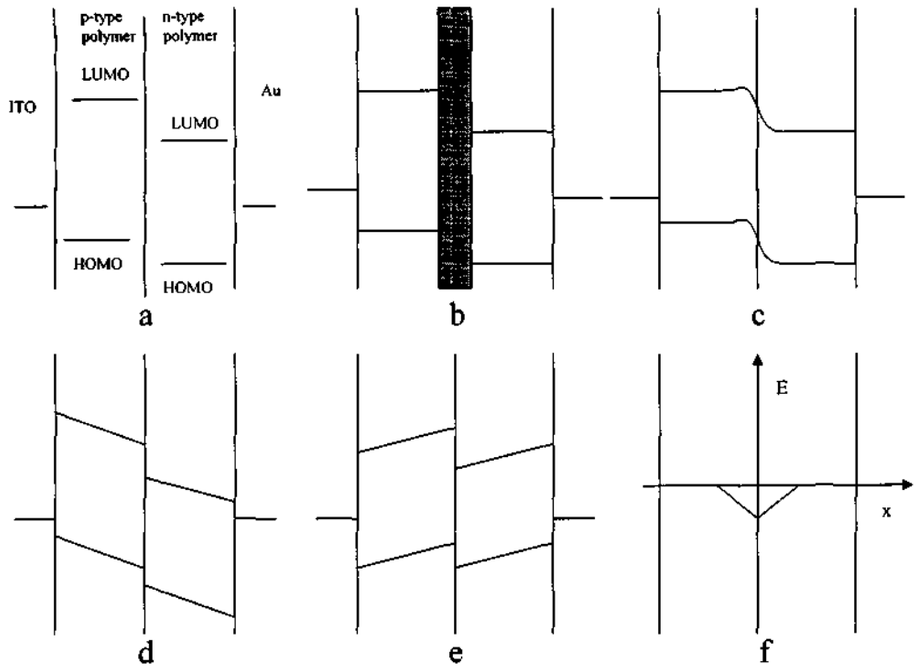

Fig. 4. 1. *Schematic of a) the energy level diagram of the bilayer structure before contact, b) assumed depleted region(shaded) when the two layer is in contact with each other, c) The energy level modification at the interface of the bilayer structure, d) modified energy level diagram of the bilayer structure in reverse bias mode, e) modified energy level diagram of bilayer structure in forward bias mode and f) the electric field at the interface of the bilayer structure.*

4. 2 Current – voltage (IV) characteristics

The IV characteristic of the bilayer (P3OT/BBL) showed an asymmetric behavior similar to the p-n heterojunction (Fig. 4. 2). The deviation from an ideal p-n heterojunction behavior can be attributed to the pinhole and impurities present in the sample. The transport properties of P3OT/BBL bilayer was studied by fitting the IV characteristic to the space charge limited transport due to traps [196, 197] (Fig. 4. 2 inset) in the injection mode(forward bias).

$$J = \frac{9\varepsilon\varepsilon_0\mu V^{2+x}}{8L^3} \qquad (4.1)$$

where V is the applied voltage, μ is mobility of the carrier, ε is the dielectric constant of the material, L is the thickness of the sample. The current varies as $V^{2.8}$ and the transport is limited by the space charge due to traps at the interface.

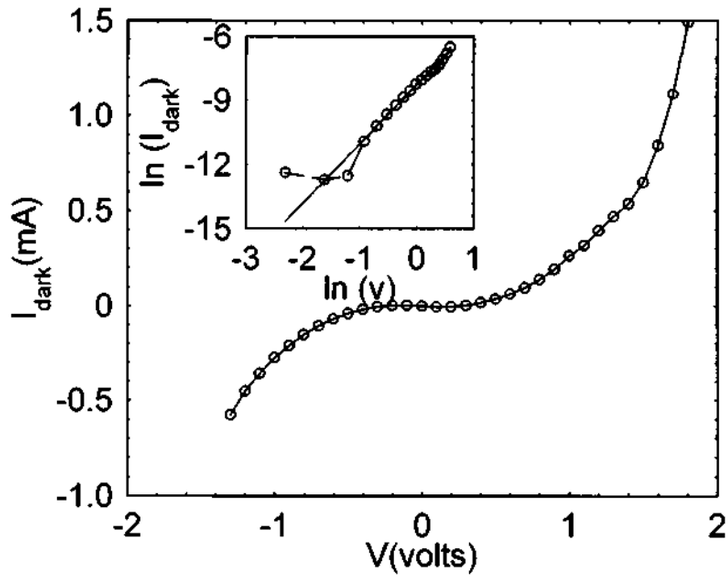

Fig. 4. 2 *The dark I-V characteristic of ITO/P3OT/BBL/Au bilayer structure. Inset shows the fit to the dark I-V in the forward bias mode.*

This validates the assumption that a space charge was created at the interface due to shallow level traps as the polymer came into contact. The metal/polymer interface showed a ohmic IV behavior. The space charge at the interface results in a depleted region at the interface and has been probed by capacitance voltage measurements.

4. 3 Capacitance voltage measurements

The capacitance voltage measurements (Fig. 4. 3) showed a capacitance of 9 nF which can be attributed to a depleted zone at the interface of width 20 nm [198]. The capacitance measured at higher forward bias showed an accumulation of charges at the interface. The reverse bias showed an increase in the depletion width. The measurement confirms the assumption of a space charge region at the

interface due to traps. This space charge region plays a decisive role in the photoinduced processes at the interface. The space charge induced electric field at the interface enhances the exciton dissociation at the interface. The electric field will get modified due to the minority carrier traps in the respective individual layers.

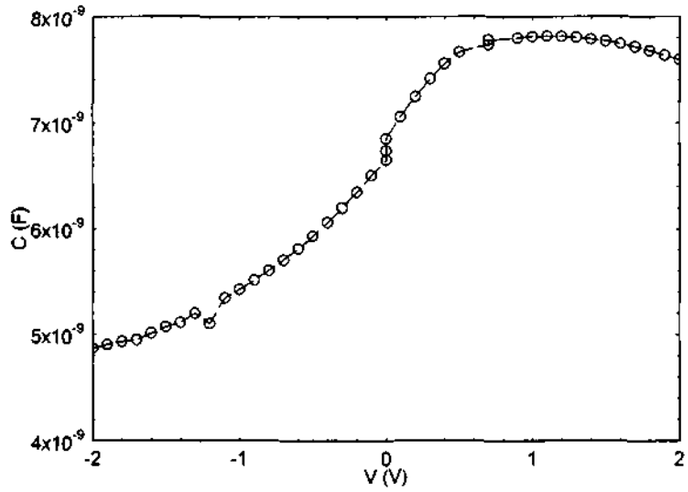

Fig. 4. 3 *The capacitance voltage characteristic of the ITO/P3OT/BBL/Au bilayer structure.*

4. 4 Photocurrent spectroscopy

The photoinduced free charge carrier generation was found to be a secondary process involving different steps as shown in Fig. 4. 4 [50]. The bilayer consists of two polymers, which absorb in different region of the solar spectrum. P3OT and MEHPPV have an absorption window for $\lambda \leq 650$ nm and BBL has an absorption window for $\lambda \leq 750$ nm. The photocurrent spectral response ($I_{ph}(\lambda)$) of both P3OT/BBL and MEHPPV/BBL bilayer initiates at $\lambda \approx 750$ nm, which is the absorption edge of the BBL and shows the absorption features of individual layers as shown in Fig. 4. 5. and Fig. 4. 6 respectively. The bilayer clearly showed an increase in the $I_{ph}(\lambda)$ compared to single layer devices of same thickness. The experiments were carried out with different thickness and the thickness was optimized (p-type ≈100 nm, n-type ≈ 60 nm) for higher photocurrent (I_{ph}) efficiency. P3OT/BBL bilayer showed two orders of increase in I_{ph} while

MEHPPV/BBL showed four orders of increase in I_{ph} compared to that of a single layer structure

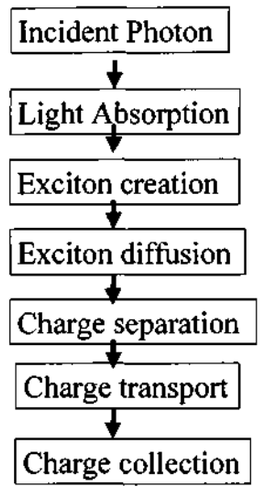

Fig. 4. 4 *The block diagram of charge carrier generation process in a conjugated polymer based photovoltaic device.*

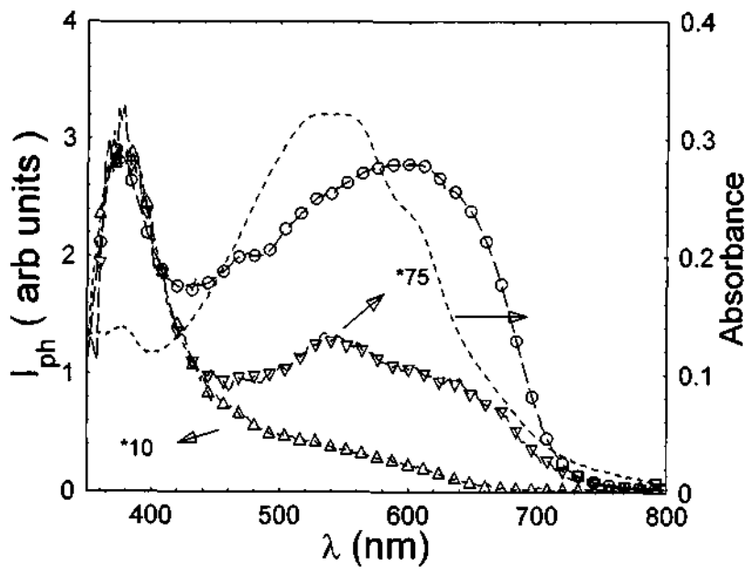

Fig. 4. 5 *The normalized $I_{ph}(\lambda)$ of ITO/BBL/Au (∇)(scaled 75 times), ITO/P3OT/Au (Δ)(scaled 10 times), ITO/P3OT/BBL/Au (o) and absorption spectra (dashed line) of bilayer structure of similar thickness coated on quartz plate.*

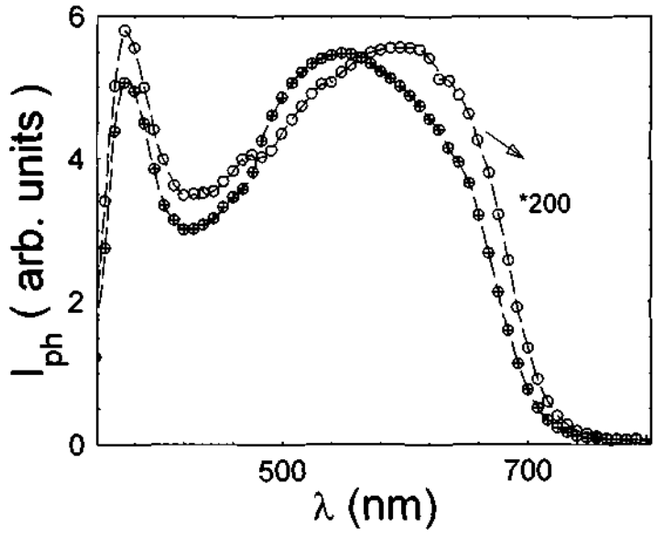

Fig. 4. 6 *The normalized $I_{ph}(\lambda)$ of ITO/P3OT/BBL/Au (o)(scaled 200 times) and ITO/MEHPPV/BBL/Au (⊕) bilayer structure.*

The $I_{ph}(\lambda)$ of the bilayer can be explained as follows: In the wavelength range 650 nm $< \lambda <$ 750 nm, the I_{ph} can be attributed to the photocarrier generation in BBL layer, where the absorption contribution of P3OT or MEHPPV were found to be negligible. The photogeneration of free carriers in BBL can be attributed to the defect and trap induced exciton dissociation. But the efficiency of a single layer BBL was found to be low due to the reduced transfer rate of hole to the electrodes or in other words the hole transfer was limited by the higher density of hole traps. The increase in I_{ph} of the bilayer compared to single layer BBL can be due to the enhanced hole transfer to the electrode through a hole transporting material. This was a result of the interfacial electric field due to the space charge at the interface of the bilayer, which enhances the transfer of holes in BBL near to the bilayer interface to the hole mobile P3OT or MEHPPV. The $I_{ph}(\lambda)$ increased significantly for 700 nm $> \lambda >$ 600 nm and peaks at $\lambda \approx$ 650 nm. This can be attributed to the higher exciton dissociation at the interface due to band edge absorption of P3OT. The $I_{ph}(\lambda)$ gradually decreased for 500 nm $< \lambda <$ 600 nm and can be due to the higher absorption of P3OT compared to BBL which results in an exciton creation away from the interfacial electric field region. But it was

observed that the I_{ph} showed a higher efficiency compared to a single layer in this λ range.

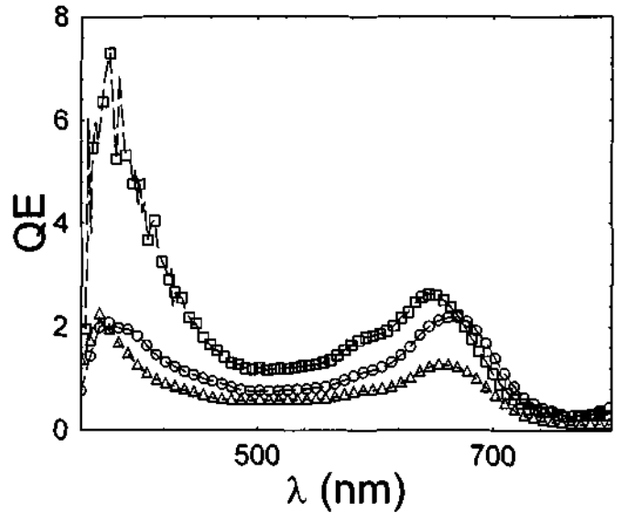

Fig. 4. 7 *The relative quantum efficiency (QE) (scaled 10 times) of ITO/P3OT/BBL/Au bilayer structure with light incidence through ITO (Δ), Au (o) and that for a reverse bias of –1.5 V (□) with light through ITO.*

The observation leads to the assumption that the depletion width at the interface increased due to the incident light. The assumption is validated by the short circuit photocurrent, which has a reverse bias current direction and the increase in I_{ph} for λ, where the penetration depth defined as 1/absorption coefficient $\alpha(\lambda)$ was less than the thickness of the P3OT layer. The enhancement in I_{ph} (λ) for 500 nm < λ < 700 nm can be attributed to the interfacial active region due to space charges.

The confirmation of interface as the photoactive region was done by $I_{ph}(\lambda)$ measurements for light incident through both the electrodes and electric field dependence. The relative quantum efficiency spectral envelope of the bilayer for light incident from ITO side and Au side was similar with a ≈ 20 % increase in the I_{ph} (λ) with light through Au side (Fig. 4. 7). The increase in efficiency for light through Au can be attributed to the additional diffusive component of the holes towards the bilayer interface. It has to be observed that if the active regions

were metal/polymer interface, it should result in a symbatic and antibatic $I_{ph}(\lambda)$, as light incident through ITO or Au respectively(Symbatic: $I_{ph}(\lambda)$ has full width at half maximum of ≈ 50 nm about the absorption edge the polymer, Antibatic: $I_{ph}(\lambda)$ initiate at the absorption edge of the polymer and spreads over the entire absorption range). The electric field increases the I_{ph} (λ) efficiency in the reverse bias mode and reduces in the forward bias mode (Fig. 4. 8).

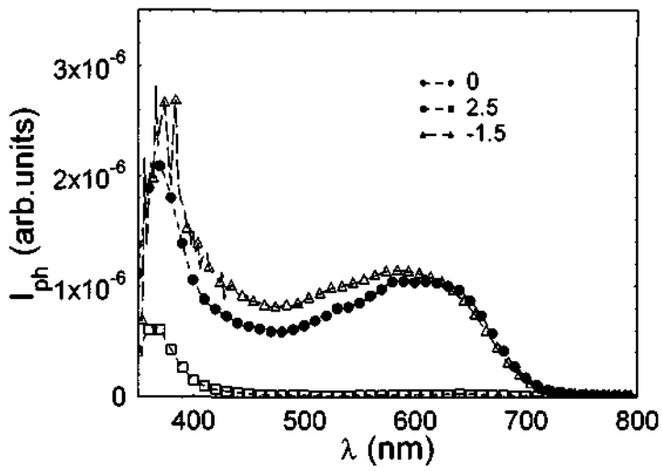

Fig. 4. 8 *The normalized $I_{ph}(\lambda)$ of ITO/P3OT/BBL/Au bilayer structure under different bias conditions.*

This clearly showed the rectification behavior of the interface. The increase in I_{ph} can be attributed to the efficient sweeping of photogenerated free carriers to the electrodes. $I_{ph}(\lambda)$ spectral shape was independent of the electric field strength and can be attributed to the invariant photoactive region at the bilayer interface. It was also observed that irrespective of the individual layer thickness, the $I_{ph}(\lambda)$ spectral shape was similar with variation in the I_{ph} efficiencies confirming the interface of the bilayer as the photoactive region.

Another clear observation was that, I_{ph} direction in a single layer ITO/BBL/Au sample with BBL layer thickness similar to that of BBL in P3OT/BBL bilayer. In the single layer, the I_{ph} indicates electron transfer from BBL to ITO electrode and hole transfer to Au electrode. In the bilayer, the I_{ph} direction indicates that the electron from BBL layer transfer to Au and hole from P3OT

transfer to ITO. This observation can be unambiguously explained only by invoking the more efficient bilayer interfacial minority carrier charge transfer process. This universality of the decisive interfacial factor was also observed in the complementary structure ITO/BBL/P3OT/Au where the direction of short circuit I_{ph} reverses under the same external electrical configuration. The $I_{ph}(\lambda)$ was unchanged and the external quantum efficiency marginally drops due to the mildly blocking nature of the electrodes. This observation unequivocally proves the origin of enhancement in $I_{ph}(\lambda)$ is due to bilayer interface.

The figures of merits of the bilayer for photovoltaic application were calculated and are as follows. The photoresponsivity (S) defined as the ratio of the short circuit I_{ph} (A/cm^2) to the incident power (W/cm^2) and was found to be 60 mA/W for P3OT/BBL bilayer and 0.2 A/W for the MEHPPV/BBL bilayer. The incident photon to current conversion efficiency (IPCE %) defined as (1240 S(A/W)/λ(nm))×100 % was 14% for P3OT/BBL bilayer and 48% for MEHPPV/BBL bilayer at λ = 532 nm. The open circuit voltage (V_{oc}) of ≈ 0.9 V was measured using a modulated monochromatic incident light source

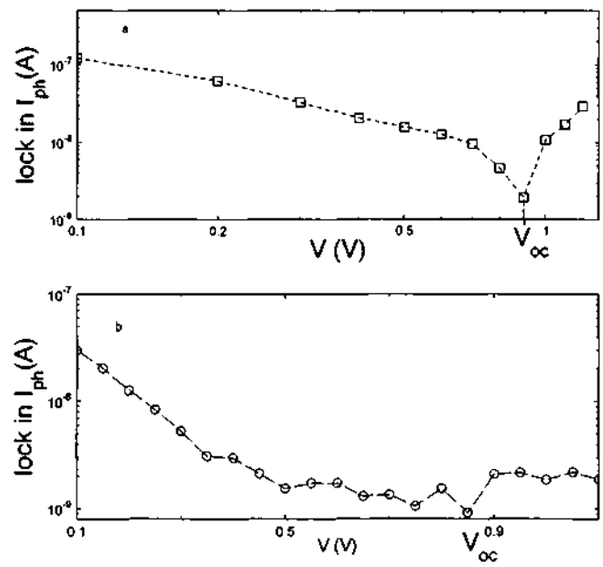

Fig. 4. 9 *The modulated photocurrent (modulated at 19 Hz, λ = 532 nm) I_{ph} Vs V for (a) ITO/P3OT/BBL/Au and (b) ITO/MEHPPV/BBL/Au bilayer structures.*

at λ = 532 nm of intensity 1 mW/cm^2 (Fig. 4. 9). The V_{oc} was similar to the fermi level difference of the two polymers used in the bilayer, which further validates the

argument of photoactive region as the bilayer interface [199, 200]. The fill factor (FF) of the bilayer structure is defined as the $(IV)_{max}/I_{sc}V_{oc}$ and the power conversion efficiency PCE is defined as the $(FF)I_{sc}V_{oc}$/ incident light power. The FF calculated was 10% and PCE was 1.5% for the MEHPPV bilayer structure. The FF and PCE values were lower by an order of magnitude for P3OT/BBL bilayer.

The interesting observation of lower I_{ph} efficiency of P3OT/BBL bilayer compared to MEHPPV/BBL bilayer, even though both of them has similar HOMO and LUMO energy levels can be attributed to other factors. These factors are linked to transfer and transport of the photogenerated free carriers, which affect the external quantum efficiency of the bilayer device.

4. 5 Transient photocurrent measurements

The transient I_{ph} was done using a 10 ns pulsed laser at λ = 532 nm of power 1 mW/cm^2 (Fig. 4. 10). The measurements were for $t_{transit} < \tau_\sigma$ in order to avoid the electric field redistribution effects. The I_{ph} transient showed a stretched exponential decay, $I(t) = I_0\exp(-(t/\tau)^\gamma)$ which has been a feature of transport limited by the traps [201] (Fig. 4. 10 inset). The fit gave the exponent value $\gamma \approx 0.64$ and decay time

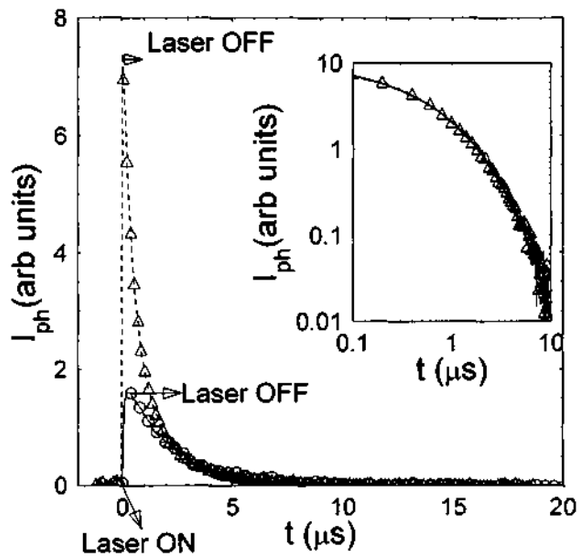

Fig. 4. 10 *Transient $I_{ph}(\lambda)$ of ITO/P3OT/BBL/Au (Δ) and ITO/MEHPPV/BBL/Au (o) bilayer structures using λ = 532 nm, 5 ns pulsed laser. Inset shows the fit to a stretched exponential model.*

constant of the I_{ph} transient τ as $\approx$ 0.56 ms. The gain calculated as the ratio of the number of photogenerated free charge carriers to the number of photons was 33% for P3OT/BBL and 18% for MEHPPV/BBL of similar thickness. The traps were inevitable as the bilayer structure has high density of traps for one of the free charge carriers in individual layer.

4. 6 Persistent photocurrent measurements

Persistent $I_{ph}(t)$ were studied to understand the effect of traps and interfacial process for long exposure of light. The bilayer structure of MEHPPV/BBL showed a totally different $I_{ph}(t)$ response compared to that of P3OT/BBL bilayer. The P3OT/BBL bilayer I_{ph} showed an initial increase and gradual decrease while light was ON. The I_{ph} decreased and reversed its direction while light was OFF and gradually relaxes to the dark value (Fig. 4.11). The experiments were carried out for different duration of exposure time varying from 10 ns to 2 s and it was found

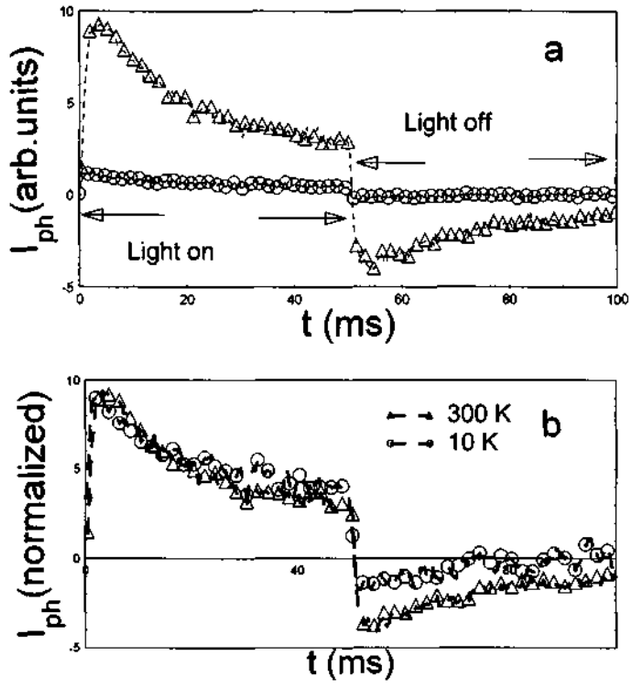

Fig. 4. 11 *a) Transient $I_{ph}(\lambda)$ of ITO/P3OT/BBL/Au bilayer structure for a LED (λ = 660 nm) pulsed at 10 Hz at 300 K (Δ) and at 10 K (o) and b) shows the normalized data.*

that there was a threshold exposure time (light ON > 2 ms) for this type of charging phenomena to initiate. The decay time-constant τ_{on} during the ON-period is ≈ 38 ms. Upon switching OFF the light, after long exposure duration, the I_{ph} decreases and changes its direction (polarity) and then eventually relaxes to the original dark conditions with τ_{off} ≈ 30 ms. These observations indicate the additional capacitive component upon photoexcitation. Upon decreasing the temperature to 10 K, t_{ON} increases marginally and was accompanied by a faster decay response, τ_{on} ≈ 30 ms. These features, related to photo-initiated charging and discharging, were absent in case MEHPPV/BBL bilayer (Fig. 4. 12) systems and single layer devices of P3OT, BBL and MEHPPV. The long lived I_{ph} transient

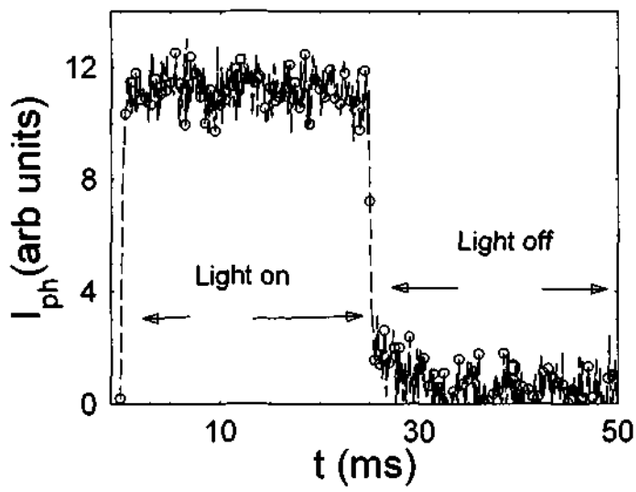

4. 12 *Transient $I_{ph}(\lambda)$ of ITO/MEHPPV/BBL/Au device for a LED (λ = 660 nm) pulsed at 10 Hz at 300 K.*

measurements clearly showed that the P3OT/BBL interface was quite different from that of MEHPPV/BBL interface and focussed our results on P3OT/BBL devices to study the effect of interfacial defect states on charge separation and transport across the layers. The long time response of ITO/P3OT/BBL/Au in short-circuit current mode and in presence of an external bias is shown in Fig. 4. 13. It was observed that the decay rates did not vary significantly with the electric field in the range 0.5 V > V > -2.0 V and was comparable to decay rate of the short-circuit current obtained by short pulses (prior to charging).

Accumulation of such kind of interfacial charges limits the photovoltaic properties of the bilayer structure. This event is caused by the asynchronized rates of charge generation, transport, different dielectric relaxation time constant (τ_σ) of the individual layer and the transfer rate due to the presence of interfacial barrier states, which impede the flow of carriers. The capacitive nature of the photo-induced current generated by long-light pulses can be interpreted in terms of the charging process, which continuously modifies the photo-induced electric field re-distribution and in the process impedes the flow of carriers across the interface.

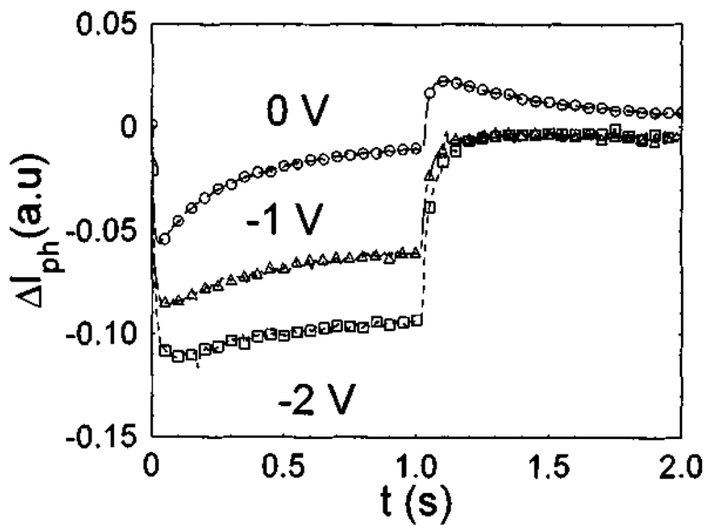

Fig. 4. 13 *The response of ITO/P3OT/BBL/Au for a LED (660 nm) of pulse width 1 s under 0 V(o), -1 V (Δ) and –2 V (□).*

This factor is quite significant in case of P3OT/BBL compared to MEHPPV/BBL. An important observation in our work is that MEHPPV/BBL devices have higher PV efficiency than P3OT/BBL in spite of a higher μ_h of P3OT compared to MEHPPV. Another way to interpret is that the device efficiencies are dependent on the duration incident photon rate (repetition rate). Within the charging limit or short pulse duration (< 1 ms), the current in P3OT/BBL is not impeded by the charging effects but for longer exposure duration the efficiency of MEHPPV/BBL is significantly higher than P3OT/BBL devices. The light-induced decay was completely absent in $I_{ph}(t)$ in MEHPPV/BBL devices for MEHPPPV layer

thickness ranging from 50 nm to 150 nm, while the photo-induced charging was always present in all P3OT/BBL devices (independent of thickness). From this it is obvious that the specific nature of P3OT/BBL interface is a crucial factor for this feature.

P3OT/BBL interface exhibit charging upon prolonged-exposure (duration time > 2 ms) of light of intensity 1 $mWcm^{-2}$. This time constant for charging can be related to the trap filling and emptying kinetics. The spatial region for these trap states were speculated to be located in the P3OT section of the interface based upon studies of samples with different thickness, comparison with single layer devices. The gain, which is defined as the ratio of the number photogenerated free

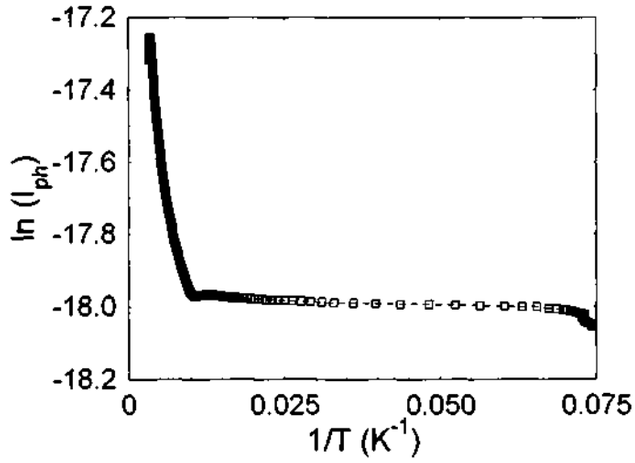

Fig. 4. 14 *The temperature dependence of the modulated $I_{ph}(\lambda)$ (chopper frequency 73 Hz, λ = 532 nm).*

charge carriers to the number of incident photons, calculated is 33% for P3OT/BBL and 18% for MEHPPV/BBL. It is interesting to note that the P3OT/BBL is efficient for short pulse duration (t < 100 ns) compared to MEHPPV/BBL, while for steady sate continuous exposure MEHPPV/BBL devices show higher efficiency. Transient measurement with pulses of different ON duration indicates that there is a threshold value of photogenerated charge, Q ≈ 10^{-9} C (corresponds to a free carrier density of ≈$10^{15}/cm^3$), above which the charging at the interface is observed. For a long light-pulse duration of 10 ms, ≈ 5 μC charges are trapped at the interface.

Temperature dependent measurements of the I_{ph} were also done. The peak value as measured by the oscilloscope (Fig. 4. 11) or the RMS value as measured by the lock in amplifier (LIA) (Fig. 4. 14) showed a reasonably strong dependence of I_{ph}, with I_{ph} decreasing with decreasing temperature. A clear single activation behavior with an activation energy of 0.34 eV (300 K -150 K) range was observed. The activation energy value can be attributed to barrier limited charge carrier transport in bulk since similar value was obtained from the dark conductivity temperature dependence in BBL films of similar thickness [202]. The charging behavior (presumably from the interface) persisted at 10 K also. The time constant of the charging and discharging appeared similar to that at 300 K. A complete picture involving the distribution of the shallow tape levels at the interface is necessary to understand this feature completely.

A clear evidence of the dominant photoactivity and trap center can also be inferred from the experiments with light incident from Au side. I_{ph} time dependent profiles were observed on the oscilloscope upon photoexciting ITO/P3OT/BBL/Au with pulsed LEDs with light incident from the ITO side as well as the Au side. Experiments carried out with light incident through Au side using 670 nm red LED

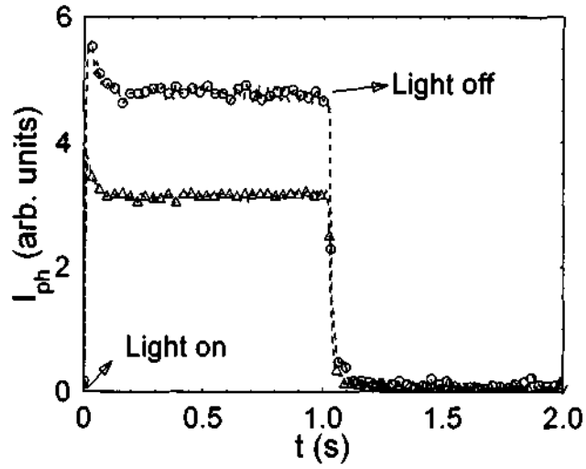

Fig. 4. 15 *I_{ph} per unit photon absorbed of ITO/P3OT/BBL/Au devices using a pulse of 1 s duration of λ = 660 nm LED (o) and of λ = 472 nm LED (Δ) from the Au side.*

(at λ = 670 nm, $\alpha_{BBL} \approx 5000$ cm^{-1}, $\alpha_{P3OT} < 100$ cm^{-1} in this region) resulted in a higher density of charge carriers at the p-n interfacial zone. A higher charge

accumulation or photocapacitance was observed in this case compared to a blue LED source (Fig. 4. 15). This excess charge carrier at the interface also had a characteristic stronger temperature dependence, which can be explained on the basis of the trap states. The sizable decrease in this magnitude of I_{ph} at 10 K also is directly related to trap-barrier levels.

Simultaneous illumination from both the ITO side and Au side, in tandem and with controlled phase difference of the driving voltage pulses to the LED, reveal the difference in the dynamics of the charge carriers originating from the two layers. The critical threshold for charging can be increased by distributing the photogenerated carriers optimally across the interface. However, recombination of the photogenerated charge carriers can be expected to dominate at high intensities. In order to understand the asymmetry involved in the charge carrier creation and transport across the interface, different λ were used to illuminate from both sides.

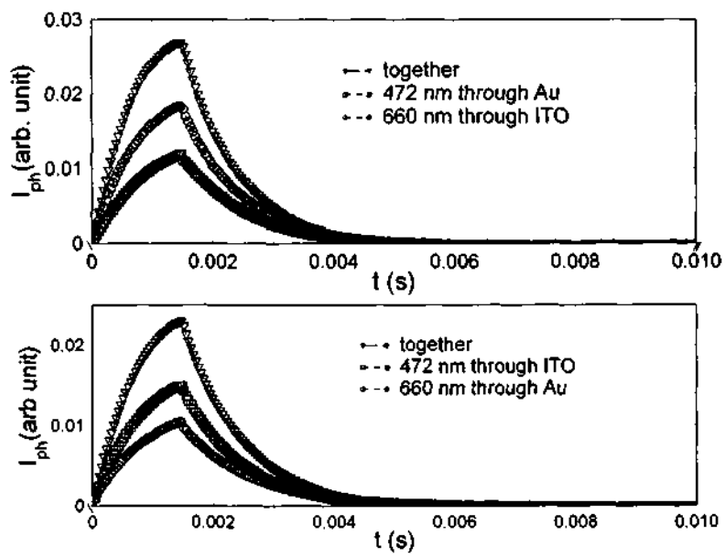

Fig. 4. 16 *The I_{ph} profile for ITO/P3OT/BBL/Au bilayer structure for light incidence through ITO, Au and simultaneously for pulse time duration less than charging time.*

These observations can be summarized as follows: (i) For t_{ON} < 1 ms (Fig. 4. 16), the net I_{ph} is an algebraic sum of the individual components, i.e., I_{ph}(total) = I_{ph}(light incident from ITO side) + I_{ph}(light incident from gold side) at any λ. (ii)

For t_{ON} > 1 ms (Fig. 4. 17), it is observed that the I_{ph} (total) < I_{ph} (light incident from ITO side) + I_{ph}(light incident from gold side), this difference from the algebraic sum gets more accentuated in the spectral region where P3OT is more photoactive.

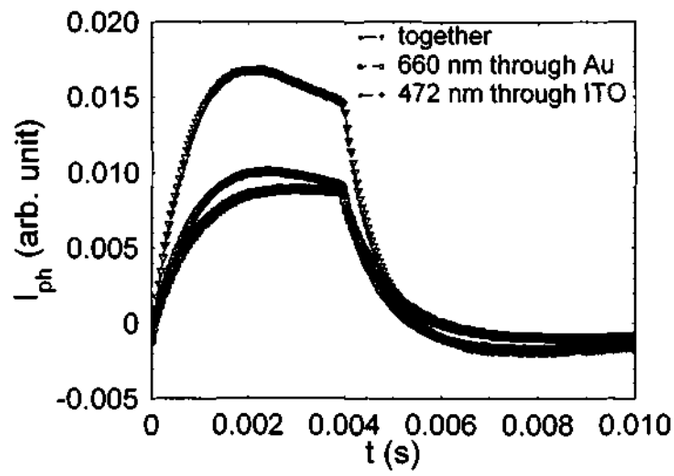

Fig. 4. 17 *The I_{ph} profile for ITO/P3OT/BBL/Au bilayer structure for light incidence through ITO, Au and simultaneously for pulse time duration greater than charging time.*

When P3OT is photoactive the photogenerated free carriers get accumulated in P3OT, which results in a reduction of I_{ph}. This validates the previous speculation of charging in P3OT at the interface upon illumination.

The $I_{ph}(t)$ of the ITO/P3OT/BBL/Au devices can also be attributed to the electric field redistribution due to the differences in electrical conductivities (σ) of P3OT ($\sigma_{P3OT} \approx 10^{-7}$ S/cm) and BBL ($\sigma_{BBL} \approx 10^{-10}$ S/cm) as $\tau_\sigma < t_{transit}$ for P3OT layer at short-circuit condition. But for ITO/MEHPPV/BBL/Au, even though $\tau_\sigma < t_{transit}$, ($\tau_\sigma \approx 30$ μs and transit time, $t_{transit} > 4$ ms) no charging phenomena was observed. If the charging was a result of only the dielectric relaxation, it should have its signature for t > 300 ns onwards. Since there was no clear distinction made between the charging due to dielectric relaxation and that due to trap induced space charge, the charging phenomena can be attributed to both these properties. It is also to be noticed that the threshold period of charging depends on the incident photon rate and the duration. Charging/retarding effects are absent even over long light duration in these ITO/MEHPPV/BBL/Au devices of varying thickness.

4. 7 Intensity dependence

The above observations are also reflected in the intensity dependence studies of P3OT/BBL bilayer structure, where $I_{ph} \propto (\text{Intensity})^{\eta}$[203]. I_{ph} has a sub-linear dependence on the intensity for intensity-modulation frequency of < 1 kHz (for example $\eta = 0.8$ at $\omega = 19$ Hz for intensity range > 0.6 mW/cm^2) (Fig. 4. 18). The η value is 0.9 for the intensity range 0.05 - 1 mW/cm^2 for frequencies > 1 kHz as shown in Fig. 4. 18 inset. The I_{ph} for MEHPPV/BBL bilayer structure, on the other hand, exhibits linear response with intensity of the incident light at both lower and higher frequency range.

The near linear dependency of the I_{ph} at intensity < 0.6 mW show that the free charge carrier transfer across the interface takes place before the accumulation process at the interface. At higher intensity, there is an accumulation of $\approx 10^{13}$ carriers cm^{-2} at the interface and the field due to this oppose further transfer of minority carriers across the interface resulting in a reduction in I_{ph}. The space

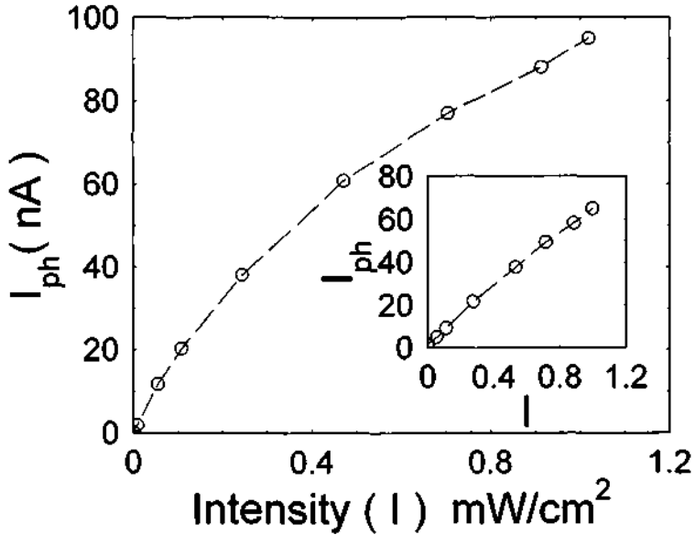

Fig. 4. 18 *The I_{ph} Vs Intensity for ITO/P3OT/BBL/Au bilayer structure at λ = 532 nm. Inset shows the same for a modulated (1.2 kHz) incident light.*

charge related to this accumulation can be attributed to the traps and interfacial states present in the bilayer [203]. The I_{ph} shows a near linear intensity dependency ($\eta = 0.9$) at chopping frequencies above 1.2 kHz. The effect of charging of P3OT at the interface for chopping frequency < 80 Hz, when light incident through both

ITO and Au side validates the deviation from linear behavior at low chopping frequencies and for $\omega = 0$, continuous illumination.

4. 8 Intensity modulated photocurrent spectroscopy

The photo initiated interfacial transport processes were studied by IMPS. IMPS measurements were carried on P3OT/BBL bilayer samples and the real and imaginary components of $I_{ph}(\omega)$ was determined over 10 Hz - 15 kHz range. Imaginary $I_{ph}(\omega)$ vs Real $I_{ph}(\omega)$ at 300 K and 10 K is shown in Fig. 4. 19.

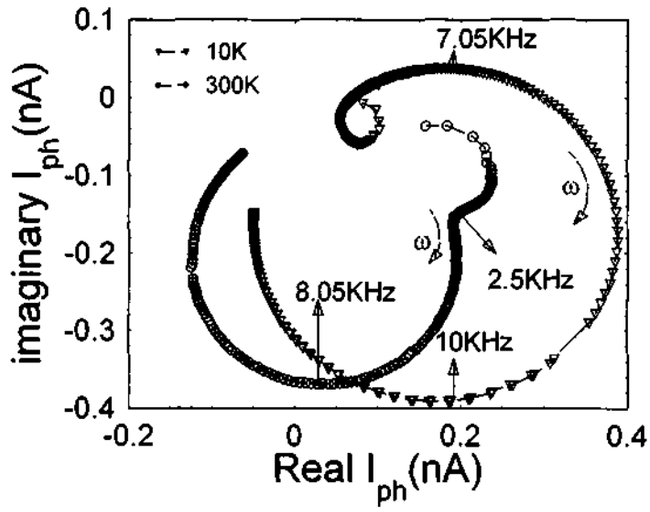

Fig. 4. 19 *The intensity modulated photocurrent spectra of ITO/P3OT/BBL/Au bilayer structure using a modulated LED source at λ = 660 nm in 10 Hz to 15 kHz frequency range at temperature 300 K and 10 K.*

The plot of imaginary I_{ph} vs real I_{ph} consists of two arcs with two ω_{min}, (ω_1, ω_2) at 300 K. The low frequency component in the fourth quadrant shifts to first quadrant at 10 K. The arc-length increases by a factor of two when the temperature is varied from 300 K to 10 K.

The IMPS response can be modeled using kinetic equations of minority carrier traps and releases as shown in Fig 4. 20.

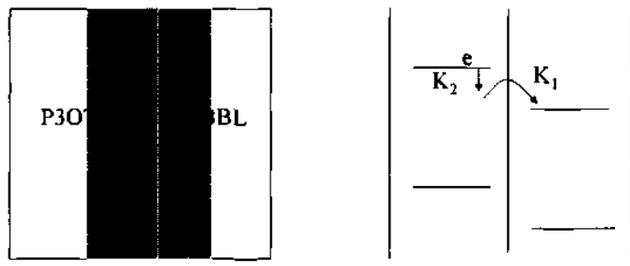

Fig. 4. 20 *Schematic of the interfacial process at the P3OT/BBL interface and interfacial capacitance.*

The assumption is that the incident light creates free charge carriers within and near to the interface so that the diffusion of minority carriers from the bulk towards the polymer-polymer interface can be neglected. Illumination of light through ITO creates electron-hole pairs, subsequently, the majority carriers in P3OT move to ITO whereas the minority carriers move to the interface, where they can get trapped at a rate constant K_2 and released from traps at a rate constant K_1. This trapping and detrapping can result in an effective charging at P3OT and BBL layers near the interface. At low incident intensity, linear conditions can be assumed. The appropriate differential equations for the photogenerated charge Q_1 across C_1 of P3OT capacitive layer and for the photogenerated charge Q_2 across C_2 of BBL capacitive layer near to the interface then are

$$\frac{dQ_1}{dt} = I_0(1+\exp(i\omega t)) - J - K_2(Q_1 - Q_2) \qquad (4.2)$$

$$\frac{dQ_2}{dt} = K_1(Q_1 - Q_2) - J \qquad (4.3)$$

Assuming a constant potential across the system

$$\frac{Q_1}{C_1} + \frac{Q_2}{C_2} = JR \qquad (4.4)$$

where I_0 is the amplitude of modulated photo current, and J is the external current due to photogenerated carriers Fig. 4. 21.

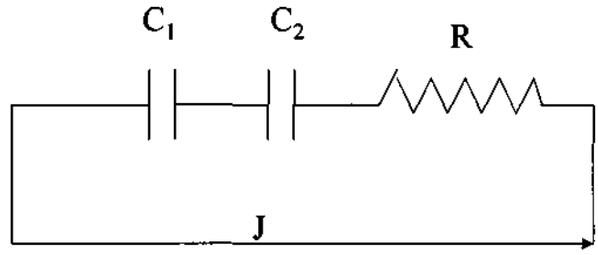

Fig. 4. 21 *Schematic of the circuit diagram used in solving the equation.*

Solving this three equations

$$J = I_0\left[\frac{K_1 + i\omega\dfrac{C}{C_1}}{(K_1 + K_2 + i\omega)(1 + i\omega\tau)}\exp(i\omega t) + \frac{K_1}{K_1 + K_2}\right] \tag{4.5}$$

And the ac component is given by

$$J(\omega) = I_0\frac{K_1 + i\omega\dfrac{C}{C_1}}{(K_1 + K_2 + i\omega)(1 + i\omega\tau)} \tag{4.6}$$

where $C = C_1C_2/(C_1+C_2)$, $\tau = RC$. The two ω_{min} ω_1 and ω_2 arise due to the different rate of K_1 and K_2 respectively. The increase in ω_1 can be correlated to the decrease in the value of trapping rate K_1 at 10 K. ω_2 does not change significantly at 10 K. The trapping rate and hence the capacitance depends on the density of photogenerated free charge carriers. The model fits in the low frequency range (10 Hz -5 kHz) with an estimate of $K_1 \approx 50$ ms , $K_2 \approx 50$ ms and $C \approx 100$ nF. Direct capacitance measurements with light ON of the same device at 100 Hz also show a photocapacitance of $\approx$ 100 nF.

4. 9 Thermally stimulated current measurement

Another useful probe to study the defect states is by measuring the TSC. This technique conceptually involves perturbing the system with photoexcitation, or applying a large electric field in order to populate the localized electron traps or hole traps within the band gap of the material. After removal of the external perturbation the system is left in a non-equilibrium state, which relaxes towards

thermal equilibrium via a rate-limiting step of thermal release of carriers from the traps into the bands. The interpretation of the results is based on fitting the experimental results to expression from models for the kinetic processes. TSC has been recently used to evaluate the trap density and trap depth in the pristine and heat-treated BBL and P3OT films [195]. TSC results of BBL films indicated existence of variety of trap states, which depend on the morphology and thermal history. Various defect characteristics with an estimate of trap states ranging from 0.5 eV to 20 meV were determined in BBL. The additional features, which appear in the TSC glow curve of bilayer structure, and which are absent in the single layer device, is a direct evidence of presence of inter-layer, interfacial states.

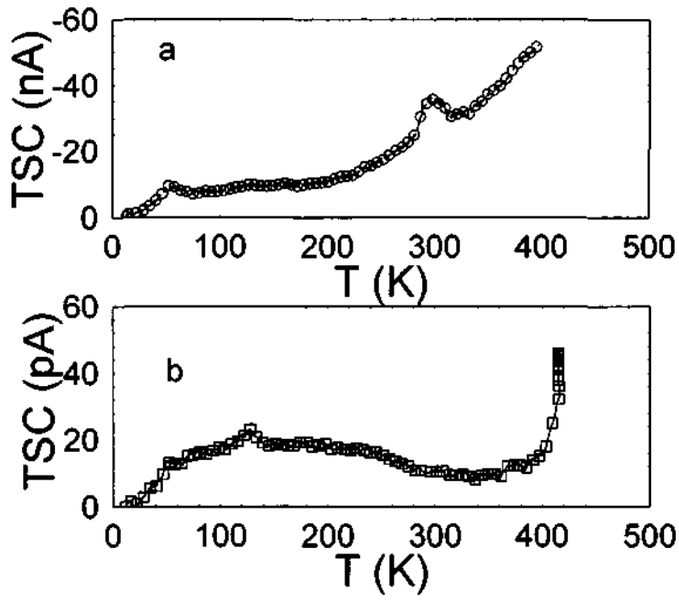

Fig. 4. 22 *TSC of a) ITO/P3OT/BBL/Au and b) ITO/MEHPPV/BBL/Au bilayer structures*

The interfacial charging, in the bilayer P3OT/BBL system, due to trap is substantiated by TSC results and is as shown in Fig. 4. 22a. I_{TSC} (T) as shown in this figure consists of two prominent peaks positioned at $T_{max} \approx 52$ K and 298 K. From the initial rise method [195], the trap depths corresponding to T_{max} are ranging from few meV to ≈ 0.26 eV respectively. The total number of released charges during this experiment is ≈ 7.15 μC and that for MEHPPV/BBL is ≈ 0.1 n

C. The results also indicate the differences in the trap distribution and energy levels between P3OT/BBL and MEHPPV/BBL devices.

Even though the TSC measurements do not give spatial information of the trap distribution, in the present context it serves as a valuable tool to correlate the device performance to defect characteristics. The barrier energy levels corresponding to the prominent peaks are 20 meV and 0.28 eV. The magnitude of TSC and the total thermally releasable charge (a measure of trap density) is nearly three orders of magnitude higher in P3OT/BBL compared to MEHPPV/BBL(Fig. 4. 22b). TSC studies of these bilayers show additional TSC peaks, which were not present in the single layer structures. These peaks can be due to the release of charges from traps present at the interface. The traps at the interface can be attributed to surface and energy level modification when two polymers come in contact. It is noted that the magnitude of trap density derived from the number of releasable traps from TSC is similar to the interfacial trap density estimates from the photo-induced experiments.

4. 10 Summary

The I_{ph} measurements show that the photoactive region in P3OT/BBL and MEHHPV/BBL is at the interface and the Table 4. 1 summarizes the properties of the two bilayers structures.

Device	S	FF	IPCE	PCE	Charging
P3OT/BBL	60 mA/W	1%	14%	0.1%	Severe
MEHPPV/BBL	0.2 A/W	10%	48%	1.5%	Not significant

Table 4. 1 *A comparison of the properties of the two bilayer structure.*

The present approach of time-domain and frequency-domain I_{ph} measurement along with TSC studies emphasize the role of interfacial disorder in these bilayer structures apart from the effects caused by the electric field redistribution. The comparison of MEHPPV/BBL and P3OT/BBL stresses the importance of chemical compatibility of the organic components apart from the constituent properties. The interfacial charging in P3OT/BBL is due to accumulation of photogenerated free

charge carriers in P3OT when it is photoactive. The understanding of these interfacial defects and dielectric relaxation, which limits the performance, is a key factor in the development of polymer based solar cells.

Chapter 5

Conjugated polymer–bR hybrid structures

The photoelectric properties of structures based on unoriented single layer thin solid films of bacteriorhodopsin (bR), and bilayers consisting of a conducting polymer and bR are discussed in this chapter. These structures are studied in terms of its spectroscopic and charge-displacement properties. The spectral response is examined in terms of contributions from its two intermediate states; (i) The primary excited protonated state (yellow) and (ii) the de-protonated M-state (blue). The M state present in the bR photocycle was observed by an additional optical pump (570 nm) during the photocurrent spectral response measurements. The spectrum under these conditions can be understood in terms of kinetics of a 3-level system. The states were characterized by photoelectric spectral responses in the range 300 nm to 700 nm with M-state level features appearing at 420 nm and the B-state at 570 nm.

This chapter then demonstrates the synergistic action arising from the individual effects of a bilayer consisting of a doped conjugated polymer and a protein in the bilayer structure. Results from the measurements carried out for the bilayer structures consisting of the conducting polymer blend and bR reveal the presence of M-state in absence of the optical pump (but in presence of an electrical-pump). In the bilayer structures, the outcome of the photoelectric-spectroscopy measurement is dependent on the external bias voltage. Spectral measurements were carried out systematically as a function of the externally applied bias voltage. The photoelectric spectral responsivity ($R(\lambda)$) of the bilayer and origin of the photoelectric responses were studied and was compared with $R(\lambda)$ of single layer bR.

5. 1 Single layer bR

5. 1. 1 Transient photoelectric response for a longer light pulse

The signal transduction process (optically induced charge-dislocation processes resulting in displacement current) in bR was observed by transient (pulsed light) measurements. The transient photoelectric response (I_{tr}) of the

unoriented single layer bR (Fig. 5. 1) structure was measured using electrometer and a monochromatic light at λ = 570 nm (using Tungsten lamp of power 200 W coupled with Acton Spectra pro 150 Monochromator). The pulse duration was 100 s (using manually operated shutter) and the response was as shown in Fig.5.1. The measurements were carried out under ambient conditions (300 K, 50 % humidity). The I_{tr} increased to a maximum and then decreased to a steady value while the light was ON. The I_{tr} decreased to a minimum with opposite polarity and then decreased to the dark value while light was OFF. The basic mechanism of photoelectric response of bR is photoinduced proton release of Schiff base to extracellular side and uptake from cytoplasmic side through proton pathways. Here the initial increase was attributed to a sudden influx of proton release to the ITO/bR interface, which creates a proton gradient at the ITO/bR interface. This charged interface prevents further flow of protons and results in a decrease in I_{tr} and finally reaches a steady value. The steady value can be attributed to leaky currents due to diffusive, ionic components. Upon switching the light OFF, the bR thermally relax back to the dark condition by reprotonation of the Schiff base and a I_{tr} response, which was similar to charging and discharging of a capacitor was obtained. The I_{tr} response is attributed to proton gradient at the ITO/bR interface upon light exposure.

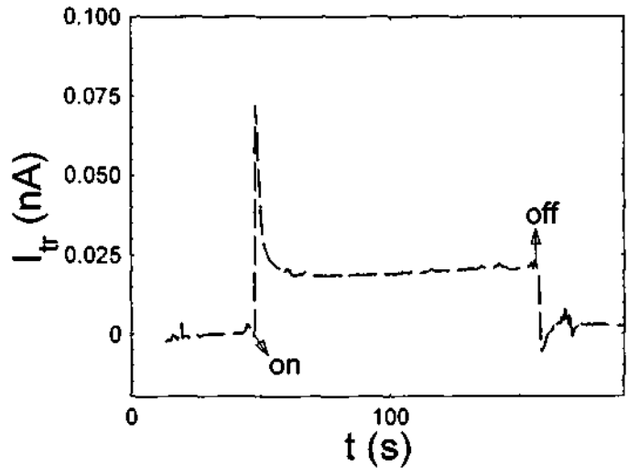

Fig. 5. 1 *The transient photoelectric response of a ITO/bR/Al single layer structure measured using electrometer and a monochromatic light of λ = 570 nm.*

5. 1. 2 Photoelectric spectral response

The R(λ) of a single layer bR sandwiched between ITO and Al was studied using lock in technique, which is a frequency domain measurement technique. This can be compared to the real time measurement by taking Fourier transform of measured signal in real time and is as shown in Fig. 5. 2. The photoelectric signals were measured in the frequency range (< 1 kHz), which correspond to the Fourier transform of the real time measurement of photoelectric responses of bR single layer structure.

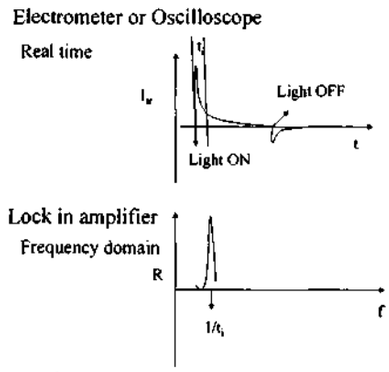

Fig. 5. 2 *Comparison of real time measurements with that of lock in measurements in the frequency domain using lock in technique.*

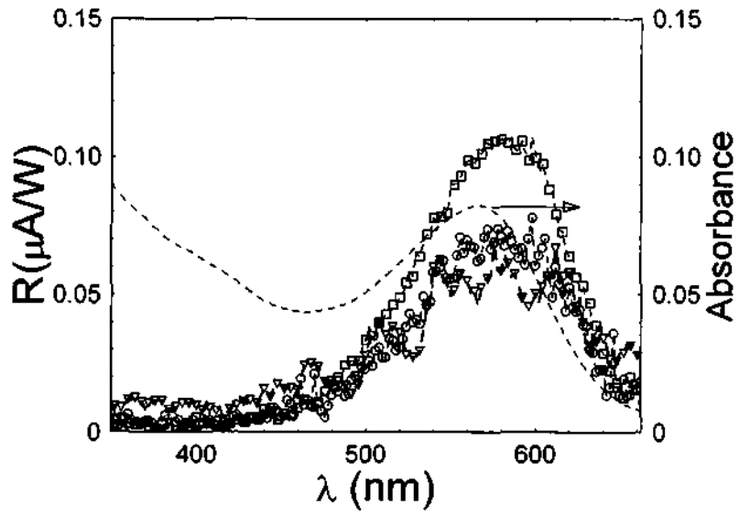

Fig. 5. 3 *The photoelectric spectral response plotted as responsivity R of ITO/bR/Al single layer structure with no bias (o), +12 V to ITO (▽) and −12 V to ITO(□) measured using lock in technique. The dashed line shows the absorption spectra of the bR of similar thickness casted on a quartz plate.*

Sufficient interval was given between two consecutive wavelength readings to avoid history effects in R(λ). The measurements were done with light incident from both ITO and Al sides. Al electrode thickness was < 50 nm and about 30 % transparent.

The R(λ) measured at chopping frequency of 19 Hz, revealed a broad single maximum at around λ = 570 nm as shown in Fig. 5. 3. The R(λ) is similar to the absorption spectra of a cast bR single layer film of similar thickness and primarily depicts the ground state of light adapted bR. In terms of spectral range of operation for such a device, the spectral window covers the range 500 nm < λ < 650 nm. The photoelectric signal at a molecular level can be interpreted to originate from the light induced proton gradient at the ITO/bR interface. The photoexcitation causes the deprotonation of Schiff base in bR followed by a thermal relaxation of deprotonated Schiff base to protonated state by reprotonation of bR from cytoplasmic side. The R(λ) depends on the number of bR molecules in each state in the bR photocycle. The R(λ) can be fitted to a two state model; protonated ground state B and deprotonated metastable state M, and is discussed in the next section. The bias dependent R(λ) showed a marginal increase in the photoelectric response in the reverse bias substantiating the argument that the photoelectric response is due to proton gradient at the ITO/bR interface. Upon biasing the device, a marginal rectification was observed with R(-12 V) ÷ R(12 V) ≈ 2 at λ = 570 nm. This feature, observed in oriented bR-device can be explained largely on the basis of the vectorial nature of photo-induced proton transport. The experiments carried out with light incident from the Al side also showed similar photoelectric spectral responses.

5. 1. 3 Photoelectrical response in presence of continuous optical pumping

The spectral nature of the light initiated current is correlated to the bR photocycle. This aspect is more evident in R(λ) measurements in presence of an additional pump source (CW or a high repetition-rate 10 KHz pump with λ centered about the B state absorption λ_{max} ± 60 nm ~ 570 nm). A clear transfer of the spectral weight from the B-state to the M-state is observed with the appearance

of the M-state contribution centered at $\lambda \approx 412$ nm and a simultaneous decrease of the B-state at $\lambda = 570$ nm. A laser at $\lambda = 532$ nm of power 2 mW/cm^2 was used as the pump source and focused on the same area as the probe area. Spectral measurements of the bR film were recorded in presence of continuous pumping. R(λ) was measured using the lockin technique with probe beam chopped at 19 Hz and is shown in Fig. 5. 4. R(λ) profile consists of the broad peak at $\lambda = 570$ nm accompanied by an additional feature with a maximum at $\lambda \approx 412$ nm. This additional component at 412 nm of R(λ) in the pump-probe experiment can be attributed to the M state in the bR-photocylce. The increase in R(λ) in the range 500 nm < λ < 380 nm was accompanied by a decrease in spectral weight at 500 nm < λ < 650 nm range and can be attributed to the conversion of bR ground state molecules to M state.

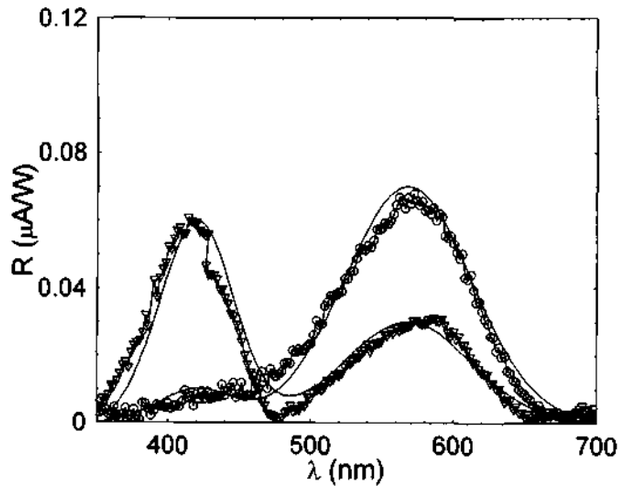

Fig. 5. 4 *The photoelectric spectral response of ITO/bR/Al single layer structure without pumping(o) and in presence of an additional CW pump source, 2 mW/cm^2 at $\lambda = 532$ nm (▽). Solid lines are fit based on kinetic model of two level systems.*

The $I_{ph}(\lambda)$ of the single layer bR can then be explained in terms of superposition of the discrete states and the spectral weight distribution depends on the density distribution of these two states. The intensity-modulated (< 1 kHz) steady state photocurrent spectral response can be modeled by assuming contributions only from these two states [204]. The internal conversion process

efficiency of the molecule in B* (excited B state) to M depends on the pump intensity and can be written as

$$N_M(I) = N_M(0) + (N_B(0) - N_B(0)\exp -(bI)^{\beta}) \quad (5.1)$$

where $N_M(I)$ is the population of M state at a particular pump of intensity, I, $N_M(0)$ is the population of M state before pumping, $N_B(0)$ is the population of B state before pumping, b and β are the constants. The strength of the M state signal depends on the pumping efficiency from B state to M state. The model for the net R with these assumptions can be written in the form

$$R = \sum_i A_i \int \lambda P(\lambda)\alpha_i(\lambda)d\lambda \quad (5.2)$$

where i represents the system state i.e., i = 1 ⇒ B state and i = 2 ⇒ M state. The constant A_i depends on the efficiency of the internal B to M state conversion upon

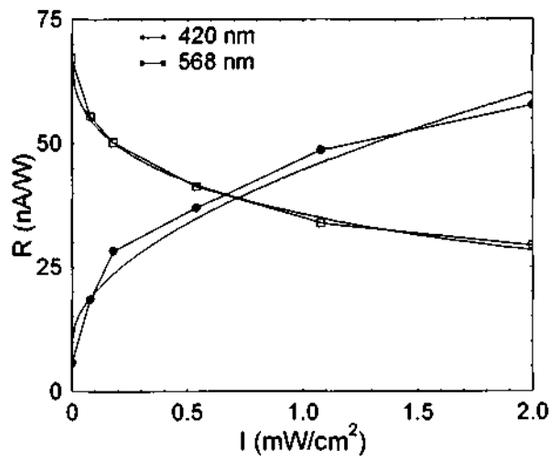

Fig. 5. 5 *Profile of B state and M state of bR in a ITO/bR/Al single layer structure with CW pumping.*

pumping, P(λ) is the spectral power distribution of incident light, α(λ) is the absorptance and can be expressed as $(1 - 10^{A(\lambda)})$ where A(λ) is the absorbance..

At a particular intensity, the ratio of the increase in area enclosed by the R(λ) at about λ = 420 nm to the decrease in area of the R(λ) at about λ = 568 nm gives the efficiency of conversion from B state to M state and is ≈ 64% for a pumping light of λ = 532 nm and intensity ~ 2 mW/cm^2. Fig. 5. 4 reveals the experimental R(λ) with and without the light-pump along with a fit to the model

based on equation 5. 2. The decrease of B state and the increase of M state contributions with pump intensity can be fitted to a stretched exponential $R(B, I) = R(B, 0) \exp(-bI)^{\beta}$ and $R(M, I) = R(M, 0) + (R(B,0) - R(B, I))$ as the $R(\lambda)$ due to any state is proportional to the number of molecules present at that state. The results were depicted in Fig.5. 5 and this indicates the complimentarity in the relative population changes of the two states. These results, which form a measure of the proton displacement were a direct evidence of the correlation between the proton displacement and the associated structural changes in bR.

The I_{tr} of the bR single layer structure at λ = 405 nm of intensity =1 mW/cm^2, in presence of continuous pumping at λ = 532 nm was as shown in Fig. 5. 6.

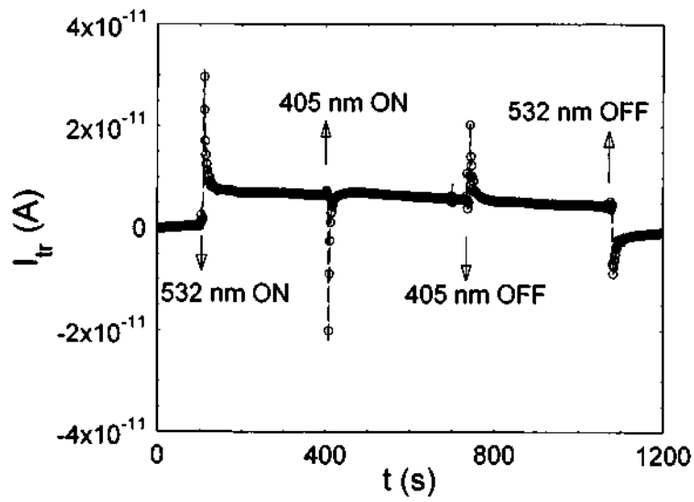

Fig. 5. 6 *The time dependant profile of photoelectric response of ITO/bR/Al single layer structure at λ = 405 nm in presence of CW λ = 532 nm measured using an electrometer.*

The I_{tr} showed a reversal in the polarity at λ = 405 nm compared to that of at λ = 532 nm. The I_{tr} polarity reversal was a controversial issue and has been attributed to the reprotonation of bR from extracellular side. This arguments was contrary to the expected uni-directional, vectorial nature of proton dislocation in bR and is not completely understood.

5. 2 PEDOT:PSS/bR bilayer structure

5. 2. 1 Transient photoelectric response for a longer light pulse

The I_{tr} is shown in Fig. 5. 7 and. shows similar response compared to single layer of bR of similar thickness with an increase in I_{tr} amplitude. The direction and increase in I_{tr} can be interpreted to arise from an oriented bR structure, formed with its extracellular side on the PEDOT:PSS layer. The orientation can be attributed to the anionic surfactant nature of the PSS, which is in large proportion compared to PEDOT (PEDOT:PSS = 1:3) in the mixture PEDOT:PSS. This results in a negatively charged surface. The I_{tr} can be attributed to the proton gradient created at the PEDOT:PSS/bR interface due to deprotonation of Schiff base to extracellular side upon illumination and reprotonation of Schiff base while light is OFF.

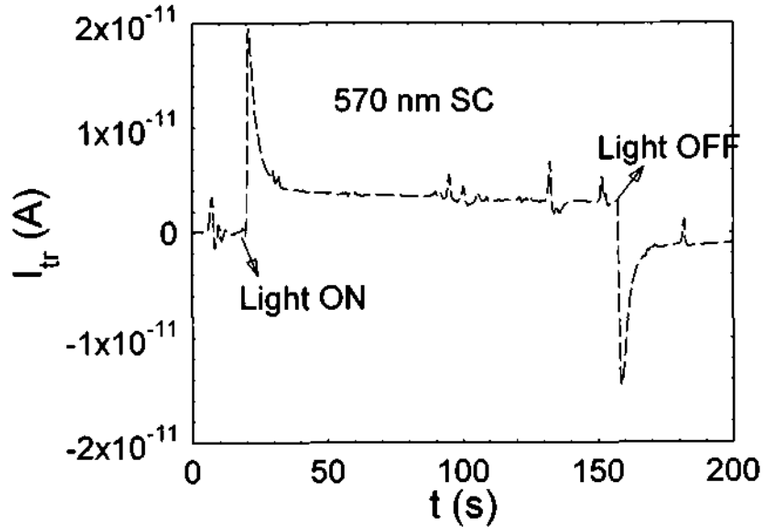

Fig. 5. 7 *Time dependent photoelectric response of the ITO/PEDOT:PSS/bR/Al bilayer structure at λ = 570 nm in short circuit(SC) mode.*

5. 2. 2 Photoelectric spectral response

The R(λ) of the bilayer structure was measured using lock in technique with light chopped at 19 Hz and is as shown in Fig. 5. 8. In the short circuit mode the R(λ) was similar to the bR single layer structure R(λ) with a marginal increase in spectral weight contribution at 380 nm < λ < 500 nm. This can be attributed to the stabilization of M state due to the anionic surfactant at PEDOT:PSS/bR

interface. The magnitude of R(λ) was ten times higher than that of the single layer bR structure of similar thickness and can be directly attributed to the orientation/order of bR on the conducting polymer surface.

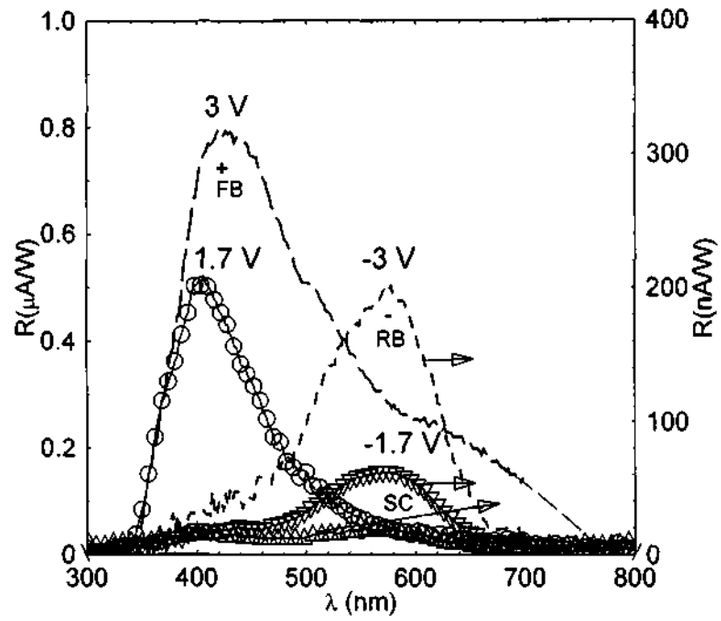

Fig. 5. 8 *Photoelectrical responsivity R(λ) of the ITO/PEDOT:PSS/bR/Al device (ω = 19 Hz). The R(λ) for forward bias (FB), 3 V (long dashed line), 1.7 V(o), for reverse bias (RB) -3.5 V(short dash lines), -1.7 V(∇) and for short circuit (Δ). The R(λ) for reverse bias -3.5 V,-1.7 V and 0 V bias were scaled up by a factor of 2.25 and scaled down by a factor of 5 for 3 V respectively.*

The R(λ) can be explained on the basis of photoinduced proton gradient at the PEDOT:PSS/bR interface due to the deprotonation and reprotonation of Schiff base. Several interesting additional features in the R(λ) characteristics were observed when bR was oriented on PEDOT:PSS. The R(λ) of PEDOT:PSS/bR films at a reverse bias (RB) of -3 V, had a peak value at 570 nm (note that peak location is similar to pristine bR layer). The response was two orders of magnitude more efficient than that of ITO/bR/Al device. This increase in magnitude correlates with the degree of orientation of bR on the anionic surface of the conducting

polymer electrode. The degree of orientation can be controlled by the deposition parameters such as the electric potential of the bottom PEDOT electrode during the formation of the bR layer on the electrode from the water based suspension. The most striking feature was the appearance of a significantly different R(λ) in PEDOT:PSS/bR/ devices under positive bias (FB) conditions. A distinct responses was observed, with an R(λ) at positive bias corresponding to an

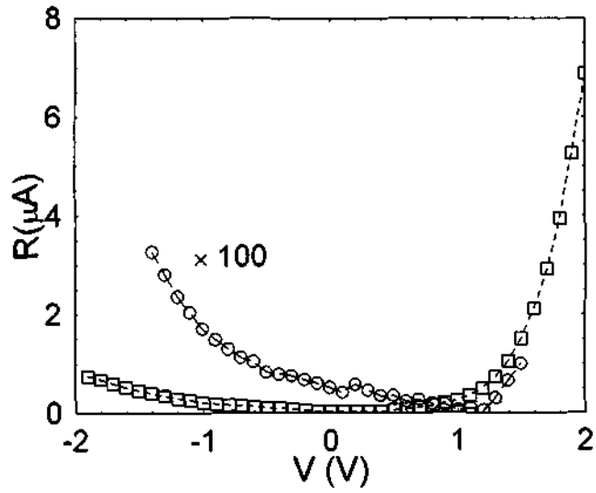

Fig. 5. 9 *Photoelectric spectral response R(λ) – V behavior of the device for λ = 570 nm (O) and at λ = 405 nm (□).*

R(λ) maximum at λ ≈ 420 nm, compared to the negative bias R(λ) which had λ_{max} ≈ 570 nm. The spectrally active region of R(λ) exclusively depends on the polarity with just an increase in magnitude of the peak current accompanied by significant broadening with increasing voltage without any significant variation in λ_{max} corresponding to the peak position. This observation also manifests in the R(λ) - V curve as shown in the Fig. 5. 9 at the two wavelengths and is an extremely interesting feature from a device (color dependent ac photodiode) perspective. The quantitative discrepancy in the magnitude of R(λ) (Fig. 5. 8 and Fig. 5. 9) can be accounted by the history dependence which is described in the sections below.

The distinct blue-shifted R(λ) (*appearing even in the absence of a pump source*) at positive bias voltage then can be interpreted to arise from a separate pathway which stabilizes the deprotonated M-state at the interfacial region. This

was different from earlier reports of electric field effect on bR [205-207]. Upon photoexcitation, the protein channel across the membrane, which serves as the conduit for the proton H^+ transfer to the polymer electrode is not active, due to the electrostatic repulsion from the positive polarized surface. The nature and characteristics of $R(\lambda)$ also changes compared to a typical bR differential response with a sizable presence of a large light-induced dc component in the FB conditions. This feature is indicative of the additional ionic components in the current through the layers apart from the charge displacement component. The relaxation process of the photoinduced charge displacement is caused by an effective translocation of the proton towards the extracellular (conducting polymer) direction and is a dominant factor in the RB case. While in the FB case, a counterion drift away from the electrode seems to be occurring. It is not clear whether this FB photoinduced current can be attributed to a photoreversal of the proton-displacement at 405 nm, which has been observed earlier in certain conditions. The lack of capacitive component points to an ion-pathway surrounding the proton channel. This photo-initiated ionic current can then be expected to ionic current features such as the reversal of the mobile ions upon reversing the applied voltage, which however is not observed in this case due to the inherent asymmetry in the I-V introduced by the PEDOT's electrochemical rectifying behavior.

The effectiveness of the wavelength selective light-valve was clearly observed upon reversal of the forward bias, resulting in a negligible $R(\lambda)$ in the negative bias at λ = 405 nm, while at λ = 570 nm, R(-1.7 V) was significant compared to R(+1.7 V). The bias dependent $R(\lambda)$ at the two spectral regions can also be interpreted in terms of a rectifying behavior with R(+1.7 V) ÷ R(-1.7 V) ≈ 20 at λ = 405 nm and R(-1.7 V) ÷ R(+1.7 V) at λ = 570 nm ≈ 5. Higher rectification with R(+3 V) ÷ R(-3 V) ≈ 100 at λ = 405 nm and R(-3 V) ÷ R(+3 V) at λ = 570 nm ≈ 10, were obtained from $\Delta R(\lambda)$ -voltage measurements at the two wavelengths. The $R(\lambda)$ response was linear with incident intensity in the range 0.01 mW - 10 mW with a reasonably high photodetector responsivity at 405 nm, 3 V, of 0.01 mA/W.

4. 2. 3 Photoelectric response in presence of continuous pumping

Additional photoexcitation at 532 nm (wavelength which represents pumping of the bR ground state) resulted in an increase of R(at λ = 412 nm) with the PEDOT:PSS/bR device under negative bias. This R(λ) increase at λ = 412 nm

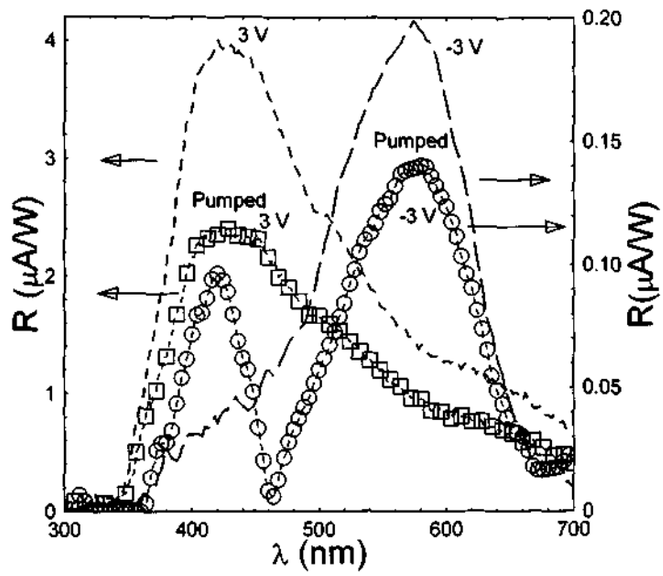

is

Fig. 5. 10 *Effect of photo-pump on R(λ) of ITO/PEDOT:PSS/bR/Al at forward and reverse bias: The pump used was a continuous illumination 2 mW/cm^2 source at 532 nm while the probe beam from the monochromator was chopped at 19 Hz. (The pumping action using the 532 nm source is equivalent to using a source at 570 nm.).*

proportional to the pump intensity and is similar to an effect observed in a pristine single-layered bR device. On the other hand, R(probed at λ = 412 nm) decreases with the pump intensity under the forward bias as shown in Fig. 5. 10. Upon comparing the pump-induced R(λ) to the differential absorption response or the pump-induced absorption changes in bR, the effect of the voltage bias becomes apparent. In case of pump-induced R(λ) of reverse bias shown in Fig. 5. 10, the signature of the intermediate long-lived M state in the photocycle appears in R(λ) due to the difference in the proton release and uptake rate, whereas in the positive

bias the decrease in the M-intermediate signal indicates an introduction of an opposing proton gradient due to the pump. The driving force for these ions are the positive polarized surface. The interface driven FB I_{ph} can be affected if an additional gradient is set-up in the bulk using the photo-pump route. The effective sum of the interface (M-state absorption) I_{ph} and the bulk (pump created I_{ph}) can be observed in both the dc and the modulated measurements. Upon pumping, a decrease in the RMS value of the 405 nm modulated signal at $\omega < 100$ Hz was observed. This is understandable and a decrease can be expected if the M-state component from the pump is not in synchronization with the natural modulated frequency dependent signal response in FB conditions. These subtle effects involving the competing relaxation processes are observed only in the modulated measurements compared to dc mode, where the signal just shows an increase with additional pump The distinct blue-shifted R(λ) (*appearing even in the absence of a pump source*) at positive bias voltage then can be interpreted to arise from the stabilizing effect of the intermediate M-state.

.

5. 2. 4 Verification of absence of PEDOT:PSS contribution to spectral response

Upon changing the redox state of PEDOT:PSS, changes in the optical properties (electrochromic effects) of PEDOT:PSS are also expected [77]. The electrochromic effects can be discounted as a plausible source for spectral changes due to following observations: (i) R(λ) obtained with light incident from the semi-transparent Al side were similar to that obtained for illumination from PEDOT:PSS side as shown in Fig. 5. 11. (ii) The largest reported magnitude of electrochromism in PEDOT:PSS cannot account for the sizable and discrete spectral shifts, in fact the spectral shifts due to an electrochromic reducible and oxidizable PEDOT layer would result in red-shifted R(λ) [77] .

Careful studies of the ITO/PEDOT:PSS/Al device without the bR layer, primarily showed bolometric effect (resistive heating, since PEDOT:PSS is fairly conducting even in its semi-reduced form). This light-induced bolometric current is governed by the absorption and possibly a photo-catalyzed electrochemical reaction at the Al/PEDOT:PSS interface. The following experiments were also performed on the plain PEDOT:PSS devices:

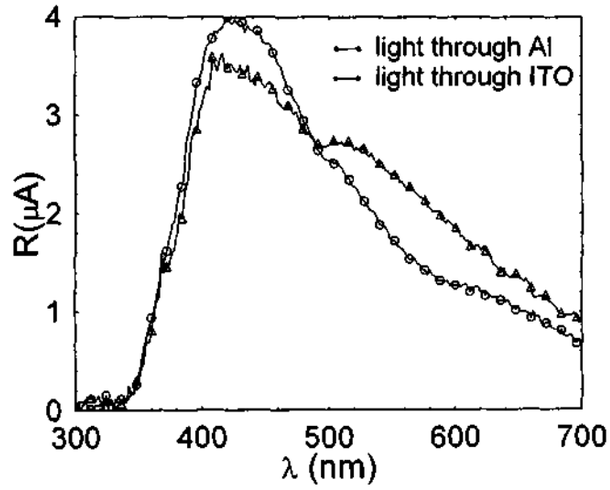

Fig. 5. 11 *Comparison of the photoelectric spectral response R(λ) of ITO/PEDOT:PSS/bR/Al with light incident through ITO and Al.*

The current in dark and light conditions were monitored in ITO/PEDOT:PSS/Au structures. HMDS treated ITO surface was used to prevent direct pin-hole defects and shorting problems, where a thin layer (< 20 nm) of HMDS is introduced prior to PEDOT:PSS coating, and then measuring the I-V in dark and light. The noise analysis of the large dark(dc) signal is also indicative of the thermal processes. The current in a planar (surface) configured geometry Metal-PEDOT:PSS – Metal were monitored and was found to be largely due to thermal processes. The spectral responses of the current in the plain PEDOT:PSS systems due to light at low bias condition covers the entire visible region but does not directly correlate with the absorption spectra of any of its redox-states. The light-induced current in plain PEDOT:PSS system depends on the magnitude of the dc current, i.e., magnitude of I_{light} is proportional to I_{dark}.

The dynamical aspect of the current involve, the rise of the current upon photoexcitation and the decay, after the photoexcitation was switched off and resemble with characteristic thermally-induced changes, which are wavelength independent. A typical time dependence of the current in presence of an optical excitation was as shown in Fig. 5. 12. These results were in direct contrast to

PEDOT:PSS/bR structures where the fundamental nature of the photocurrent was different with the

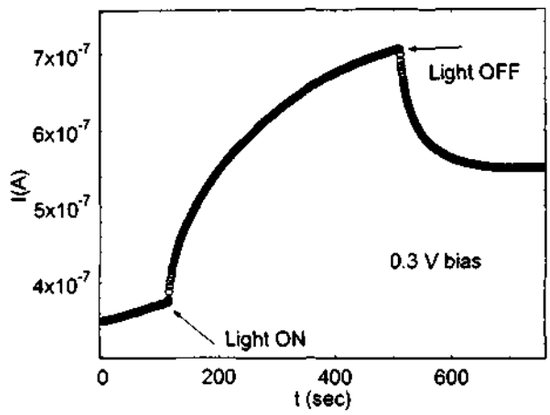

Fig. 5. 12 *The photoresponse of ITO/PEDOT:PSS/Al under a small forward bias at λ = 532 nm.*

following distinct experimental signatures:(i) The dark current in PEDOT:PSS/bR had a capacitive response when a voltage was introduced as shown in Fig. 5. 13 which is in contrast to samples without the bR layer. (ii) The current densities involved in PEDOT:PSS/bR (nA range) was much lower than typical current densities in PEDOT:PSS/electrolyte devices (mA range). (iii) The photo-induced current here (PEDOT/bR) has wavelength dependent dynamics as well as unique

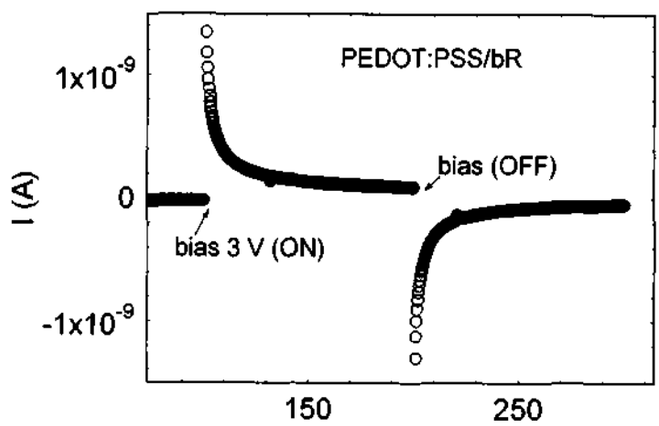

Fig. 5. 13 *The dark current response of ITO/PEDOT:PSS/bR/Al under bias condition*

optical-history dependent features which is discussed later in this chapter. An example of such a dynamics was when the system was probed at 405 nm and then a pump 570 nm was introduced under 3 V bias causing an additional increase in the dc component. However, upon, switching off the 570 nm source, the signal (photo-induced current) decay was much slower (infact non-existent) compared to the decay when 405 nm was switched off. These features are a clear indication of the role of intermediate metastable levels in the bR photocycle. (iv)The heating related features were avoided in bR by operating the device at low bias voltages (minimal dc current). (v) The PEDOT:PSS/bR samples are extremely stable (> 3-months in ambient conditions) exhibiting large signal to noise ratio, unlike the current signals in plain PEDOT:PSS samples.

5. 2. 5. Determination of M state life time

The above mentioned observation lead to the conclusion that the forward bias induces a deprotonated state of bR and shows the spectral features of M state of bR. The M state life time can be estimated by probing the response of the bilayer at λ = 532 nm at different delay times after the forward bias was applied. This method is similar in principle to the pump-probe experiments where the M state was created by the excitation of ground state and the relaxation of the M state to ground state was then probed. The M-state lifetime is then estimated by observing the growth of B-state signal at λ = 570 nm at different intervals after excitation. This approach cannot be directly adapted when bR states are probed by their R(λ) characteristics since the measurements were limited by the time constants involved in the circuit, especially in the range < 10 ms (τ_M ~ 5 ms). However, if the lifetime is sufficiently large then this approach can be adopted by replacing the pump- photoexcitation source with an electrical excitation in the forward bias, the B state can then be subsequently observed at different delay times after the bias is turned off [208]. In the present device upon probing at 532 nm, after a voltage pulse (ON time 20 sec duration) is applied, at regular intervals should give an estimate of the M-state lifetime, as in Fig. 5. 14. Unlike, optical excitation and optical probing, the application of voltage and the measurement of the photocurrent involve electronic, ionic, dielectric, and electrochemical processes

with characteristic associated time constants. A relaxation time constant of ≈ 10 s, is obtained from the enveloping curve covering the periodic responses. In other words, it takes ~ 10 s for the device to regain the unperturbed short-circuit ΔR(λ) value after introducing a perturbation of +3 V pulse and this can be assigned to the life time associated with the M state.

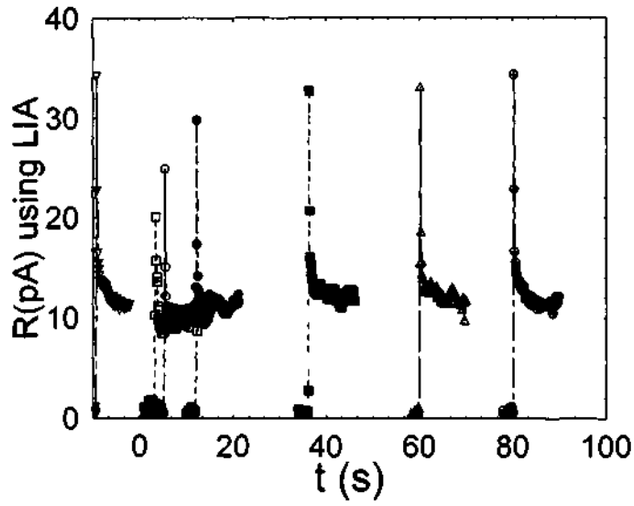

Fig. 5. 14 *Short circuit R(λ) at λ = 532 nm measured using lock in amplifier as function of delay time after applying a 20 s width square-function type positive bias of 3 V in dark, (3 s (□), 5 s (○), 12 s (•), 36 s (■), 60 s (Δ), 80 s (⊕))and is compared with the response prior to bias application (▽).*

5. 2. 6 Time dependant photoelectric responses

Apart from the bias dependence, the differences in the physical processes contributing to the R(λ) at the two spectral regions was also observed in the time dependent and frequency dependent responses. The kinetics/dynamical aspects of the photo-electric processes (1 ps < t < 10 ms) in bR are quite complex with issues such as correlation of the photoelectric signals with the degree of H^+ translocation, role of spectral intermediates and photoreversal still unresolved. The difference in the switching response under different bias conditions to long-duration light pulses was highlighted.

The $I_{tr}(t)$ consists of a substantial dc component which changes with illumination (λ = 405 nm) under a positive bias (1.5 V), unlike a predominant differential response seen in pristine bR system as shown in Fig. 5. 15. The persistence of the light-induced current (sizable dc component, which gradually decreases) with continuous illumination at λ = 405 nm is observed as shown in Fig. 5. 15.

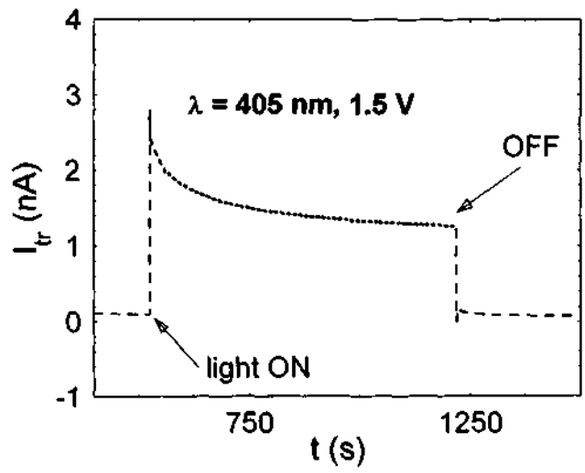

Fig. 5. 15 *The time dependence photoelectric response of ITO/PEDOT:PSS/bR/Al bilayer structure measured using electrometer with ITO biased +1.5 V at λ = 405 nm.*

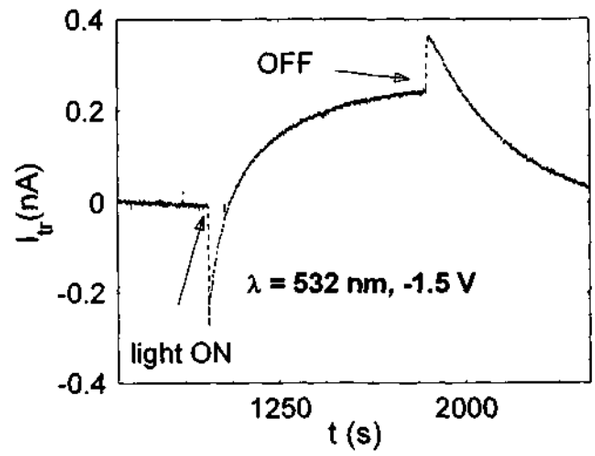

Fig. 5. 16 *The time dependence photoelectric response of ITO/PEDOT:PSS/bR/Al bilayer structure measured using electrometer with ITO biased -1.5 V at λ = 532 nm.*

The electrochemical light controlled activity at the interface in the forward bias acts as a driving force for the diffusion of the protons, away from the polarized interface, towards the Al electrode. The temporal profile can be explained on the basis of this process.

At λ = 532 nm, under a negative bias, the $I_{tr}(t)$ is similar to a displacement current observed in pristine bR system but modified by the changing redox state of the PEDOT with a possible debye layer formation at the interface. The B-state I_{tr} dynamics of PEDOT:PSS/bR is shown in Fig. 5. 16. and is probed by applying a RB of -1.5 V. The background dc component (with light on) shows a gradual decrease with time indicative of the lowering in conductivity of the PEDOT layer, which can be interpreted in terms of a reduction process induced by the light activated proton transfer from the bR side under these bias conditions.

5. 2. 7 History dependence of modulated photoelectric response

R(λ) arising from potential driven electrochemical photo-induced reactions

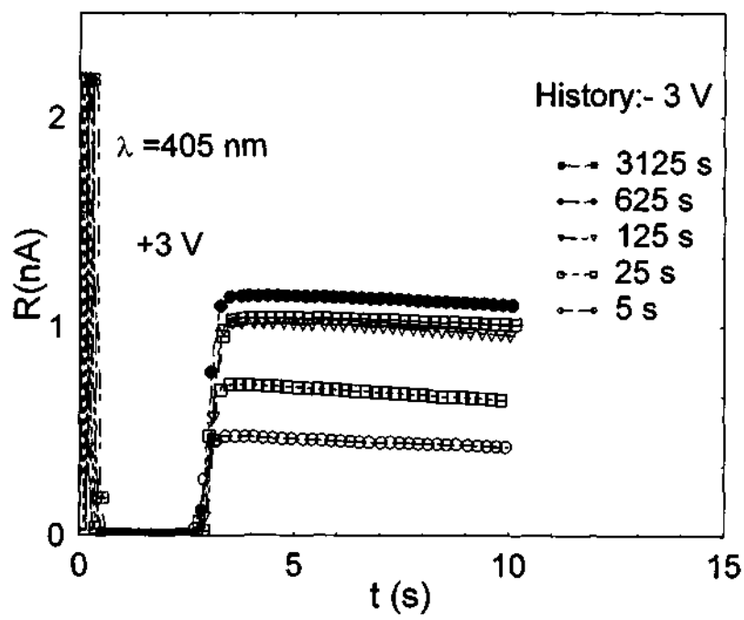

Fig. 5. 17 *The modulated photoelectric response of the ITO/PEDOT:PSS/bR/Al at λ = 405 nm (73 Hz, integration time constant for the lock-in amplifier ~ 30 msec) under +3 V bias measured as a function of time upon voltage reversal, device maintained at reverse bias for different durations.*

is also dependent on the history or the duration of the reverse bias voltage prior to driving to forward bias and vice versa. The evolvement of R(t) subsequent to the application of the bias is quite informative. The voltage reversal effects are shown in Fig. 5. 17 and Fig. 5. 18 and large rectification features were also evident in the two spectral regions. The R(73 Hz, 405 nm) signal strength exhibits a step-function response with respect to time upon reversing the bias voltage, for instance –3 V to +3 V as shown in Fig. 5. 17. The R(t) in the FB at 405 nm gets stabilized relatively fast (< 75 ms), compared to R(t) in RB at532 nm which gradually reaches a steady-state value over a period of several seconds, after a local maximum and a minimum.

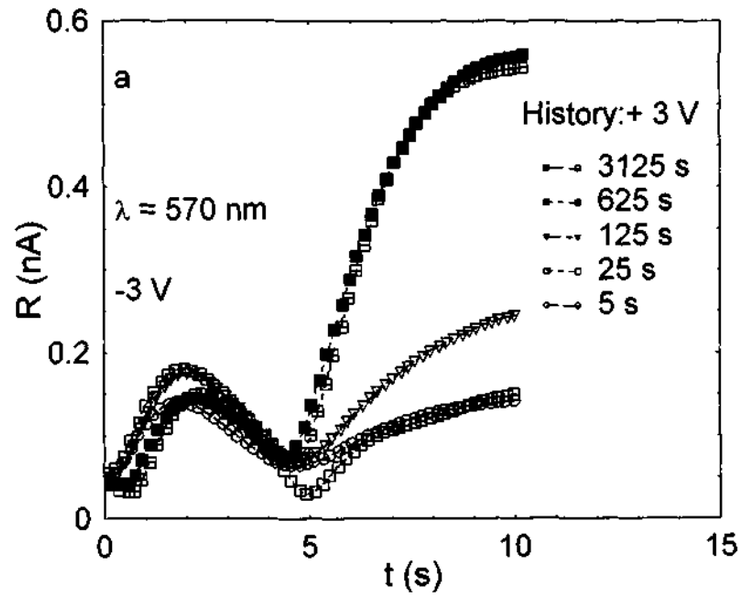

Fig. 5. 18 *The modulated photoelectric response of the ITO/PEDOT:PSS/bR/Al at λ = 532 nm (73 Hz, integration time constant for the lock-in amplifier ~ 30 msec) under -3 V bias measured as a function of time upon voltage reversal, device maintained at forward bias for different duration.*

The threshold time for the R(λ), when the device was switched to the positive bias, and was in the range $t_{threshold} \approx 2.8 \pm 0.5$ sec, and was independent of history, i.e., the duration of the device in the RB conditions. However, the magnitude of the R(λ) signal in this FB condition was dependent on the history, and R(λ) increases with longer exposure to RB conditions upto a duration of ~ 1000 s, beyond which

the history effect is minimal. The threshold time of ~ 2.8 s for the increase in R(λ) can be attributed to the period required for the interface to recover from the reduced state and to facilitate the forward charge transport process.

In case of reversal from FB to RB, the threshold time of ~ 5 s (Fig. 5. 18) for the increase in R(λ) was observed and can be attributed to the period required for the interface to recover from the oxidized state and facilitate the charge transport process. Another interesting inference from the FB to RB reversal experiment is that the history-duration-time corresponding to the saturation value for R(λ) can be a measure of the upper limit of the M-state relaxation lifetime, which is in the order of 100 s. The time dependence of R(532 nm, 73 Hz) response shown in Fig. 5. 18 shows a local maxima/peak at t ~ 2 s upon reversal of the bias from +3 V to –3 V. This initial peak also shows subtle history-dependent pattern in magnitude and position, that can be associated with competing process of the decreasing conductivity of PEDOT:PSS arising from the photo-induced reduction process from the proton transfer and the increasing efficiency of this transfer process with increasing time.

5. 3 Summary

In conclusion, the spectroscopic signature of the M-state in bR was determined using opto-electrical measurements, and a strategy for controlling the optically induced biomolecular events in bR using functional conducting polymer interfaces was demonstrated. This strategy would be especially relevant in developing schemes for detailed studies of the intermediate states in functional proteins such as bR and its variants. Conducting polymers such as PEDOT:PSS are promising multi-functional electrode-contacts for studying the signal transduction in membrane proteins.

It has been shown that ITO electrodes in these devices can be entirely replaced by PEDOT:PSS, which also can be pixelated and addressed with relative ease on any flexible-soft substrates with a variety of printing techniques. The combined spectra arising from the two bias conditions observed in the present system nearly covers the entire visible spectral range and along with factors such as water based bio-compatible processing techniques, form an important basis for an artificial retina. Methods based on our strategy for tapping into the biomolecular

events can overcome the inability to extend the lifetime of the M-state which has been a severe limitation in bR based applications.

Chapter 6

Conjugated polymer/Nanocrystallites bilayer structure

Conjugated polymers have been utilized as active layers in light-emitting diodes (LEDs) with the emission spectral-range determined by the chemical structure. Peak output up to 10^6 Cd/m^2 have been recently reported for polymer devices [209]. Materials such as semiconductor nanoclusters have also been demonstrated as active layers for emission and detection devices with the optical range of interest tuned by size selection of the nanoparticles [210, 211]. Reports on heterostructure devices with an inorganic layer of CdS and a polymer light emitter show the advantage of the high-charge transporting properties of an inorganic semiconductor and the enhanced emission efficiency of the polymer emitter [212]. It has been observed, that the work function of the nanoparticles can be matched with that of the metal contacts improving the electron injection efficiency. It is also known, that the emission colour governed by the recombination zone can be controlled by the magnitude of the external voltage [210]. Studies of blends consisting of nanoparticles in a polymer media where the nanoparticles act as a sensitizer for the photocurrent and as active emitters for electroluminescence (EL) have also been reported [213-215]. Previous reports shows that polymer-based devices can be utilized as a LED in the forward bias and a photodetector in the reverse bias [216]. The conjugated polymer/nanocrystallites interface in the present report was explored with these perspectives in the background.

6. 1 Nanocrystallites – A brief introduction

Nanocrystallites with typical dimensions in the nanometer range belong to a unique class of materials with their physical and chemical properties distinctly different from the corresponding bulk materials [217-220]. For example the band gap of a semiconducting material along with its other electronic and optical

properties can be changed over a wide range of values by controlling the particle size. The fact that one can tune properties of materials just by varying their sizes has aroused enormous interest [221, 222]. This has led to the rapid advancement in this area over the last two decades The changes in the material properties at such length scales are primarily driven by two effects increased surface to volume ratio with reduction in the particle size and the changes in the electronic structure at such finite sizes The latter effect known as the quantum confinement effect is substantial in case of semiconductors leading to drastic changes in their optical and electronic properties [223]. Some of the interesting manifestations of such size dependent properties in the quantum size limit are pronounced shifts in the absorption and emission features, higher optical nonlinear coefficients and large oscillator strengths. Structural studies confirm that even at such small sizes of a few nanometers the core of these tiny particles are crystalline often with structure and lattice parameters similar to those of the corresponding bulk material.

Apart from the effect of a large surface area there exists a particular size limit below which the material properties undergo a drastic change in their optical and electrical properties as a function of their size. Such effects arise due to the systematic variation of the density of the electronic energy levels with size. In the language of solid-state physics this is referred to as the change in the density of states with the dimensionality. For an infinite bulk solid with free electron like states the variation of the density of states versus energy has a typical $E^{-1/2}$ dependence. With additional degree of confinement along one two and three dimensions there is a marked change in the density of states [220]. In case of nanocrystallites there is a three dimensional confinement of the matter corresponding to the quantum box. In this limit, the electronic energy levels of a solid change with the size depending on the type of bonding and local hopping interactions in the system. The changes in the optical and electrical properties occur at different size regimes in case of metals and semiconductors while there is hardly any observable effect on the material properties with size in case of molecular solids. The bandwidth in any solid is determined by the strength of the hopping interactions between the orbital of the neighboring atoms. In case of molecular or Vander Waal solids the hopping interactions responsible for band formation are weak leading to narrow bands. The corresponding wave functions

are primarily localized at most over a few interatomic distances. Therefore there is hardly any noticeable change in the properties of this class of materials even at a fairly small size of the nanocrystallites. The effect of quantum confinement is in general more pronounced near the zone edges than the center. This is because the energy dispersion near the center of the band compared to the edges is such that it corresponds to an increase in the effective mass at the center leading to less quantum size effects (effective mass approximation) [224]. Additionally, the center of the bands in general has a much higher density of states compared to the band edges. In metals the Fermi level often lies near the band center and hence the spatial confinement effects on their optical and electronic properties are less prominent until very small sizes of the crystallites are attained. On the other hand in semiconductors the Fermi level lies in the band gap region and hence the band edges dominate the optical and electrical excitations leading to a more drastic change in the optical and electronic properties even at relatively larger sizes.

6. 2 Results and discussion

Organically capped nanoparticle photocurrent efficiencies are very high and are comparable to that of bulk CdS. The possibility of synergistically combining the efficient photoconduction (PC) properties of the inorganic and the EL properties of the polymer in a single device were explored. The results on such hybrid devices, where the photoconductivity characteristics dominated by the quantum size of the inorganic semiconductor and the enhanced EL spectral feature originated predominantly from the polymer component were discussed. The potential of such devices where windows for the detection and emission can be selected by nanoparticle-size engineering and/or modifying the chemical structure of the polymer were demonstrated.

The results for the CdS-44 based device are shown in Fig. 6.1. The photocurrent onset is sharply defined at ≈ 4700 Å, which also corresponds to the absorption edge, and is highly efficient with a response of I_{ph} ≈ 100 nA for an incident photon intensity of 1.0 mW/cm^2 at 4100 Å. The band edge of the nanocluster is blue shifted with respect to bulk CdS as a result of quantum confinement of free carriers in the nanoparticles (Fig 6. 2). Measurements were done for CdS-22 also and

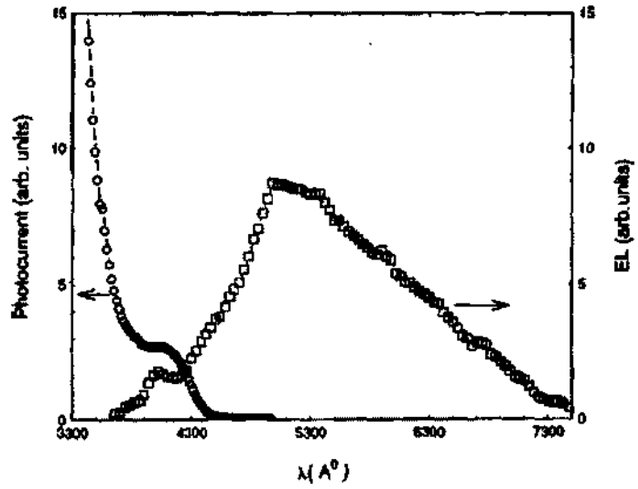

Fig. 6. 1 *Spectral response of photocurrent (o) and EL (□) in CdS-44-only device.*

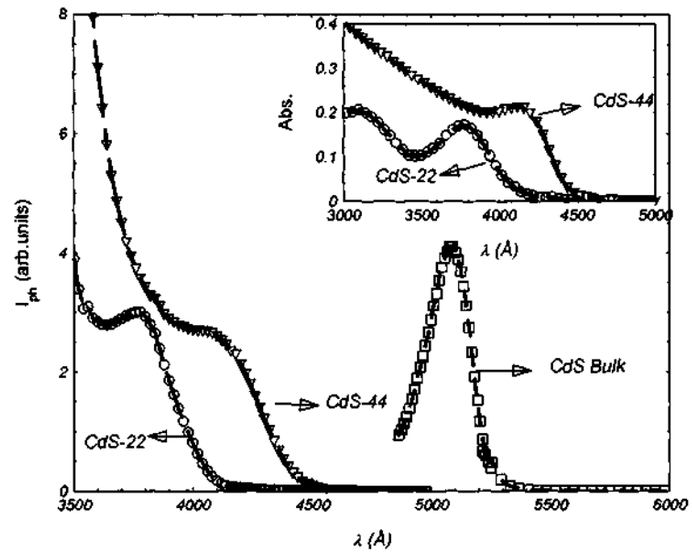

Fig. 6. 2 *The photocurrent spectral response of CdS-22, CdS-44 and bulk CdS. Inset shows the absorbance spectra of the CdS-22 and CdS-44.*

the results were consistent with particle-size-dependent band-edge results in CdS (Fig. 6. 2). However, the EL observed in the nanoparticle is relatively less efficient, ≈ 0.5 Cd/m^2, and is dominated by the trap emission rather than band-edge emission. This aspect of trap emission is observed in the PL emission in the film

also. The relative contribution of the trap emission is higher in the film form than in the solution form. The origin of the trap-dominated emission in these samples has been explained on the basis of recombination via surface localized states partly arising from the nanoparticle capping layer[225].

The EL spectral response results for three different heterostructures with different types of polymer are displayed in Fig. 6. 3. The light-emission color scales with the band gap of the polymer with maxima at 6200, 5400, and 5250 Å for CdS-44/P3HT, CdS-44/MEHPPV, and CdS-44/6FPBO devices, respectively. The EL spectra are closer to the pure polymer responses with efficiency nearly an order of magnitude higher than CdS-only devices and polymer-only devices. It has been observed in LED devices based on nanocrystals, which have high-band-edge PL yield, the insertion of a hole transporting polymer layer enhances the nanocrystal band-edge emission characteristics [226]. In the present case the results can be interpreted in terms of the CdS-44 layer enhancing the polymer emission characteristics. The maximum brightness achieved was in the range of 30 Cd/m^2 and external efficiencies were in the range of 10^{-3} Lm/W at current levels of 20 mA. It is expected that the absorbance and the emission from the polymer layer will modulate the emission from the CdS layer, however, in the present case the thickness of the emitting polymer layer in the devices is significantly less than $1/\alpha_{max}$, where α is the absorption coefficient. 6FPBO is an electron transporting emitter [227] while MEHPPV and P3HT are predominantly hole transporting emitting polymers. The recombination in the 6FPBO device is closer to the PVK/6FPBO interface in the 6FPBO layer with minimum trap emission contribution from the nanocluster layer resulting in a sharper emission as shown in Fig. 6. 3.

The issue of PL quenching, charge separation, and transport in nanocrystal CdS/MEHPPV composite blends have been studied in detail. The results correlate quenching with improved quantum yield for charge separation. In the present case of bilayers with completely segregated phases, the possibility of Forster transfer of the exciton to the nanoparticles will be effective only at the interface leading to a possible emission quenching. Initial results on PL showed negligible quenching effects with excitation energies corresponding to that of the polymer in CdS-44/P3HT. Quenching effects can be minimized by reducing Forster transfer rates,

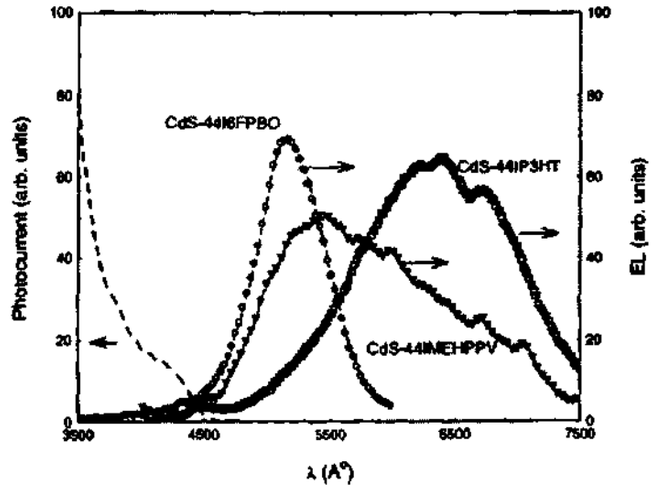

Fig. 6. 3 *Normalized EL spectral response of each device along with the short-circuit photocurrent (dashed).*

by choosing polymers of appropriate electron affinity values and suitable capping materials for the nanocrystals. The EL efficiency can also be enhanced by optimizing device parameters such as thickness with prior information on values of mobility and electron–hole pair diffusion length to have radiative recombination away from the interface.

In stark contrast, the short-circuit photocurrent spectral response in all the three devices is identical to that of a CdS-44 layer independent of the type of the polymer as shown in Fig. 6. 3. The polymer signature is observed but $I_{ph}(\lambda)$ in the nonabsorbing region of CdS-44 and absorbing region of the polymer is less than 3–4 orders in magnitude than $I_{ph}(\lambda)$ in the CdS-44 absorption region. A significant separation width of nearly 2000 Å (2.0 eV) in the visible range between the emission maxima and the photocurrent region is observed in the CdS-44/P3HT device. The external zero-bias photocurrent efficiency in all the hybrid devices is in a similar range as that of pure nanoparticle devices with a responsivity of ≈ 100 mA/W. It is expected that if the polymer thickness is increased to be comparable to the absorption depth, the spectral response would be modified. The large photocurrent primarily reflects the high efficiencies commonly observed in CdS-based detectors due to high absorption and efficient charge-carrier separation. *I* –V measurements of the devices indicate nonlinear behavior and characteristics of a

LED. The magnitude of the current density for light emission in the bilayer devices is not significantly different compared with that of the single-layer polymer-only devices. The emission intensity scales linearly with the current in the device. The nonlinear I –V curve in Fig. 6. 4 shows two distinct regions as indicated by different I(V) behavior, with a weaker dependence at the higher voltage regime suggesting multicomponent features. The relative position of the band energy levels of the different regions of the device is depicted in the inset of Fig. 6. 4 with assumed values of the electron affinity for the nanocluster.14 The barrier present at the inorganic–organic interface could lead to the plateauing of the I –V curve and may be the cause for a voltage-dependent recombination zones giving rise to voltage-controlled color emission in such devices. The magnitude of the current and the onset voltage show variation with the type of the polymer as shown in Fig. 6. 4. The tunability of a Shottky diode based on a semiconductor/ conjugated polymer (doped) interface has been explored electrochemically manipulating the work function of the conjugated polymer. In the present case, the work function

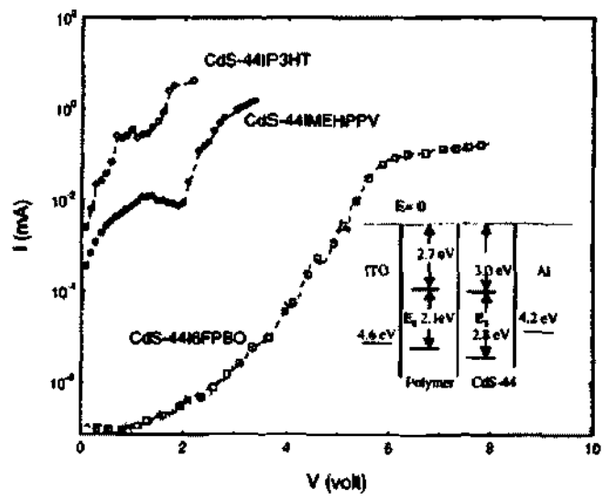

Fig. 6. 4. *Current vs voltage curves for the devices and the inset is a typical band diagram representing the device with assumed values for CdS-44 P3HT representing the polymer layer.*

along with the charge-carrier concentration and the nature of the interface will also decide the LED characteristics.

6. 3 Summary

Dual properties of photoconduction and electroluminescence in hybrid devices consisting of a nanocluster semiconductor layer and a polymer were explored. It was observed that the photocurrent spectral response and efficiency in these multilayer devices were similar to that of the semiconductor component, while the EL spectral responses were closer to that of the polymer layer. The results were confirmed using the nanoparticle semiconductor, cadmium sulphide CdS, of different particle sizes and polymers representing a wide spectral range. A general feature of efficient photocurrent spectral response corresponding to nanoparticle and an appreciable EL response corresponding more to the active polymer are observed in all devices and results in wide, separated spectral windows. Current– voltage responses also indicate possibilities of added tunability in these devices.

Summary and future directions

The results of various investigations carried out in this thesis can be summarized as follows:

The bilayer device consisting of a p-type polymer and n-type polymer was studied in detail. Poly (3-alky thiophene) (P3OT) and poly(2-methoxy, 5-(2-ethylhexoxy)-1, 4-phenylene vinylene) (MEHPPV) were used as p-type materials and poly(benzimidazobenzophenthroline) (BBL) was used as n-type polymer. The photocurrent generation mechanism in these bilayer devices were studied using various techniques like photocurrent spectral response, transient photocurrent measurement for pulse duration varying from 5 ns to few seconds, intensity modulated photocurrent spectroscopy (IMPS). The bilayer structure made of P3OT/BBL showed charging phenomena, which reduces the photocurrent efficiency. Such kind of effect were negligible in the case of MEHPPV/BBL bilayer. The interfacial processes were studied using thermally stimulated current measurements, light of same and different phase lags incident on both sides of the bilayer structure and IMPS. In order to arrive to a general conclusion, studies were carried out on bilayers of different thickness of the individual layers. The MEHPV/BBL bilayer showed a higher photosensitivity (S) of 0.2 A/W, incident photon to current conversion (IPCE) efficiency of 48%, fill factor (FF) of 10% and power conversion efficiency (PCE) of 1.5% compared to that of P3OT/BBL bilayer, which showed S of 60mA/W, IPCE of 14%, FF of 1% and PCE of 0.1%. The open circuit photovoltage (V_{oc}) of 0.9 V was similar to the fermi energy level difference between the polymers. The bilayers were compared with single layer structures of similar thickness and found that the photocurrent efficiency increased four orders of magnitude in the case of MEHPPV/BBL bilayer and two orders in the case of P3OT/BBL bilayer.

From the above mentioned investigations it has been understood that the interfaces energy barrier plays an important role in deciding various optoelectronics properties of the devices made of organic molecules. Polymers with suitable HOMO-LUMO levels can be tailored by having multiple layers to form quantum well structure. If we have a three layer device in which the middle layer HOMO-LUMO levels are different from the other two layers, and the

thickness of the layers are in few nano meters, this can be achieved. However, it may be necessary to use other film formation techniques such as, self assembly or Langmuir blodget technique to achieve this. The principle of operation here, is that the device should be able to respond to incident light whose energy equal to the energy level difference of the middle layer with respect to the other two layers.

The synergistic process at the interface due to the individual effects in the layer of conducting polymers/bacteriorhodopsin were investigated using photoelectric spectral response, (in presence of a electric field and in absence, in presence of a pump beam of monochromatic light and in absence of it), time and frequency dependence of photoelectric response. The single layered bR structure showed spectral responses similar to that reported in literature. A modeling of the photocurrent spectral response was carried out. bR showed spectral response features of the ground state bR with a peak at 570 nm and the spectral weight shifted to 412 nm in presence of a pump beam of wavelength (λ) = 532 nm of 2mW/cm^2. We found a relation between the pumping intensity and the population of B state and M state. The bilayer structure of conducting polymer, PEDOT:PSS/bR showed similar photoelectric spectral response as that of single bR layer structure but showed very different photoelectrical response in presence of a forward bias (PEDOT:PSS biased positive compared to bR). The forward bias photoelectrical response showed stabilization of M state with a peak at ~412 nm. The voltage dependent photoelectric response showed a rectification behavior for an incident λ at 405 nm. The photoelectric response was history dependent. The PEDOT:PSS contribution to the photoelectric response was verified and was found to be negligible. The M state lifetime of ~ 20 s was estimated in this system.

This research can have a bearing in the development of artificial retinas which can have biocompatible conducting polymers and functional bio-molecules as the major active components. As we have seen two different spectral response has been achieved by simple proceedure of reversing a low voltage bias to the device. This has been achieved in eye retina by different rhododpsin encapsulated in different proteins scattered over the retina. By having a pixelated bilayer structure as ours and giving different bias to different regions of the bilayer structure we can actually reproduce the image we have seen with our naked eye.

Another prospect of such a system is creating a photoelectrochemical field effect transistor. Here the channel is a polymer and the dielectric medium is the membrane. The drain current can be controlled by the reduction or oxidation of the polymer by light induced ion displacement in the membrane.

Dual properties of photoconduction and electroluminescence (EL) in hybrid devices consisting of a nanocluster semiconductor layer and a polymer were studied. It was observed that the photocurrent spectral response and efficiency in these multilayer devices were similar to that of the semiconductor component, while the EL spectral responses were closer to that of the polymer layer. The results were confirmed using the nanoparticle semiconductor, cadmium sulphide CdS, of different particle sizes and polymers representing a wide spectral range. A general feature of efficient photocurrent spectral response corresponding to nanoparticle and an appreciable EL response corresponding more to the active polymer were observed in all devices and results in wide, separated spectral windows. Current– voltage responses also indicate possibilities of added tunability in these devices.

The present investigation lead to the prospect of tailoring nanoparticles on polymers by various methods to obtain the desired optoelectronic properties. The present investigation leads to new ideas of nanoparticles incorporation into a composite form and layer structure where multifunction can be achieved on a single device itself.

References

1. J. Mort, Polymers. Electrical properties. Encyclopedia of Phys. Sci. Tech. **11**, 48 (1987).

2. A. J. Heeger, Rev. Mod. Phys. **73**. 681 (2001).

3. A, G. MacDiarimid, Rev. Mod. Phys. **73**, 701 (2001).

4. H. Shirakawa, Rev. Mod. Phys. **73**, 713 (2001).

5. H. Shirakawa, E. J. Louis, A. G. Madiarmid, C. K. Chiang and A. J. Heeger, J. Chem. Soc. Comm. 557 (1977).

6. C. K. Chiang, C. R. Jr. Fincher, Y. W. Park, A. J. Heeger, H. Shirakawa and E. J. Louis, Phys. Rev. Lett. **39**, 1098 (1977).

7. S. Roth and H. Bleier, Adv. Phys. **36**, 386 (1987).

8. Handbook of Conducting Polymers, 2nd ed. (Eds: T. A. Skotheim, R. L. Elsenbaumer, J. R. Reynolds), Marcel Dekker, New York 1998.

9. A. Tsumura, H. Koezuka and T. Ando, Appl. Phys. Lett. **49**, 1210 (1986).

10. A. Assadi, G. Svesson, M. Willander and O. Inganas, Appl. Phys. Lett. **53**, 195 (1988).

11. J. H. Burroughs, C. A. Jones and R. H. Friend, Nature. **335**, 127 (1988).

12. J. H. Burroughes, D. D. C. Bradley, A. R. Brown, R. N. Marks, K. Mackay, R. H. Friend, P. L. Burn and A. B. Holmes, Nature. **347**, 539 (1990).

13. G. Gustafsson, Y. Cao, G. M. Treacy, F. Klavetter, N. Colaneri and A. J. Heeger, Nature. **357**, 477 (1992).

14. P. .L. Burns, A. B. Holmes, A. Kraft, D. D. C. Bradley, A. R. Brown, R. H. Friend and R. W. Gymer, Nature. **357**, 47 (1992).

15. R. H. Friend, R. W. Gymer, A. B. Holmes, J. H. Burroughs, R. N. Marks, C. Taliani, D. D. C. Bradley, D. A. Dos Santos, J. L. Bredas, M. Logdlund and W. R. Salaneck, Nature. **397**, 121 (1999).

16. R. H. Friend, Physics World, 35, (June,1999).

17. C. J. Brabec, N. S. Sariciftci and J. C. Hummelen, Adv. Funct. Mater. **11**, 15 (2001).

18. N. S. Sariciftci, Curr. Opin. Sol. Sta. Mater. Sci. **4**, 373 (1999).

19. J. Nelson, Curr. Opin. Sol. Sta. Mater. Sci. **6**, 87 (2002).

20. C. J. Drury, C. M. J. Mutsaers, C. M. Hart, M. Matters and D. M. de Leeuw, Appl. Phys. Lett. **73**, 108 (1998).

21. G. H. Gelinck, T. C. T. Geuns and D. M. de Leeuw, Appl. Phys. Lett. 77, 1487 (2000).

22. H. Sirringhaus, N. Tessler and R. H. Friend, Science. **280**, 1741 (1998).

23. K. Yoshino, M. Tabata, K. Kaneto and T. Ohsawa, Jap. J. Appl. Phys. **24**, L693 (1985).

24. Y. Yang and A. J. Heeger, Appl. Phys. Lett. **64**, 1245 (1994).

25. M. Gross, D C. Muller, H-G Nothfer, U Scherf, D Neher, C. Brauchle and K. Meerholz, Nature. **405**, 661 (2000).

26. F. Zhang, M. Johansson, M. R. Andersson, J. C. Hummelen and O. Inganas, Adv. Mater. 14, 662 (2002).

27. P. J. Reucroft and H. Ullal, Sol. Energy. Mater. **2**, 217 (1979-80).

28. B. R. Weinberger, S. C. Gau and Z. Kiss, Appl. Phys. Lett. **38**, 555 (1981). (28a). J. L. Bredas, J. P. Calbert, D. A. da Silvo Filho and J. Cornill, Proc. Nati. Acad. Sci. USA. 99, 5804 (2002).

29. N. W. Ashcroft and N. D. Mermin, Solid State Physics (Saunders, Philadelphia, 1976).

30. E. M. Conwell, Phys. Rev. **103**, 51 (1956).

31. N. F. Mott, Canadian J. Phys. **34**, 1356 (1956).

32. N. F. Mott and E. A. Davis, Electronic Processes in Noncrystalline Materials (Clarendon, Oxford, 1971).

33. A. Miller and E. Abrahams, Phys. Rev. **120**, 745 (1960).

34. H. Bottger and V. V. Bryksin, Hopping Conduction in Solids (Akademie-Verlag, Berlin, 1985).

35. B. I. Shklovskii and A. L. Efros, Electronic Properties of Doped Semiconductors (Springer-Verlag, Berlin, 1984).

36. A. Madan, M. P. Shaw, Physics and application of amorphous semiconductors (Academic Press, Boston, 1988)

37. B. J. Shklovskii and A. L. Efros, Electronic properties of disordered semiconductors, (Springer, Berlin, 1984)

38. Z. H. Wang, E. M. Scherr, A. G. MacDiramid and A. J. Epstien, Phys. Rev. B. **45**, 4190 (1992).

39. Z. H. Wang, A. Ray, A. G. macDiramid and A. J. Epstein, Phys. Rev. B. **43**, 4373 (1991).

40. P. Sheng, B. Abeles and Y. Arie, Phys. Rev. Lett. **31**, 44 (1973).

41. P. Sheng, Phys. Rev. B. **21**, 2180 (1980).

42. A. J. Heeger, S. Kivelson, J. R. Schrieer and W. P. Su, Rev. Mod. Phys. **60**, 781 (1988).

43. C. H. Lee, G. Yu and A. J. Heeger, Phys. Rev. B **47**, 15543 (1993).

44. H. Bassler, V. Brandl, M. Deussen, E. O. G□obel, R. Kersting, H. Kurz, U. Lemmer, R. F. Mahrt and A. Ochse, Pure Appl. Chem. **67**, 377 (1995).

45. U. Rauscher, H. Bassler, D. D. C. Bradley, and M. Hennecke, Phys. Rev. B. **42**, 9830 (1990).

46. R. Kersting, U. Lemmer, R. F. Mahrt, K. Leo, H. Kurz, H. Bassler and E. O. Gobel, Phys. Rev. Lett. **70**, 3820 (1993).

47. R. Kersting, U. Lemmer, M. Deussen, H. J. Bakker, R. F. Mahrt, H. Kurz, V. I. Arkhipov, H. Bassler and E. O. Gobel, Phys. Rev. Lett. **73**, 1440 (1994).

48. M. Deussen, M. Scheidler and H. Bassler, Synth. Met. **73**, 123 (1995).

49. S. Barth and H. Bassler, Phys. Rev. Lett. **79**, 4445 (1997).

50. Primary Photoexcitation in Conjugated Polymers, ed. N.S. Sariciftci, World Scientific Publishing, Singapore, Ch.X (1998).

51. H. Antoniadis, B. R. Hsieh, M. A. Abkowitz, S. A. Jenekhe and M. Stolka, Synth. Met. **62**, 265 (1994).

52. I. D. Parker, J. Appl. Phys. **75**, 1656 (1994).

53. G. Yu, K. Pakbaz and A. J. Heeger, Appl. Phys. Lett. **64**, 3422 (1994).

54. R. N. Marks, J. J. M. Halls, D. D. C. Bradley, R. H. Friend and A. B. Holmes, J. Phys. Cond. Matt. **6**, 1379 (1994).

55. M. G. Harrison, J. Grüner and G. C. W. Spencer, Phys. Rev. B. **55**, 7831 (1997).

56. R. C. Nelson, J. Opt. Soc. Am. **46**, 13 (1956).

57. C. W. Tang, Appl. Phys. Lett. **48**, 183 (1986).

58. L. S. Roman, W. Mammo, L. A. A. Patterson, M. R. Anderson and O. Inganas, Adv. Mater. **10**, 774 (1998).

59. L. C. Chen, D. Godovsky, O. Inganas, J. C. Hummelen, R. A. J. Janssens, M. Svensson and M. R. Anderson, Adv. Mater. **12**, 1367 (2000).

60. N. S. Sariciftci, L. Smilowitz, A. J. Heeger and F. Wudi, Science, **258**, 1474 (1992).

61. N. S. Sariciftci, Prog. Quantum Electronics **19**, 131 (1995).

62. G. Yu, J. Gao, J. C. Hummelen, F. Wudi and A. J. Heeger, Science **270**, 1789 (1995).

63. G. Yu and A. J. Heeger, J. Appl. Phys. **78**, 4510 (1995).

64. L. S. Roman, L. C. Chen, L. A. A. Patterson, W. Mammo, M. R. Anderson, M. Johansson, and O. Inganas, Synth. Met. **102**, 977 (1999).

65. C. H. Lee, G. Yu, D. Moses, K. Pakhaz, C. Zhang, N. S. Sariciftci, A. J. Heeger and F. Wudl, Phys. Rev. B. **48**, 15425 (1993).

66. J. J. Halls, K. Pichler, R. H. Friend, S. C. Moratti and A. B. Holmes, Appl. Phys. Lett. **68**, 3120 (1996).

67. J. J. M. Halls, C. A. Walsh, N. C. Greenham, F. A. Marseglia, R. H. Friend, S. C. Moratti and A. B. Holmes, Nature **376**, 498 (1995).

68. S. E. Shaheen, R. Radspinner, N. Peyghambarian and G. E. Jabbour, Appl. Phys. Lett. **79**, 2996 (2001).

69. K. Tada, M. Onoda, A. A. Zakhidov and K. Yoshino, Jpn. J. Appl. Phys. Part2. **36**, L306 (1997): C. J. Brabec, N. S. Sariciftci, and J. C. Hummelen, Adv. Funct. Mater. **11**, 15 (2001).

70. S. A. Jenekhe and S. Yi, Appl. Phys. Lett. **77**, 2635 (2000).

71. A. Kraft, A. C. Grimsdale and A. B. Holmes, Angew. Chem. Int. Ed. Engl. **37**, 402 (1998).

72. Handbook of Organic Conductive Molecules and Polymers, Vols. 1±4 (Ed: H. S. Nalwa), Wiley, Chichester, UK 1997.

73. J. Joo, Z. Oblakowski, G. Du, J. P. Pouget, E. J. Oh, J. M. Wiesinger, Y. Min, A. G. Macdiarmid and A. J. Epstein. Phys. Rev. B. **49**, 2977 (1994).

74. K. Mizoguchi, M. Nechtachein, J. P. Travers and C. Menardo, Phys. Rev. Lett. **63**, 66 (1989).

75. P. Philips and H. L. Wu, Science. **252**, 1805 (1991).

76. Z. H. Wang, C. Li, E. M. Scherr, A. G. MacDiarmid and A. J. Epstein, Phys. Rev. Lett. **66**, 1745 (1991).

77. L. B. Groenendaal, F. Jonas, D. Freitag, H. Pielartzik and J. R. Reynolds, Adv. Mater. **12**, 481 (2000).

78. M. Chen, D. Nilsson, T. Kugler, M. Berggren and T. Remonen, Appl. Phys. Lett. **81**, 2011 (2002).

79. H. W. Huer, R. Wehrmann and S. Kirchmeyer, Adv. Fun. Mater.**12**, 89 (2002).

80. P. Chandrasekhar, B. J. Zay, G. C. Birur, S. Rawal, E. A. Pierson, L. Kauder and T. Swanson. Adv. Fun. Mater. **12**, 95 (2002).

81. A. J. Epstein, J. Joo, R. S. Kohlman, G. Du, A. G. MacDiramid, E. J. Oh, Y. Min, J. Tsukamoto, H. Kaneko and J. P. Pooger, Synth. Met. **65**, 149 (1994).

82. L. Zuppiroli, M. N. Bussac, S. Paschen, O. Chauvet and L. Forro, Phys. Rev. B. **50**, 5196 (1994).

83. B. Sixou, N. Mermilliod and J. P. Travers, Phys. Rev. B. **53**, 4509 (1996)

84. M. Reghu, C. O. Yoon, C. Y. Yang, D. Moses, P. Smith, A. J. Heeger and Y. Cao, Phys. Rev. B. **50**, 13931 (1994).

85. R. Rosenbaum, Phys. Rev. B. **44**, 3599 (1991).

86. D. Oesterhelt and W. Stoeckenius, Nature New Biol. (London). **233**, 149 (1971).

87. D. Oesterhelt and W. Stoeckenius. Proc. Natl. Acad. Sci. USA. **70**, 2853 (1973).

88. Y. Shen, C. R. Safnya, K. S. Liang, A. F. Ruppert and K. J. Rothschild, Nature. 366, 48 (1993).

89. W. Stoeckenius, R. H. Lozier and R. A. Bogomolni, Biochim. Biophys. Acta. **505**, 215 (1979).

90. W. Stoeckenius and R. A. Bogomolni, Ann. Rev. Biochem. **52**, 587 (1982).

91. T. Kouyama, K. Kinosita and A. Ihegami, Adv. Biophys. **24**, 123 (1988).

92. Y. Mukohata and Y. Kaji, Arch. Biochem. Biophys. **206**, 72 (1981).

93. J. L. Spudich and R. A. Bogomolni, Nature. **312**, 509 (1984).

94. A. Danon and W. Stoecknius, Proc. Natl. Acad. Sci. USA. **71**, 1234 (1974).

95. R. J. P. Williams, J. Theoret. Biol. **1**, 1 (1961).

96. R. J. P. Williams, J. Theoret. Biol. **3**, 209 (1962).

97. P. Mitchell, Biol. Rev. **41**, 445 (1966).

98. D. Kuschmitz and B. Hess, Biochemistry. **20**, 5950 (1981).

99. R. Renthal and C. H. Cha, Biophy. J. **45**. 1001 (1984)

100. B. Ehrenberg, T. G. Ebrey, N. Friedman and M. Sheves, FEBS Lett. **250**, 179 (1989).

101. M. Kates, S. C. Kushwaha and G. D. Sprott, Meth. Enzymol. **88**, 98 (1982).

102. R. Renthal, Biophy. J. **55**, 581 (1989).

103. A. E, Blaurock and G. I. King, Science. **196**, 1101 (1977).

104. K. A. Fisher, K. Yanagimoto and W. Stoeckenius, J. Cell. Biol. **77**, 611 (1978).

105. G. Varo, Acta. Biol. Acad. Sci. **32**, 301 (1981).

106. K. Barbas, A. Der, Zs. Dancshazy, P. Ormos, M. Marden and L. Keszthelyi, Biophy. J. **43**, 5 (1983).

107. Y. Kimura, M. Fujiwara and A. Ikengami, Biophys. J. **45**, 615 (1984).

108. L. Keszthelyi and P. Ormos, FEBS Lett. 109, 189 (1980).

109.K. Nakanishi, V. Balogh-Nair, M. Arnaboldi, K. Tsujimoto and B. Honig, J. Am. Chem. Soc. **102**, 7945 (1980).

110.S. Druckman, M. Ottolenghi, A. Pande, J. Pande and R. H. Callender, Biochemistry. **21**, 4953 (1982).

111.P. Scherrer, M. K. Mathew, W. Sperling and W. Stoeckenius, Biochemistry. **28**, 829 (1989).

112.D. Mitchell and G. W. Rayfield, Biophys. J. **49**, 563 (1986).

113.E. Racker and W. Stoeckenius, J. Biol. Chem. **249**, 662 (1974).

114.R. Hartmann and D. Oesterhelt, Eur. J. Biochem. **77**, 325 (1977).

115.S. L. Hegerson and W. Stoechenius, Arch. Biochem. Biophys. **241**, 616 (1985).

116.Y. Mukohata, M. Isoyama and A. Fuke, J. Biochem. **99**, 1 (1986).

117.N. A. Dencher and M. P. Heyn, FEBS Lett. **108**, 307 (1979).

118.S. Grzesiek and N. A. Dencher, Proc. Natl. Acad. Sci. USA. **85**, 9509 (1988).

119.Z. Dancshazy, G. I. Groma, D. Oesterhelt and T. Tittor, FEBS. Lett. **196**, 198 (1986).

120.J. F. Nagle and H. J. Morowitz, Proc. Natl. Acad. Sci. USA. **75**, 298 (1078).

121.F. Seibert, W. Mantele and W. Kreutz, FEBS. Lett. **141**, 82 (1982).

122.M. Engelhard, K. Gerwert, B. Hess, W. Kreutz and F. Siebert, Biochemistry. **24**, 400 (1985).

123.L. Eisenstien, S. L. Lin, G. Dollinger, K. Odashima, J. Termini, K. Konno, W. D. Ding and K. Nakanishi, J. Am. Chem. Soc. **109**, 6860 (1987)

124.K. Gerwert, B. Hess, J. Soppa and D. Oesterhelt, Proc. Nat. Acad. Sci. USA. **86**, 4943 (1989).

125.M. S. Braiman, T. Mogi, T. Marti, L. J. Stern, H. G. Khorana and K. J. Rothschild, Biochemistry. **27**, 8516 (1988).

126.T. Mogi, L. J. Stern, T. Marti, B. H. Chao and H. G. Khorana, Proc. Natl. Acad. Sci. USA. **85**, 4148 (1988).

127.R. Henderson, J. M. Baldwin, T. A. Ceska, F. Zemlin, E. Beckmann and K. H. Downing, J. Mol. Biol. **213**, 899 (1990).

128.R. Henderson and P. N. T. Unwin. Nature. **257**, 28 (1975).

129.J. K. Lanyi, Biochim. Biophys. Acta. **1183**, 241 (1993).

130.H. Otto, T. Marti, M. Holz, T. Mogi, M. Lindau. H. G. Khorana and M. P. Heyn, Proc. Natl. Acad. Sci. USA. **86**, 9228 (1995).

131.H. Luecke, H. T. Richter and J. K. Lanyi, Science. **280**, 1934 (1998).

132.L. S. Brown, J. Sasaki, H. Kandori, A. Maeda, R. Needleman and J. K. Lanyi, J. Biol. Chem. **270**, 27122 (1995).

133.A. K. Dioumaev, H. T. Ritcher, L. S. Brown, M. Tanio, S. Tuzi, H. Saito, Y. Kimura, R. Needleman and J. K. Lanyi, Biochemistry. **37**, 2496 (1998).

134.S. Subrahmanian and R. Henderson, Nature. **406**, 653 (2000).

135.R. Lozier, R. A. Bogomolni and W. Stoeckenius, Biophys. J. **15**, 955 (1975).

136.R. H. Birge, Biochim. Biophys. **1016**, 293 (1990).

137.A. Der, and L. Keszthelyi, *Bioelectronic Applications of Photochromic Pigments, NATO Science Series: Life Sciences* (IOS, Amsterdam, 2001).

138.R. R. Birge, Annu. Rev. Phys. Chem. **41**, 683 (1990).

139. N. N Vsevolodov, *Biomolecular Electronics An introduction via Photosensitive Proteins* (Birkhauser, Boston, 1998).

140.R. R. Birge, N. B. Gillespie, E. W. Izaguiree, A. Kusnetzow, A. F. Lawrence, D. Singh, Q. W. Song, E. Schmidt, J. A. Stuart, S. Seetharaman and J. K. Wise, J. Phys. Chem. B **103**, 10746 (1999).

141.G. Varo and J. K. Lanyi, Biochemistry. **30**, 5016 (1991).

142.S. Druckmann, N. Friedmann, J. K. Lanyi, R. Needlemann, M. Ottoelnghi and M. Sheves, Photochem. Photobiol. **56**, 1041 (1992).

143.S. Druckmann, M. P. Heyn, J. K. Lanyi, M. Ottolenghi and L. Zimanyi, Biophys. J. **65**, 1231 (1993).

144.B. Hessling, J. Herbst, R. Rammaelsberg and K. Gerwert, Biophys. J. **73**, 2071 (1997).

145.K. Ludmann, C. Gergely and Gy. Varo, Biophys. J. 75, 3110 (1998).

146.Z. P. Chen and R. R. Birge, TIBTECH. **11**, 292 (1993).

147.L. A. Drachev, A. A. Jasaitis, A. D. Kaulen, A. A. Kondrashin, E. A. Liberman, I. B. Nmecek, S. A. Ostroumov, A. Yu. Semenov and V. P. Skulachev, Nature. **249**, 321 (1974).

148.L. A. Drachev, A. D. Kaulen, S. A. Ostroumov and V. P. Skulachev, FEBS. Lett. **39**, 43 (1974).

149.A. R. McIntosh and F. Boucher, Biochim. Biophys. Acta. **1056**, 149 (1991).

150.H. W. Trissl, Photochem. Photobio. **51**, 793 (1990)

151.H.-W. Trissl and W. Gartner, Biophys. J. **26**, 751 (1987).

152.L. Keszthelyi and P. Ormos, Biophys. Chem.**18**, 397 (1983).

153.S. Y. Liu, Biophys. J. **57**, 943 (1990).

154.S. Y. Liu and T. G. Ebrey, Biophys. J. **54**, 321 (1988).

155.K. Koyama, N. Yamaguchi and T. Miyasaka, Science. **265**, 762 (1994).

156.K. Koyama, N. Yamaguchi and T. Miyasaka, Adv. Mater. **7**, 590 (1995).

157.T. Miyasaka, K. Koyama and I. Otoh, Science. **255**, 342 (1992).

158.T. Miyasaka and K.Koyama, Thin Solid Films. **210/211**, 146 (1992).

159.T. Furuno, K.Takimoto, T.Kouyama, A. Ikegami and H. Sasabe, Thin Solid Films. **160**, 145 (1988).

160.M. Ikonen, J. Peltonen, E. Vuorimaa and H. Lemmetyinen, Thin Solid Films. **213**, 277 (1992).

161.H. H. Weetall and L. A. Samuelson, Thin Solid Films. **312**, 306 (1998).

162.L. Keszthelyi, Biochim. Biophys. Acta. **598**, 429 (1980).

163.R. A. Brizzolara, Biosystems. **35**, 137 (1995).

164.R. A. Brizzolara and B. C. Beard,J. Vac. Sci. Technol. A. **12**, 2981 (1994).

165.J.-A. He, L. Samuelson, L. Li, J. Kumar and S. K. Tripathy, Langmuir.**14**, 1674 (1998).

166. J.-A. He, L. Samuelson, L. Li, J. Kumar and S. K. Tripathy, J. Phys. Chem. B. **102**, 7067 (1998).

167.S. G. Wu, L. M. Ellerby, J. S. Cohan, B. Dunn, M. A. El-Sayed, J. S. Valentine and J. I. Zink, Chem. Mater. 1993, **5**, 115 (1993).

168. H. H. Weetall, Appl.Biochem. Biotechnol. **49**, 241 (1994).

169.Z. Chen, A. Lewis, H. Takei and I. Nebenzahl, Appl. Opt. **30**, 5188 (1991).

170. Z. Chen, K. Chittibabu, K. Marx, J. Kumar, S. K. Tripathy, L.A. Samuelson, J. Akkara and D. L. Kaplan, SPIE Proc. **2189**, 105 (1994).

171.B. Robertson and E. P. Lukashev, Biophys. J. **68**, 1507 (1995).

172.J. P. Wang, S. K. Yoo, L. Song, M. A. El-Sayed, J. Phys. Chem. B **101**, 3420 (1997).

173.J. P. Wang, L. Song, S. K. Yoo, M. A. El-Sayed, J. Phys. Chem. B **101**, 10599 (1997).

174.J. A. He, L. Samuelson, L. Li, J. Kumar and S. K. Tripathy, Adv. Mater. **11**, 435 (1999).

175.F. T. Hong, Prog. Surf. Sci. **62**, 1 (1999).

176.M. Li, B. Li, L. Jiang, T. Tussila, N. Tkachenko, and H. Lemmetyinen, Langmuir **16**, 5503 (2000).

177.C. Gergely, L. Zimanyi and G. Varo, J. Phys. Chem. B. **101**, 9390 (1997).

178.Y. Saga, T. Watanabe, K. Koyama and T. Miyasaka, Anal. Sci. **15**, 365 (1999).

179.T. Mogi, L. J. Stern, T. Marti, B. H. Chao and H. G. Khorana, Proc. Natl. Sci. Acad. USA. **85**, 4148 (1988).

180.R. D. McCullough, Adv. Mater. **10**, 93 (1998).

181.T. A. Chen, X. Xu and R. D. Rieke, J. Am. Chem. Soc. **117**, 233 (1995)

182.R. A. Wessling and R. G. Zimmerman, U.S. Patent **3401**, 152 (1968).

183.P. L. Burn, D. D. C. Bradley, R. H. Friend, D. A. Halliday, A. B. Holmes, R. W. Jackson and A. Kraft, J. Chem. Soc. Perkin. Trans **1**, 3225 (1992).

184.G. Padmanabhan, and S. Ramakrishnan, J. Am. Chem. Soc. **122**, 2244 (2000).

185.F. E. Arnold and R. L. vanDeussen, Macromolecules, **2**, 479 (1969).

186.F. E. Arnold and R. L. vanDeussen, J. Appl. Polym. Sci. **15**, 2035 (1971).

187.S. A. Jenekhe, P. O. Johnson and A. K. Agarwal, Macromolecules, **23**, 4419 (1990).

188.X. Zhang and S. A. Jenekhe, Macromolecules, **33**, 2069 (2000).

189.N. Herron, Y. Wang, and H. Eckert, J. Am. Chem. Soc. **112**, 1322 (1990).

190.T. Vossmeyer, L. Katsikas, M. Giersig, I. G. Popovic, K. Diesner, A. Chemseddine, A. Eichumuer and M. Weber, J. Phys. Chem. **98**, 7665 (1994).

191.C. J. Brinkerv and G. W. Scherrer in Sol-gel Science, The physics and chemistry of sol-gel processing. Academic, Sandiego, (1989).

192.J. G. Nandha, PhD Thesis, SSCU, IISc (2000).

193.F. Jonas and L. Schrader, Synth. Met. **41-43**, 831 (1991).

194.L. M. Peter, Chem. Rev. **90**, 753 (1990).

195.A. A. Alagiriswamy and K. S. Narayan, J. Appl. Phys. **91**, 3021 (2002).

196.M. A. Lampert and P. Mark, Charge Injection in Solids (Academic, New York, 1970).

197.S. R. Forrest, M. L. Kaplan and P. H. Schimidt, J. Apll. Phys. **55**, 1492 (1981).

198.S. Bertleb, W. Brutting, and G. Paasch, Synth. Met. **122**, 37 (2001).

199.C. J. Brabec, A. Cravino, D. Meissner, N. S. Sariciftci, T. Fromhertz, M. T. Rispens, L. Sanchez, and J. C. Hummelen, Adv. Funct. Mater. **11**, 374 (2001).

200.T. J. Savenije, E. Moons, G. K. Boschloo, A. Goossens, and T. J. Schaafsma, Phys. Rev. B. **55**, 9685 (1997).

201.P.M. Borsenberger, L.T. Pautmeier, and H. Bassler, Phys. Rev. B **48**, 3066 (1993).

202.K. S. Narayan, A. A. Alagiriswamy, and R. J. Spry, Phys. Rev. B. **59**, 10054 (1999).

203.C. H. M. Maree, S. J. Roosendaal, T. J. Savenije, R. R. I. Schropp, T. J. Schaafsma, and F. H. P. M. Habraken, J. Appl. Phys. **80**, 3381 (1996).

204.S. Roy, C. P. Singh and K. P. J. Reddy, J. Appl. Phys. **90**, 3679 (2001).

205.E. P. Lukashev, E. Vozary, A. A. Kononenko, and A. B. Rubin, Biochim. Biophys. Acta. **592**, 258 (1980).

206.A. A. Kononenko, E. P. Lukashev, A. V. Maximychev, S. K. Camorovsky, A. B. Rubin, S. F. Timashev, and L. N. Chekulaeva. Biochim. Biophy. Acta. **850**, 162 (1986).

207.P. Kolodner, E. P. Lukashev, Y. Ching, and D. L. Rousseau, Proc. Natl. Acad. Sci. USA, **93**, 11618 (1996).

208.K. Koyama, T. Miyasaka, R. Needelman, and J. K. Lanyi, Chem. Lett. **8**, 769 (1999).

209.N. Tessler, N. T. Harrison, and R. H. Friend, Adv. Mater. **10**, 64 (1998).

210.V. L. Colvin, M. C. Schlamp, and A. P. Alivisatos, Nature (London) **370**, 354 (1994)

211.J. Nanda, K. S. Narayan, B. A. Kuruvilla, G. L. Murthy, and D. D. Sarma, Appl. Phys. Lett. **72**, 1335 (1998).

212.N. D. Kumar, M. P. Joshi, C. S. Friend, and P. N. Prasad, Appl. Phys. Lett. **71**, 1388 (1997).

213.Y. Wang and N. Herron, Chem. Phys. Lett. **200**, 71 (1992).

214.B. O. Dabbousi, M. G. Bawendi, O. Onitsuka, and M. F. Rubner, Appl. Phys. Lett. **66**, 1316 (1995).

215.N. C. Greenham, X. Peng, and A. P. Alivisatos, Phys. Rev. B **54**, 17628 (1996).

216.G. Yu, C. Zhang, and A. J. Heeger, Appl. Phys. Lett. **64**, 1540 (1994).

217.A. P. Alvistos, Science **271**, 933 (1996).

218. A. P. Alvistos, J. Phys. Chem. **100**, 13226 (1996).

219.H. Weller, Angew. Chem. Int. Ed. Engl. **32**, 41 (1993).

220.A. D. Yoffe, Advs. Phys. **42**, 173 (1993).

221.V. L. Colvin, M. C. Schlamp and A. P. Alivisatos, Nature. **370**, 354 (1995)

222.B. O. Dabbousi, M. G. Bawendi, O. Onitsuka and M. F. Robner, Appl. Phys. Lett. **66**, 1316 (1995).

223.S. A. Majetich and A. C. Carter, J. Phys. Chem. **97**, 8727 (1993).

224.Ai. L. Efros and A. L. Efros, Sov. Phys. Semicond. **16**, 772 (1982).

225.S. Okamoto, Y. Kanemitsu, H. Hosokawa, K. Murakoshi and S. Yanagida, Solid State Commun. **105**, 7 (1998).

226.M. C. Schlamp, X. Peng and P. Alivisatos, J. Appl. Phys. **82**, 5837 (1997).

227.G. Du, B. Taylor, R. J. Spry, M. Alexander, C. Grayson, R. Dollinger, Ferguson, B. Rienhardt and J. Burkett, Synth. Met. **97**, 135 (1998).

Publications

Relevant to thesis

1. Opt-electrical processes in a conducting polymer-bacteriorhodopsin system, **A. G. Manoj** and K. S. Narayan. (To appear in Bioelectronics and biosensors. 2003)
2. Voltage controlled spectral tuning of photoelectric signals in a conducting polymer bacteriorhodopsin device. **A. G. Manoj** and K. S. Narayan. (Appl. Phys. Lett. 83, 3614, (2003))
3. Photogenerated Charge Carrier Transport in p -Polymer n -Polymer Bilayer Structures. **A. G. Manoj**, A. A. Alagiriswamy and K. S. Narayan (J. Appl. Phys. 94, 4088, (2003))
4. Photovoltaic Properties of Polymer p-n Junctions made with P3OT/BBL Bilayers. **A. G. Manoj**, K. S. Narayan (Optical Materials, 21, 417 (2003))
5. Dual Function Hybrid Polymer-Nanoparticle Devices. K. S. Narayan, **A. G. Manoj**, J. Nanda and D. D. Sarma (App. Phys. Lett. 74, 871 (1999))
6. Optical and electronic properties of conjugated polymer - nanocluster semiconductor hybrid systems - K. S. Narayan, **A. G. Manoj**, J. Nanda, B. Kuruvilla and D. D. Sarma (Proc. of Materials Res. Socy. 519, 265 (1998))

Other publications

7. Novel Strategies for Polymer Based Light Sensors, K. S. Narayan, **A. G. Manoj**, Th. B. Singh, A. A. Alagiriswamy . (Thin Solid Films,417, 75 (2002)).
8. Photophysics of PPV derivative with varying conjugation lengths - **A. G. Manoj**, K. S. Narayan, R. Gauri, S. Ramakrishnan (Synthetic Metals,101,255 (1999))
9. Solution processing of active semiconducting polymers and conducting polymer anodes for fabricating photodetectors. V. K. Basavaraj, **A. G. Manoj** and K. S. Narayan.(Submitted to IEE Proceedings 2003)
10. Strategies for efficient photo-induced charge separation and transport in Semiconducting Polymer Systems. K. S. Narayan, Th. B. Singh, **A. G. Manoj**, V. K. Basavaraj and S. Dutta (Photonics 2002)

JNCASR
Acc No. 3271
LIBRARY